NASA CR-132532

(NASA-CR-132532) PRECISION LASER RANGE FINDER SYSTEM DESIGN FOR ADVANCED TECHNOLOGY LABORATORY APPLICATIONS Final Report (Aerospace Corp., Los Angeles, Calif.) 119 p HC $9.00 CSCL 20E G3/16 N74-34911 Unclas 52142

PRICES SUBJECT TO CHANGE

ATR-74(7438)-1

PRECISION LASER RANGEFINDER SYSTEM DESIGN FOR ADVANCED TECHNOLOGY LABORATORY APPLICATIONS

Final Report

Submitted to

Langley Research Center
National Aeronautics and Space Administration

Contract No. NAS1-12727

Principal Investigators: K. E. Golden
R. L. Kohn
D. H. Seib

Electronics Research Laboratory
The Aerospace Corporation
P. O. Box 92957
Los Angeles, California 90009

23 July 1974

Reproduced by
NATIONAL TECHNICAL INFORMATION SERVICE
US Department of Commerce
Springfield, VA 22151

PRECISION LASER RANGEFINDER SYSTEM DESIGN FOR ADVANCED TECHNOLOGY LABORATORY APPLICATIONS

by

K. E. Golden

R. L. Kohn

D. H. Seib

ABSTRACT

Preliminary system design of a pulsed precision ruby laser rangefinder system is presented. The system has potential range resolution of 0.4 cm when atmospheric effects are negligible. The system being proposed for flight testing on the Advanced Technology Laboratory (ATL) consists of a modelocked ruby laser transmitter, course and vernier rangefinder receivers, optical beacon retroreflector tracking system and a network of ATL tracking retroreflectors. Performance calculations indicate that spacecraft to ground ranging accuracies of 1 to 2 cm can be expected.

CONTENTS

ABSTRACT

I. INTRODUCTION 1

II. PROTOTYPE SYSTEM 7

III. GENERAL SYSTEM COMPONENTS 12

IV. COARSE RANGE DETECTOR 15

V. VERNIER RANGE DETECTOR 22

VI. LASER TRANSMITTER 44

VII. LASER BEACON TRACKING SYSTEM 56

VIII. RETROREFLECTOR ARRAY SYSTEM 60

IX. SYSTEM PERFORMANCE 67

X. REPRESENTATIVE SYSTEM 78

XI. FLIGHT TEST EXPERIMENTS 81

XII. CONCLUSIONS 87

FIGURES 89

REFERENCES 113

I. INTRODUCTION

A. OBJECTIVES

The objectives of this study are to evaluate the feasibility of performing precision laser ranging and altimeter experiments on the Advanced Technology Laboratory (ATL), to provide a viable conceptual experiment design, and to determine the expected system performance. The flight test objectives are: to determine the utility, limitations and accuracy of a precision laser ranging system for measuring absolute and differential range, line of sight angles, and range rate; to demonstrate ranging accuracies equal to or better than $\pm$ 3 cm over ranges up to or greater than 10^8 cm (expected maximum slant range from ATL to earth based retroreflector at a zenith angle of 60°); to evaluate the utility of onboard laser-ranging as opposed to ground based systems with passive retroreflector satellites; and to demonstrate the potential utility of onboard laser ranging for various geodetic measurements, geodynamic observations, oceanographic observations, and improved determination of satellite ephemeris data.

B. GENERAL

Recent state-of-the-art advances in pulse laser ranging systems have the potential performance needed for the ATL experimental objectives. Current operational pulsed laser ranging systems typically employ giant pulse ruby laser transmitters generating 15 to 20 nsec pulses, broadband photomultiplier detectors and conventional electronic time-interval meter circuitry having timing resolution and accuracy of about 1 nsec. The resulting range resolution is about $\pm$ 15 cm. It is expected that in the near future these systems

will be upgraded by using modelocked laser transmitters and improved time interval meter circuitry. Time interval meters with 0.25 nsec accuracy will probably be degraded in practice by pulse shape and amplitude variations in the return pulse. An overall timing accuracy of about 0.5 nsec is more realistic which would result in about ± 8 cm range resolution including worst case atmospheric effects.

Further improvements in range resolution can be obtained by incorporating a vernier ranging system consisting of an image converter receiver with synchronous image deflection (Ref. 1). The vernier receiver was developed under an AAFE program and a prototype laser ranging system was built. This system had a timing accuracy of 40 psec and a total ranging uncertainty of about ± 1.2 cm at 18 km. Image converter streak cameras have been reported (Ref. 2) with 1 - 2 psec time resolution. It is expected that a vernier range receiver could be built with at least 5 psec timing accuracy assuming state-of-the-art spatial resolution and sweep speeds. Vernier timing accuracies of 5 psec would make two color laser ranging practical for ground to satellite applications.

The range resolution of the vernier receiving system represents a substantial improvement in laser ranging needed to advance global geodetic, earth and ocean physics technology. In these applications, the precision laser rangefinder is a tool used to obtain high accuracy (± 3 cm or better) quasi-simultaneous range measurements between a satellite and four or more ground sites. A satellite system is desirable because of global coverage and inter-continental base point potential. The specific application may involve the altitude measurements, surface distance reconstruction, surface strain rate monitoring and

improving satellite ephemeris data. For example, monitoring inter-retroreflector distances with an accuracy of 1 - 10 cm is needed in the detection and measurement of large scale tectonic motion (e.g., continental drift). The determination of the inter-continental distances are accomplished by simultaneously measuring the distance between a satellite and four ground stations. Six sets of measurements are required to solve for the six unknown surface distances. The resulting uncertainties in inter-retroreflector distances are, in general, appreciably greater than those of the individual slant range measurements and depend on the retroreflector base point geometry, master clock accuracy and stability, satellite orbit, number of slant range measurements to each retroreflector and the uncertainties in the atmospheric effects on the velocity of light. A detailed error analysis is beyond the scope of this report. A preliminary error analysis indicates that the errors in determining these six distances are on the average about 6 times larger than the errors in the individual laser-ranging measurements. Since the error in an individual range measurement is ~ 1 cm, the errors in the inter-continental distances will be about ~ 6 cm. During each pass of the satellite, however, there will be many more than six sets of range measurements, so that many independent determinations of each inter-reflector distance will be made. A statistical average of these independent values will have an over-all uncertainty of less than the above.

The difficulties associated with decreasing laser ranging uncertainty below 5 cm are formidable in satellite to ground applications. The measured range has to be corrected for the effect of the refractive index of the atmosphere, a correction of about 2.4 m in a ground-to-satellite measurement.

The atmospheric correction can be calculated if the surface atmospheric pressure, site altitude, and line of sight angle are known. Uncertainties in the atmospheric range correction are theoretically less than 1 cm at the zenith and as great as 10 cm for large zenith angles. The laser return pulse is very weak, in practice, and its shape can be severely distorted as a result of the retro-reflector orientation. Statistical fluctuations and pulse stretching are encountered with a retroreflector array consisting of a number of corner cubes distributed over a finite area when the array is oriented at an angle to the beam path. As a result, the task of establishing the time of arrival of the centroid of the pulse (or its leading edge, or, indeed, any fiducial mark) is very difficult and uncertain with the conventional time interval meter approach. The vernier system, on the other hand, contains information about the orientation of the retroreflector in the shape of the return pulse. In order to take full advantage of the potential differential range resolution, the laser transmitter should be modelocked with a pulse width of about 10 to 25 psec. The retroreflector design should not unduly lengthen or degrade the rise time of the return pulse since pulse stretching decreases the total number of electrons collected in a given detector element. If a planar retroreflector array is used, active pointing and/or pulse shape analysis may be required to maintain desired measurement precision. If a spherical retroreflector design is used, active pointing is not needed; however, the return pulse is lengthened and could become longer than one sweep period of the vernier. Leading edge detection is then required rather than pulse centroid detection.

Precise time-of-flight measurements do not lead to correspondingly precise range determinations, because of the uncertainty in the atmospheric

correction. Picosecond timing measurements would, however, make it possible to improve the determination of this correction by means of the so-called two-color ranging technique (Ref. 3). In this technique, the laser transmitter would provide simultaneous ranging pulses at two different wavelengths (e.g., by means of an optical frequency-doubling crystal). Measurement of the difference between the times of flight of the two pulses (as a result of atmospheric dispersion) would permit a determination of the atmospheric correction independently of any knowledge of atmospheric pressure or temperature. For example, the uncertainty in determining the atmospheric correction is about 8.4 times greater than the individual time-of-flight measurements at ruby and doubled ruby wavelengths. With 5 psec vernier timing accuracy, the resulting range accuracy would be $\pm$ 6 mm independent of the atmospheric temperature and pressure variations.

C. BASIC SYSTEM

To satisfy the flight test objectives, the basic system concept is illustrated in Fig. 1. The ranging system consists of a modelocked laser transmitter, a polarization modulator to encode the outgoing pulse train, auto tracking transmitting and receiving optics, optical AGC attenuator, polarization sensitive course range detectors, course range time interval meter, a vernier range detector consisting of an image converter receiver with synchronous image deflection, and an extensive network of retroreflector arrays. To reduce background levels in the vernier system, an electrically operated optical attenuator is placed in the receiving optics and is automatically adjusted to the level of the last measurement. In order to maintain necessary angular accuracy and minimize required laser energy, a laser beacon tracking system is

incorporated into the basic ranging system. On the earth based retroreflector systems, meteorological observations and incident angle measurements are required for atmospheric corrections. A background radiometer is included since background radiation levels are needed to properly evaluate system performance in daylight. A detailed description of the ranging system appears in later sections.

II. PROTOTYPE SYSTEM

A. GENERAL

The precision laser ranging system design presented in this study is patterned after a prototype system shown in Fig. 2. Several refinements to the prototype system have been incorporated in the system shown in Fig. 1 which should give better reliability, improved maximum range performance, and easier optical alignment. A detailed discussion of the improved laser system, modifications and expected performances appears in Secs. III - IX.

The basic prototype ranging system appearing in Fig. 2 consists of a modelocked laser transmitter, a pulse selector which selects one sub-pulse from the modelock train, a retroreflector array to reflect the laser pulse back to the receiver, a course range receiver and a vernier range receiver. The elapsed time between the received and transmitted pulses is related to the distance between the laser transceiver and retroreflector and can be expressed in terms of an integral number of vernier sweep periods and an additional fractional period. The integral number of sweep periods is obtained directly from the course range receiver consisting of a time interval meter and a broadband photomultiplier. The course range timing accuracy needed to eliminate the range ambiguities associated with the vernier ranging unit is $\pm 0.25\ \tau_V$ where τ_V is the sweep period of the vernier image tube. The fractional period is measured with the vernier range receiver consisting of an image converter tube, a stable VHF sinusoidal deflection plate driver, an image intensifier and image recording device. In the prototype system, the linear separations between the transmit, delayed transmit, the return, and

delayed return images on the output of the image converter tube are used to derive the fractional period between the transmit and return pulses. When linear sinusoidal image deflection is used, the output image position of a single pulse yields an ambiguous time of arrival since a solution exists in two adjacent quadrants of the deflection sine wave. This ambiguity can be simply removed by focusing both the original pulse and a delayed pulse of about $0.25\ \tau_V$ on the image converter photocathode, or by using a circular deflection sweep on the image converter tube. A more detailed discussion appears in Ref. 1. The approximate system parameters of the prototype system are listed in Table 1.

Table 1. Prototype System Specifications

Max. pulse energy $\approx$ 1 mjoules
Pulse width = 500 psec
Transit beam divergence $\approx$ 1 mrad
Wavelength = 0.6943 μm
System loss = - 12 db
Receiver area = 324 cm^2
Retroreflector area = 324 cm^2
Return beam divergence $\approx$ 0.3 mrad
Max. range = 1.8×10^6 cm
One way atmospheric attenuation at 18 km $\geq$ 2 dB
Return signal at photocathode $\leq 1.9 \times 10^3$ photoelectrons/psec
S/N > 20 dB
Dynamic resolution = 3 - 5 line pairs per mm
Average writing speed = 1.8×10^{10} mm/sec
Image converter timing resolution = 19 psec

B. RANGING MEASUREMENTS

The accuracy and range resolution of the prototype system were first measured on a short rooftop range where atmospheric effects could be neglected. The one-way transmission distance was about 4000 cm. The results of these laser measurements were compared with a steel tape measurement of the transmission distance. The results illustrate that the RMS timing accuracy was about 40 psec. With the image converter writing speed, transit time spreading, and dynamic resolution of the RCA C73435U image converter tube, timing resolution of 19 psec is theoretically possible; however, the laser pulse widths are too wide to experimentally validate the potential timing resolution of the image converter system.

The prototype system was then moved to the Cerro Gordo remote ranging site located near Lone Pine, California (Ref. 4). Retroreflector sites were located about 7, 12, and 18 km from the transmitter site. Ranging measurements were performed during the months of September and October. During this period over 700 individual range measurements were performed, and end point meteorological data gathered. For the average atmospheric conditions, the atmospheric range corrections are 152, 261, and 397 cm for the 7, 12, and 18 km ranges. The range uncertainty in the Cerro Gordo data associated with the atmospheric corrections provide an upper limit on the expected accuracy of ATL to ground measurements. The atmospheric corrections through the entire atmosphere are of the same magnitude as the Cerro Gordo results (e.g., at the zenith, the atmospheric correction is about 240 cm for standard conditions); however, the statistical variations in the temperature along near horizontal paths produce larger uncertainties in the

range corrections that laser paths through the atmosphere near the zenith. A sample of the actual data obtained at the 18 km range is shown in Fig. 3, and a summary of all the data is presented in Table 2.

The daily average atmospheric corrected range data are presented in Fig. 4. The range data were corrected for atmospheric propagation effects using the summer midaltitude atmospheric model appearing in Ref. 5 and actual meteorological data taken during the range measurements. These results clearly show the range accuracy improvement when actual meteorological data is used in the determination of range corrections.

The statistical variations in the range measurements are caused by timing and propagation correction uncertainties. The uncertainty in timing was experimentally determined from the short range data. The propagation uncertainties are caused by variations in air density and water vapor content along the propagation path. Range errors associated with atmospheric turbulence and refraction are small compared to the uncertainties in the group velocity of light. For simplicity, the range uncertainty is assumed to be a function of the variation in air density along the propagation path. If we ascribe air density variations to temperature, the resulting average temperature uncertainty is about $\pm 0.9^{\circ}$ K.

The above is not meant to be a definitive meteorological data analysis but to bound possible temperature variation along the near horizontal propagation paths at Cerro Gordo.

Table 2. Range Results Obtained with Prototype System

One Way Reference Measurement (cm)	R.M.S. Coarse Timing Accuracy	Retro-reflector Altitude (km)	No. of Measurements (Laser)	One Way Laser Measurement (cm)
4049.2 ± 0.5	± 1.3 nsec		31	4049.5 ± 0.7
4095.2 ± 0.5	± 1.6 nsec		50	4095.3 ± 0.6
78.6 ± 0.5	± 1.5 nsec		21	79.1 ± 0.6
693152.9 ± 3.6	± 1.1 nsec	1.899	155	693146.7 ± 0.8
693521.0 ± 3.6	± 1.0 nsec	1.899	185	693517.8 ± 0.9
1188467.4 ± 6.4	± 1.4 nsec	1.752	147	1188459.9 ± 0.8
1809143.4 ± 7.8	* ± 2.3 nsec	1.794	215	1809137.3 ± 1.2

* Average time interval reading 3 nsec low due to malfunctioning of half-max unit

The upper limit on the range uncertainty in a satellite application will now be estimated assuming the temperature variation inferred from the Cerro Gordo range results. The atmospheric correction at 0.6943 μm from sea level to orbital altitudes is

$$\Delta R = 67.8 \frac{P_0(\text{mb})}{T_0(^\circ\text{K})} \sec \theta_Z - 0.243 (\sec^3\theta_Z - \sec \theta_Z), \text{ cm}$$

where P_0 is the surface atmospheric pressure, T_0 is the surface air temperature, and θ_Z is the line of sight zenith angle. Assuming a temperature variation of $\pm 0.9^\circ$K and an uncertainty in the line of sight angle of ± 2 mrad, the expected range uncertainty is ± 0.8 cm at $\theta_Z = 0^\circ$ and ± 2.2 cm at $\theta_Z = 60^\circ$.

III. GENERAL SYSTEM COMPONENTS

In this section, the conceptual design of the improved precision laser rangefinder system shown in Fig. 1 will be discussed. The system works as follows: after the optical laser beacon tracking system has locked on to the desired retroreflector array, the modelocked laser transmitter is triggered. As opposed to the prototype system, the entire modelocked pulse train is used to measure range which results in a factor of 7 improvement in the number of return photons. Using the entire pulse train also reduces space charge effects in the image converter receiver. The only complication is that the laser cavity has to be tuned to the sweep frequency of the vernier detector.

The pulse train passes through the polarization modulator where one of the central pulses is coded by rotating its plane of polarization by 90 degrees. The modulated pulse train is then amplified to about 0.3 joules, the beam is expanded to about 2.0 cm in diameter and the transmit beam divergence adjusted for the mission requirements. A small portion of the transmit beam is directed toward the course range and vernier receivers and serves as the transmit time reference.

The function of the laser rangefinder receiver system is to accept and detect the outgoing and return laser pulses and provide electrical outputs which can be used to extract accurate timing information. This is accomplished in two stages with two different detectors; a course range detector which allows determination of the number of cycles of a reference oscillator elapsed between the outgoing and return pulses and a vernier detector which determines the position of the pulse within a single cycle.

As discussed previously, the optical signal to be detected consists of a string of narrow pulses (~25 psec, ignoring for the moment the various effects which tend to spread the electron beam) spaced 6.67 nsec apart. The pulse train in assumed to have Gaussian amplitude distribution with 13 sub-pulses within the 10% full width. The polarization of the central pulse will be rotated by 90° with respect to the polarization of the remaining pulses to provide "keying" of the train (see Fig. 5). The course detection system must detect this pulse polarization pattern to provide the desired timing data. This can be accomplished by a polarization separator element and two fast photomultipliers, one for each direction of polarization. The occurrance of a detected pulse in one channel in conjunction with a count τ_V seconds (τ_V = 6.67 nsec) later in the second channel constitutes detection of this event.

The proposed vernier detector consists of a photocathode, an electron deflection and acceleration section, and a charge storage target. The deflection system is such as to cause photoelectrons to follow a circular path on the target; the time required to complete a circle is identical to the interpulse spacing. Therefore, photons received in all the pulses of the train may be utilized by the vernier, giving a substantial signal gain compared to utilizing one pulse only. Readout of the target, using one of several possible methods, gives the angular position of the stored signal, which can then be correlated with the phase of the driving voltage to give the fine range determination. The same detector is used to determine both the time of the outgoing pulse and the time of the return pulse; operation is precisely the same in either case.

Since the vernier detector is necessarily of the charge storage type and will therefore integrate background events, the false alarm probability per readout can be reduced by proper gating. For example, the vernier detector could be normally gated off by means of a control grid or gating deflection electrodes. The tube is then gated on by means of the course range detectors. An optical delay line of about 100 nsec is needed so that the course range detectors and associated logic circuitry have enough time to trigger the vernier detector grid prior to the arrival of the optical pulse train at the photocathode. Subsequent background and false alarm probability calculations suggest that the simpler concept of a programmed return gate could be implemented by setting the center of the return gate at the expected arrival time. A gate width of 1 msec would not degrade system performance. The expected time of arrival could be derived from the previous course range measurement to better than $\pm 500\mu sec$.

IV. COARSE RANGE DETECTOR

A. GENERAL

As discussed briefly in Section III, the coarse ranging detector must detect a pulse of one polarization followed by a pulse of orthogonal polarization τ_V seconds later. This can be accomplished as follows. The input pulse train is passed through a Glan-Thompson Prism, which spatially separates the two polarizations into two channels, A and B (see Fig. 6). Each channel contains a fast photomultiplier operating in the threshold detection mode. That is, a threshold circuit and pulse shaper is adjusted to trigger and supply a narrow, standardized pulse whenever an anode pulse equivalent to the liberation of N_T or more photocathode electrons during $\sim$ 100 psec is present. Since these photomultipliers must be left on the entire time, it is obviously necessary to have $N_T > 1$ to suppress background photoelectrons and thermionic electrons. If channel B contains the single pulse of rotated polarization, and channel A the remaining twelve pulses, the desired event can be detected by delaying the output of photomultiplier A for τ_V seconds and applying this delayed signal to a coincidence gate with the undelayed output of photomultiplier B. A coincidence between these two signals signifies the desired event (Fig. 7). The use of such a coincidence scheme and two independent photomultipliers gives this system a great immunity to false alarms, as will be seen below (Part C).

B. DETECTION PROBABILITY

For the situation described above, the detection probability, P_D, can be written:

$$P_D = P_A \cdot P_B \tag{1}$$

where P_A is the probability of detecting the pulse in channel A immediately preceding the rotated pulse and P_B is the probability of detecting the rotated pulse in channel B. Both P_A and P_B are functions of the mean number of photoelectrons per pulse, or the input signal level, and the threshold number N_T. It is assumed that the pulse height distribution curve and time resolution capabilities of the photomultipliers are such that events involving 1, 2, 3, or more photoelectrons within 100 psec can be resolved. This condition can be adequately satisfied using high gain first dynode structures. Assuming 13 sub-pulses within the 10% full width, the pulse in channel A immediately preceding the pulse in channel B has an amplitude of 0.94 times the amplitude of pulse B. If the mean number of photoelectrons in pulse B is $\overline{N}_e$, then by using Poisson statistics to describe the actual number of photons received in any one trial, the probabilities P_A and P_B can be simply calculated for different N_T and $\overline{N}_e$.

The mean number of photoelectrons in the largest pulse is, of course, related to the mean number of photons at the photocathode, $\overline{N}_p$, through the photocathode quantum efficiency, η:

$$\overline{N}_e = \eta \overline{N}_p \tag{2}$$

In Fig. 8, the calculated detection probabilities are therefore plotted as a function of signal photons at the photocathode in the largest pulse (pulse B) for $\eta = 0.15$, which can be attained with a GaAs photocathode.

C. FALSE ALARM PROBABILITY

False counts in the detection system discussed above can occur in two ways:

1) a noise pulse occurs in photomultiplier A and is followed by a noise pulse in photomultiplier B τ_V seconds later, or

2) one of the five initial signal pulses in channel A occurs followed by a noise pulse in photomultiplier B after τ_V seconds.

To calculate the number of false counts expected, N_f, let $\overline{FAR}$ be the mean number of noise pulses/sec in photomultiplier A or B (assumed identical). Furthermore, let P_n be the probability that a noise pulse occurs in photomultiplier B in time t_R, which is the resolving time of the photomultiplier. Then:

$$N_f = (\overline{FAR} + 5) \cdot P_n \frac{2 \cdot t_s}{t_R} \qquad (3)$$

The factor five takes into account the second process mentioned above.

The factor $2t_s/t_R$ takes into account the fact that output pulses from the photomultiplier, with duration of $t_R \sim 100$ psec, are standardized in amplitude and in width (to $t_s \sim 1$ nsec) before application to the coincidence gate. Therefore there are approximately $2\,t_s/t_R$ independent photomultiplier resolution time intervals that can cause coincidence.

Noise pulses, or an undesired signal exceeding the threshold signal in either photomultiplier can occur due to the following processes:

1) N_T (the threshold number) or more photoelectrons are emitted during the time t_R due to background photons or thermal emission;

2) A cosmic ray (proton) or other high energy particle strikes the photomultiplier window;

3) After pulses associated with a cosmic ray event;

4) $N_T - 1$ photoelectrons are emitted during the time t_R, due to background photons or thermal emission, and because of the width of the photomultiplier pulse height distribution curve, cause an output greater than N_T.

To evaluate Eq. (3), the $\overline{FAR}$ and P_n due to all of these processes acting in concert must be evaluated. It is assumed that the photomultiplier gain can be made such that Johnson noise in the anode resistor or other electronic noise can be made negligible compared to the above sources.

Noise sources 1) and 4) above are considered first. If there are N_{BG} background photoelectrons emitter per second and N_{th} thermal electrons per second, then the mean number emitted in t_R second is

$$a = (N_{BG} + N_{th})\, t_R. \tag{4}$$

The probability that N_T or more background events occur in t_R second is:

$$P(N \geq N_T) = 1 - P(0) - P(1) - \ldots P(N_T - 1), \tag{5}$$

where P(n) is the Poisson probability function with mean a:

$$P(n) = \frac{a^n e^{-a}}{n!}. \tag{6}$$

For small a, $P(N \geq N_T) = \frac{a^2}{2}, \frac{a^3}{6}, \frac{a^4}{24}$ for $N_T = 2, 3, 4$ respectively. Therefore, for the first noise source

$$\overline{FAR}_1 = P(N \geq N_T) \cdot \frac{1}{t_R} \tag{7}$$

$$P_{n,1} = P(N \geq N_T) \tag{8}$$

In similar fashion, for the fourth noise source, if F is the fractional overlap of the pulse height peak for N_T-1 electrons above the threshold for N_T electrons, then

$$\overline{FAR}_4 = \frac{F \cdot P(N = N_T - 1)}{t_R}$$

$$P_{n,4} = F \cdot P(N = N_T - 1) \tag{9}$$

$P(N = N_T - 1) = a, \frac{a^2}{2}, \frac{a^3}{6}$ for $N_T = 2, 3, 4$ respectively.

Cosmic rays produce Cerenkov radiation in photomultiplier window materials which can be coupled to the photocathode to create a large output pulse (Ref. 6). Therefore, for the threshold levels under consideration here, each cosmic ray event produces a noise count. High energy electrons have a much smaller effect, producing a noise count for approximately every 1000 high energy electrons incident on the photomultiplier face (Ref. 7). Afterpulses are often associated with cosmic ray pulses. These pulses tend to be small and with proper choice of window material can be reduced to ~ 5 (Ref. 8). For a 556 Km orbit (~ 1.09 earth radii) the maximum high energy particle fluxes are (Ref. 9):

Electrons $(E \geq 0.5 \text{ MeV}) < 10^3/\text{cm}^2\text{-sec}$

Protons $(E \geq 4 \text{ MeV}) < 10/\text{cm}^2\text{-sec}$.

Therefore, assuming electron induced events to be negligible and including a factor of 5 after pulsing to be conservative, for a 1 cm^2 window we have

$$\overline{FAR}_{2,3} = 50/\text{sec} \tag{10}$$

and the probability of a cosmic ray induced event in t_R seconds:

$$P_{n,2} = 1 - P(0) = 1 - e^{-50t_R} \cong 50\, t_R \tag{11}$$

Therefore, combining these three sources, we have

$$\overline{FAR} = \frac{P(N \geq N_T)}{t_R} + \frac{F \cdot P(N = N_T - 1)}{t_R} + 50\ /\text{sec} \tag{12}$$

and

$$P_n = P(N \geq N_T) + P(N = N_T - 1)F + 50\, t_R \tag{13}$$

Specification of the various parameters and use of Eqs. (5) and (6) allows Eq. (12) and (13) to be evaluated as a function of background; hence Eq. (3) for the system false count rate can be evaluated.

For evaluation of Eq. (3) we use the following parameter values:

η = photocathode quantum efficiency = 0.15

N_{th} = $10^3/\text{cm}^2$ - sec; 1 cm^2 photocathode area

F = 0.1

t_R = 100 psec; t_s = 1 nsec

Results are shown in Fig. 9 as a function of background photons per second at each photocathode. Note that a portion of the curve for $N_T = 2$ has been shifted downward by 5 orders of magnitude. The curve for $N_T = 2$ and the high background portion of the curve for $N_T = 3$ are dominated by the effect of overlap of the pulse height spectra. At low backgrounds and $N_T = 3$ and 4, the cosmic ray events dominate. Fig. 9 indicates that a threshold > 2 should be chosen to keep the number of false counts down to an acceptable level. This causes some reduction in

detection probability (Fig. 8). Alternatively, improvement of the pulse height spectra overlap factor would decrease the false count rate at a given threshold.

D. IMPLEMENTATION OF THE COARSE DETECTOR

Static crossed field photomultipliers suitable for use in the coarse ranging system have been built by Varian Associates. These photomultipliers have rise and fall times of ~ 100 psec and can resolve 50 psec pulses 1 nsec apart. The manufacturer indicates there should be no problem with pulse overlap at the highest levels (~ 3000 photoelectrons) and pulse spacings (6.67 nsec) encountered in the present application. The photomultiplier incorporates a GaAs photocathode for high quantum efficiency (~ 15%) at 0.6943 μm. High gain GaP dynodes can also be incorporated to give a good pulse height spectrum. Little or no data is available on the ability of SCFPM's to detect very small numbers of photoelectrons; however SCFPM's would not be expected to differ materially from other photomultipliers in this respect.

Tube weight, including magnets, is 3-3/4 lbs. each and they occupy ~ 800 cm^3. These tubes require operating voltages of -2400 VDC and +600 VDC (4 stage tube) and draw 0.3-1 mA from the supply circuit.

V. VERNIER RANGE DETECTOR

A. GENERAL

The function of the vernier detector is to measure the arrival time of outgoing and return ranging pulses to within a fraction of a cycle of the reference oscillator so that ranging accuracies of a fraction of a centimeter can be realized. A general schematic diagram of the proposed vernier detector is given in Fig. 10. The incoming optical pulses are focused upon a photocathode. The resulting photoelectrons are accelerated by a large voltage on the extraction grid, necessary to minimize transit time dispersion due to variation in initial photoelectron velocities. The photoelectrons are then introduced into the deflection space; sinusoidal voltages in phase quadrature are applied to two perpendicular sets of electrodes. This results in the electron spot being swept around a circular path at the target at constant velocity; any angular position on this circle corresponds to a unique phase of the driving voltages, hence time. The electron bunch first impacts upon an electron gain section and the enhanced signal is stored on a charge storage target. Use of a storage target and synchronization of the deflection voltage frequency with the interpulse spacing allows the entire 13 pulses of the optical pulse train to be utilized for increased detection probability. Finally the charge pattern stored on the target is read off by some suitable means and the angular position of any detected signal is obrained, to be used in computation of the range.

The vernier detector is analyzed in further detail below. The process of extraction of the photoelectrons and processes which contribute to time dispersion of the photoelectron bunch are considered first, followed by discussion

of the required target geometry. The detector is then analyzed under the assumption that the target and readout section are perfect and add no noise to the output signal. This assumption allows determination of the limitations on the detector occurring because of photon statistics and background considerations. Finally, means of actually realizing the target structure are considered and any additional limitations due to detector noise sources are included.

B. SYSTEM TIME RESOLUTION

The maximum theoretical time resolution of the vernier receiver is limited by dynamic spatial resolution of the image at the detector target array, the transit time spread in the photoelectrons caused by the initial electron velocity distribution, space charge limitations near the photocathode, electron beam spreading in the drift tube region of the device caused by electrostatic forces, and frequency drift in the laser cavity. The time resolution of the system is also degraded by retroreflector design and laser pulse width. Finally, use of a target with a finite number of resolution elements limits the attainable time resolution to the equivalent element time (Part C). The equivalent return pulse width can be expressed as

$$\Delta t_{return} = \left[(\Delta t_S)^2 + (\Delta t_D)^2 + (\Delta t_p)^2 + (\Delta t_R)^2 + (\Delta t_a)^2 + (\Delta t_F)^2 \right]^{1/2} \tag{14}$$

Δt_S is the time resolution associated with dynamic spatial resolution, Δt_D is the transit time spread of the photoelectrons, Δt_p is the laser pulse width, Δt_R is the retroreflector transit time spreading, Δt_a is the pulse spreading caused by the atmosphere, and Δt_F is equivalent image spreading caused by frequency drift in the laser cavity.

The time resolution Δt_S is equal to

$$\Delta t_S = \frac{1}{S\ell_p} \tag{15}$$

where S is the image sweep velocity expressed in mm/sec and ℓ_p is the spatial resolution expressed in line pairs/mm. Image converter devices having picosecond electron transit time spread have spatial resolutions of about 3 to 5 line pairs/mm (Ref. 2 & 10). Better spatial resolution should be possible if the electron optics were designed to operate with the high extraction electric fields needed for picosecond operations. The actual photocathode dimensions needed for the circular scan vernier receiver is about 2 mm x 2 mm which simplifies the electron optics design. The maximum allowable spatial resolution will be limited by diffraction effects and the initial electron velocity distribution in direction and magnitude. For the purpose of this analysis, we will assume a conservative resolution of 5 line pairs/mm, vernier detector sweep frequency of 150 MHz, a 2.5 cm diameter scan, sweep velocity of 1.2×10^{10} mm/sec which results in $\Delta t_S = 16.7$ psec.

The photoelectron transit time spread can be approximately calculated as follows (Ref. 11):

$$\Delta t_D = 2.34 \times 10^{-8} \frac{\sqrt{\Delta\epsilon(\mathrm{ev})}}{E(\mathrm{volts/cm})}, \tag{16}$$

where $\Delta\epsilon$ is the total emission energy spread of photoelectrons, and E is the cathode electric field strength. The picosecond image converter camera tubes typically employ an extraction electrode located about 3 mm from the photocathode. Voltages up to 2000 volts have been applied which result in 1 - 2 psec transit time spread. For the application at hand, only about 750 V is needed for an S-20

photocathode and a laser wavelength of 0.6943 μm. For these conditions, the spread in emission energy is about 0.4 eV resulting in a transit time spread of Δt_D = 6 psec when a 2.5kV/cm extraction electric field is applied. For two-color laser ranging applications extraction electric fields of 10kV/cm are needed which results in a transit time spread of 1.5 psec.

The equivalent return pulse width is equal to Δt_{return} = 40 psec if we assume a laser pulse width of 25 psec and 8 psec image spreading associated with the laser cavity frequency not equalling the image converter sweep frequency.

Space charge effects can normally be neglected so long as a maximum current density is not exceeded. For practical image converter devices with picosecond time resolution the maximum current density can be expressed as (Ref. 10):

$$J_{max} < \frac{1.27 \times 10^{-4}\, V_E^{3/2}\,(\text{volts})}{x^2(\text{cm})}, \quad \text{ma/cm}^2 \tag{17}$$

where V_E is the voltage applied to the extraction electrode and x is the distance between the electrode and photocathode. For an image size of 0.2 mm in diameter, an extraction voltage of 750 volts and extraction electrode spacing of 3 mm, the photocathode current density should be less than 29 mA/cm^2. The resulting signal at the vernier photocathode should be less than 2.4×10^4 photons/pulse to insure that space charge effects do not degrade the time resolution of the system.

Electron beam spreading can also degrade the time resolution of the vernier system. Assuming a beam diameter increase of about 20%, the resulting photocathode current is equal to (Ref. 12):

$$\left(\frac{2z}{d_o}\right) \frac{I^{1/2}(ma)}{32.3\ V_a^{3/4}(kV)} = 0.9, \tag{18}$$

where z is the distance along the drift region, d_o is the image diameter at the entrance of the drift region, V_a is the anode voltage and I is the total current. The resulting current is equal to 5.5×10^{-3} ma, assuming a vernier detector length of 300 mm, 25 psec laser pulse, an image size of 0.2 mm, and an anode voltage of 15 kV. The signal at the photocathode should therefore be kept below 1.4×10^4 photons/pulse to insure minimal electron beam spreading.

C. TARGET GEOMETRY

As discussed in Part A, the deflected electron bunch traces a circle in the target plane. Therefore, the electron target should be in the shape of a ring of individual resolution cells. The diameter of the ring is determined by the amount of deflection attainable; the size of the individual elements is determined (in the circumferential direction) by this diameter and by the number of resolution cells desired. In the radial direction, the resolution element size is determined by the stability of the deflection voltage and the photocathode spot size. Deflection parameters to be used imply that the ring diameter will be 1.25 - 2.5 cm. Two hundred and fifty resolution elements along the circumference are desired; this implies that each element will be (for the 2.5 cm diameter) .31 mm wide. For a deflection voltage stability of $\pm$ 5% and a cathode spot size of 0.20 mm, the length of the elements is 1.5 mm. A sketch of the target structure is given in Fig. 11. A cycle time of 6.67 nsec implies that 250 elements give an elemental resolution of 27 psec. The spot velocity, for the 2.5 cm diameter ring, is 1.2×10^{10} mm/sec.

For applications in which the elapsed time between outgoing and return pulses is large (e.g., satellite to ground) one target ring would be sufficient to detect both pulses. The only requirement is that the readout of the target be sufficiently fast so that the signal due to the outgoing pulse can be read out and the target reset to receive the return before the arrival of the return signal. For shorter range missions, when the transit time is not sufficient for this condition to be met, there are at least two possibilities for discriminating between the outgoing and return pulses (Fig. 12). In the first, only a single target ring is used and the two different pulses are keyed in different ways, i.e., with different time delays. For instance, a delay of τ_a could be introduced into one pulse and a delay of $3\tau_a$ into the second; events on the target could then be distinguished due to their different separations. This approach would simplify target design but signal photons in each individual pulse would be reduced by a factor of two. An alternative might be to use two concentric rings and change the deflection voltage level between outgoing and return pulses so that each falls on a different ring (Fig. 12b). This approach requires a more complicated target design and also requires additional control electronics. For analysis of target performance, attention is restricted to the single target case. A small square array is included in the center of the target for alignment purposes.

D. TARGET DETECTION PROBABILITY AND FALSE ALARM RATE

Possible means of realizing a vernier detector of the type discussed above and capable of detecting a few photoelectrons per element include the use of charge coupled devices, diode arrays, similar to the Reticon, or intensified silicon vidicon targets with electron beam readout. Before discussing

these approaches, however, it is useful to examine the limitations on an ideal detector (one which adds no noise or uncertainty to signal detection) due to photon statistics and the background radiation environment in which the detector operates. Such an approach is also quite useful because practical detectors, particularly one based upon charge coupled device technology, can closely approach the ideal case.

In the ideal detector, the signal in one element due to a single electron is sufficiently large to be readily distinguished from any detector or electronic noise. The output signal which results as the individual elements are read out is fed to a threshold detector, which is triggered if a signal corresponding to N_T or more electrons in a single element is encountered. Detection of this event constitutes detection of the electron pulse. For low photoelectron numbers, the detection probability is determined by the photon statistics.

For a detector of 250 elements, each element corresponds to ~ 27 psec. In Part B, it was concluded that the electron bunch due to the return will have a Gaussian distribution in time with full width at half maximum of ~ 40 psec. Therefore, the return pulse will occupy approximately two resolution elements. It is therefore assumed that photoelectrons from a given pulse are equally spread over two resolution elements. The mean number of photoelectrons per resolution cell, $\overline{N}_e$, is then:

$$\overline{N}_e = \frac{\eta N_P}{2} \tag{19}$$

where η = photocathode quantum efficiency and N_P is the total number of photons at the vernier cathode in all 13 pulses of the pulse train (see Sec. IX).

The probability that a count is recorded in the resolution cell is the Poisson probability of N_T or more events when the mean is $\overline{N}_e$. The signal position is correctly registered, however, if either of the two resolution cells registers a count; therefore the detection probability is given by $1 - P^2_{ND}$, where P_{ND} is the probability that no pulse was detected in a resolution cell when one should have been. Figure 13 shows the detection probability derived in this way as a function of photons incident upon the photocathode. The value of η used is 0.06, typical of extended red multialkali photocathodes at 0.6943 μm. Above 150 photons in the pulse train, the detection probability is seen to be > 0.9 for thresholds ≤ 4.

Figure 13 describes the situation for the lowest signals encountered. Signal amplitude can vary by ~4 orders of magnitude (Sec. IX). At the highest signal amplitudes, photons in the "tails" of the Gaussian pulses may be sufficient to cause signals greater than threshold several elements away from the centroid of the pulse, leading to a large timing error. This problem can be avoided by utilizing a dynamic threshold; i.e., the threshold number can be controlled by the output of a peak detector to assure that in the strong signal case the centroid will be detected. For the strong signals, the fluctuations in numbers of photoelectron will be sufficiently small so that high detection probabilities can be maintained with $N_T \approx 1/2\ \overline{N}_e$. Alternatively, attenuation (dependent upon signal strength) can be introduced into the signal path to keep signal strength at a moderate level so this problem is not encountered.

The probability of a false count in the vernier system is determined by the number of background photons incident upon the vernier and the high energy particle flux. Considering first the background flux, let the number of

photoelectrons due to background flux be N_{BG}/sec and assume the target is gated for a time t_G. Then the mean number of background (and thermal) electrons is:

$$\overline{N}_B = (N_{BG} + N_{th})t_G. \tag{20}$$

The probability that N_T electrons strike any given resolution cell is (Ref. 13):

$$P(N_T \text{ in given cell}) = \frac{C(\overline{N}_B, N_T)\,(N_C - 1)^{\overline{N}_B - N_T}}{N_C^{\overline{N}_B}} \approx C(\overline{N}_B, N_T) \Big/ N_C^{N_T} \tag{21}$$

where N_C is the number of resolution cells (= 250) and $C(\overline{N}_B, N_T)$ is the number of combinations of $\overline{N}_B$ objects taken N_T at a time. Each of the resolution cells is statistically independent; so Eq. (21) must be multiplied by the number of cells which must be "searched" to find the true signal. The N_C resolution cells correspond to 6.67 nsec while the course detector gives the range time to within $\pm$ 1 nsec; therefore, provided suitable logic can be implemented to restrict the elements searched, the multiplier will be approximately $N_C/3$. Thus:

$$P_{FA}(N_T) = C(\overline{N}_B, N_T) \Big/ 3N_C^{(N_T - 1)} \tag{22}$$

For large $\overline{N}_B$ Eq. (22) gives sufficient accuracy; for small $\overline{N}_B$ the false alarm probability is given by:

$$P_{FA}(N_T) = \sum_{i=N_T}^{\infty} P_i \; C(i, N_T) \Big/ 3N_C^{(N_T-1)} \tag{23}$$

where P_i is the Poisson probability of i background events given that the mean is $\overline{N}_B$. $P_{FA}(N_T)$ is the expected number of false counts, or false count probability, per readout cycle.

False alarm probabilities calculated using Eqs. (22) and (23) for thresholds of 2, 3, and 4 are shown in Figs. 14 & 15 as a function of background photons at the photocathode. The target gate time is used as a parameter. Other parameters used in the calculation are $\eta = 0.06$ and $N_{th} = 1000$ electrons/sec. As would be anticipated, P_{FA} decreases as gate time and background flux decrease and as threshold increases. For the highest background flux encountered (10^8 photons/sec) P_{FA} can be kept below 10^{-3} by utilizing, for example, a threshold of 4 and gate time < 100 μsec (Fig. 15).

Cosmic ray events set a lower limit to P_{FA} at very low background levels and relatively long gate times. As discussed in Sec. IV, Part C, there is a flux of approximately 10 protons/cm^2-sec at the operational altitude. It is assumed that each proton event coupled to the photocathode causes > 10 photoelectrons, which would result in an above threshold signal for low thresholds, as considered in Figs. 14 & 15. In the present application, the photocathode can be relatively small; furthermore, the electron optics in the vernier tube assures that the photocathode area coupled to an active area on the target is approximately equal to the area of a resolution cell, which is 4.6×10^{-3} cm^2. Using an effective photocathode area of 0.1 cm^2 as a more conservative estimation, the false alarm probability due to cosmic rays is:

$$P_{FA} = \begin{cases} 3 \times 10^{-4} & t_G = 1 \text{ msec} \\ 3 \times 10^{-7} & t_G = 1 \ \mu\text{sec} \end{cases} \tag{24}$$

These limits are too small to appear on the scale of Figs. 14 & 15.

Gating of the vernier tube, if required, can be accomplished by use of a gating electrode internal to the tube, switched in response to a signal from the coarse detector or from other coarse range data. Alternatively, the target itself can be activated from a non-collecting to a collecting state, e.g., in the case of a charge coupled device target, the collecting wells can be turned on over the appropriate time interval and left off at other times.

It is important to note that Figs. 14 & 15 represent an upper limit to false alarm rate when some sort of dynamic threshold is incorporated at high signal levels, as discussed above. If a variable threshold is actually used, the false alarm rate is decreased as threshold increases, as illustrated by increasing threshold from 2 to 4 at a given gate time and background photon rate in Figs. 14 & 15. Alternatively, if variable attenuation as a function of signal level is introduced into the return beam channel and the threshold is kept constant, P_{FA} decreases in response to the reduced background photon rate.

These considerations, coupled with the detection probability curves of Fig. 13, indicate that adequate false alarm rate and detection probability can be attained for thresholds ≥ 3 for most mission conditions (Sec. IX). Sample measurement missions illustrating this are discussed below in Sec. IX.

E. IMPLEMENTATION OF THE VERNIER DETECTOR

There are several possible approaches to realizing the vernier detector target. (Attention is primarily focused upon the target structure alone since this item would require the most development. Photocathode technology and electron optics are sufficiently well in hand that they need not be treated in detail here.) The most attractive are all solid state approaches, i.e., utilization of charge-coupled-devices or pn junction diode arrays with solid-state readout. These approaches give the advantages, compared to electron beam readout tubes, of decreased power consumption and size, and increased reliability. Solid state arrays can be gated or activitated electronically, thereby eliminating the need to gate the tube at the photocathode, in order to obtain background suppression. However, imaging with targets which utilize electron beam readout, such as the silicon-intensified-target (SIT) tube is perhaps further developed at this time, and a target system of this type is also possible, but with somewhat reduced sensitivity.

1. CHARGE COUPLED DEVICE TARGET

A target based upon charge-coupled-device (CCD) technology is considered first. In such a target, the individual resolution elements of Fig. 11 would be formed by the depletion region of a metal-oxide-semiconductor capacitor, appropriately biased. When the silicon is bombarded by an electron of 10 - 20 KeV energy, a charge gain of 1500 - 2000 can be realized, as in the SIT tube. This charge is collected in one or two depletion regions and then clocked in a sequential fashion to an output preamplifier located on the target chip. At the output of this amplifier, a decision can be made as to whether or not the threshold number of photoelectrons were incident upon any given resolution cell.

There are at least two possible layouts for a target based upon CCD technology. The first is the obvious approach of dividing each resolution element into thirds along the circumferential direction (a three-phase CCD is assumed here and in the subsequent discussion) and utilizing the detector ring as a charge transport register as well as the detector. The second approach is patterned after that used in Fairchild's linear imaging array: after integration of the signal charge in the detector elements, the signal is passed to a separate charge transport array by a transfer gate. This type of arrangement is shown schematically in Fig. 16. This configuration would be the preferred one since it has smaller area in the transfer array, which reduces dark current noise and transfer noise. The layout of such a device may be more complicated than the first geometry mentioned, however.

As mentioned above, each photoelectron results in 1500 - 2000 electrons being collected by the CCD wells. Therefore, one or a few photoelectrons can be detected if the number of noise electrons introduced by the device itself is less than the one photoelectron equivalent number. There are three sources of noise of importance in the CCD detector: 1) dark current shot noise; 2) trapping state noise; and 3) preamplifier noise. It is most convenient to express these noises in terms of the number of RMS noise electrons per charge packet.

1) The number of RMS noise electrons due to dark current shot noise, n_d, is:

$$n_d = \left[\frac{A_D J \tau_i}{q} + \frac{A_t J \tau_t}{q}\right]^{1/2} \tag{25}$$

A_d = area of detector element = $4.6 \times 10^{-3} cm^2$

A_t = area of element in transfer register = $3 \times 10^{-4} cm^2$ for 0.3 mm x 0.1 mm elements

τ_i = signal integration time, or gate time

τ_t = total transfer time

J = dark current density = $5 \times 10^{-9} A/cm^2$ in state-of-art devices at room temperature

q = electronic charge

For τ_i = 100 μsec, τ_t = 250 μsec (readout time of 1 μsec for 250 elements)

n_d = 128 electrons RMS

For τ_i = 1 msec, this is increased by $\sim \sqrt{10}$ or

n_d = 405 electrons RMS

Because of the continual accumulation of dark carriers during the readout of the target, the last element contains more dark electrons than the first. With the numbers used above, the 250th element contains 2,300 more electrons than the first, or 1 - 2 photoelectron equivalents. Several possibilities exist to minimize this gradation so that it will not cause false counts; for example, increase the readout speed (decrease τ_t), divide the detector ring into several different parts with different preamplifiers for each, or cool the target to reduce J. Pehaps the simplest solution is to simply scale down the target size; reduction of scale by a factor of 2 reduces the electrode areas by 4 and drops this shading effect well below a single electron equivalent level.

2) For a surface channel CCD surface state trapping noise is given by:

$$n_{ss} = \left[N_{tr} \frac{A_t}{3} kT \cdot 1.4 \cdot N_{ss}\right]^{\frac{1}{2}} \qquad (26)$$

N_{tr} = number of transfers = 750

kT = Boltzmann's constant times temperature

N_{ss} = Surface state trapping center density = $10^{10}/cm^2$-eV.

With these values:

n_{ss} = 5,200 electrons RMS.

This large number, equivalent to the signal from several photoelectrons, results in the most part from the relatively large (compared to other CCD applications) electrode area required in the present detector and the assumption of a surface channel device. This large noise source can be avoided by utilizing a buried channel CCD, in which the signal charge is not in contact with the surface. In a buried channel device, bulk state trapping, analogous to surface state trapping, may occur. However, available experimental data on Fairchild CCD's, which use a buried channel, show no evidence of bulk state trapping noise, indicating that in such a device the trapping noise is one to two orders of magnitude less than in a surface channel device. Any bulk state trapping effects could be minimized by proper choice of clocking frequency or by use of a "slim zero", or small bias charge. Therefore, for a buried channel device, a conservative estimate of noise due to trapping effects is n_{ss} = 100 electrons RMS.

3) In present day CCD's amplifier noise is mainly determined by the uncertainty of resetting the floating output diffusion and amounts to ~220 electrons for a diffusion with capacitance of 0.3 pf. With correlated double sampling or floating gate amplification (i.e., more sophisticated output techniques), this number could be reduced to approximately 50 - 100 electrons.

The total RMS noise expected for the CCD detector is the RMS sum of the individual noises above, or:

$$n_{ss}^{T} = 275 \text{ electrons RMS (100 } \mu\text{sec gate time)}$$

$$= 470 \text{ electrons RMS (1 msec gate time)}$$

These values are well below the single electron level and indicate that the charge coupled device target with a threshold of three or more can function as a nearly ideal detector for the vernier system.

Another factor affecting the operation of the proposed CCD target structure is the relative large gate areas required. State-of-the-art CCD's have gate areas of $\sim 6 \times 10^{-6}$ cm^2 and can operate with clock frequencies up to $\sim$ 10 MHz. With larger gate areas, a greater charge transfer time must be used to assure that all signal charge is transferred at each step. This implies that slower clock frequencies may have to be used to maintain adequate charge transfer efficiency.

The proposed detector does incorporate many features which are very much state-of-the-art and would therefore require development effort. For use in the electron bombarded mode, the CCD must be illuminated from the rear; this requires thinning of the target to 10 - 20 μm and proper treatment of the back surface to attain good secondary electron collection efficiency. As has been noted, buried channel technology should be used. Obviously, special mask designs are required, and perfection must be maintained over a large silicon area, which may create yield problems. However, many companies are involved in CCD fabrication, and these problems do not appear insurmountable.

2. DIODE ARRAY TARGET

A second approach to an all-solid-state target utilizes a self-scanning, p-n junction, charge storage diode array, which is a combination of MOS microcircuitry and planar photodiodes. In such a device, diode charge is serially gated out a common video line. Devices are commercially available from Reticon Corporation, which have up to 2,500 elements and can operate at frequencies as high as 10 KHz. The Reticon device is capable of detecting the signal due to $\sim 10^5$ electrons (Ref. 14). Prototype devices have been built which show the feasibility of using a Bendix chevron channel electron multiplier to furnish the necessary electron gain (up to 10^7) to allow single electron events to be detected (Ref. 15). Application of such a device to the present situation would require the circular electron path be swept on the electron multiplier and secondary electrons would be accelerated directly onto the diode target, which would also be in the form of a ring. Some fraction of the photoelectrons would be lost due to dead area on the multiplier so this approach would have less sensitivity than a CCD device. Sufficient quantitative data does not appear to be available to analyze in greater detail the noise performance of this type of target arrangement. A potential drawback is that the electron flux bombarding the target diodes would be high, which may adversely affect the lifetime of the diodes.

A second possible approach to using serially scanned silicon diode arrays is that proposed by McMullan, et al. (Ref. 16). In this approach, a simple charge amplifier is associated with each sensing diode to provide a gain of ~ 10. This gain, in addition to electron multiplication gain in the sensing diode, allows individual photoelectron events to be detected. For a

prototype device tested, consisting of only one sensing diode of area 100 x 120 μm, the output due to a single photoelectron was 5 mV while noise amounted to ~ 2mV RMS. Leakage current contributed 1 mV to the output signal. Circuit arrangements for reading out a number of photodiodes sequentially have been proposed. For application of this technique to the vernier detector, two possible problems might arise. The detector area shown on Fig. 11 is ~ 40 times larger than that of the prototype device discussed above; since the dark current signal scales with area, the dark current signal would be ~ 40 mV compared to a 5 mV single electron signal. While this average dark current contribution could be subtracted out, element-to-element fluctuations, or noise, would also increase as the dark current signal increases. Scaling the target down by a factor of two so as to reduce detector area by a factor of four would decrease this problem as would cooling of the target slightly to reduce dark current (cooling to 25° below ambient reduces dark current by an order of magnitude). A second possible problem is the elimination of switching transients and capacitative coupling of unwanted signals to the output line, a problem which has plagued diode arrays in the past.

Before leaving the subject of all solid-state target and readout sections, a few remarks are in order concerning incorporation of such devices in tube structures. The target structures are similar to that used in a SIT tube; therefore, the technology used in such tubes should be directly applicable. Electronic-Vision Corporation of San Diego, makers of a photocathode–p-n junction device called the Digicon, have had considerable experience in operating solid state target structures in tubes similar to that

needed in the present situation. This company is presently developing tubes with Reticon and CCD targets.

3. SIT TYPE TARGET SYSTEMS

The final types of vernier tube systems to be considered are those which would incorporate electron beam readout of the charge storage target. There are many image tubes of this type, e.g., silicon vidicon, SEC vidicon, plumicon, etc., which, when coupled with an image intensifier or electron gain stage, can detect single photoelectron events. Here, to serve as an example of the capability of this type of system, attention is restricted to a tube of the silicon-intensified-target (SIT) type (Ref. 17). This particular device contains the electron gain stage, charge storage target and readout in one envelope and has been under development for several years. Single photon counting systems using other types of tubes which could potentially be adapted to the vernier target application are described in the literature (Ref. 18).

The SIT tube consists of a photocathode, electron acceleration section, silicon diode mosaic charge storage target and electron beam readout section. Resolution element size is typically 40 μm × 40 μm. The dominant noise contribution of the tube itself is from the video preamplifier; state-of-the-art values for preamplifier noise current are $\sim 1 \times 10^{-9}$ A RMS over a 1 MHz bandwidth. Silicon vidicons (without intensification) have been reported to be able to detect 1000 charge carriers/resolution element with a signal-to-noise ratio of 1. With ~ 2000 gain due to the electron multiplication process, ~ 1 photoelectron per resolution element should be detectable.

For adaptation to the vernier detection system, there are two possible approaches. In the first, the target would remain the same as in any SIT tube, i.e., a square or rectangular array of typically 6×10^4 resolution elements. For any one vernier measurement, the signal charge would be spread over an area (assuming a target ring scaled down by a factor of 2 from Fig. 11) of 225 μm x 200 μm. The first number, the circumferential spread, is the distance traversed by a 40 psec pulse while the second figure is based upon a dynamic image tube resolution of 5 lp/mm (it is assumed that deflection voltage fluctuations are unimportant during the ~ 100 nsec of a single measurment). Thus the area covers ~ 27 - 40 μm x 40 μm resolution elements; or the signal photoelectrons are spread over this many resolution elements. To detect the presence of a signal, given that it takes ~ 1 electron/resolution element for a signal-to-noise ratio of one, on the order of 27 signal photoelectrons would be required. This is because, if a threshold is set to be > 1 to suppress false counts due to preamplifier noise or background photoelectron events, a large number of photons must be supplied to assure that a few of the resolution elements have received more than the threshold number of photoelectrons. Or, if the threshold is one and the signal is separated from noise events by looking for a closely spaced bunch of photoelectron occurrances, ~ 27 photoelectrons would have to be supplied to constitute a statistically significant bunch. In either case, a small computer would probably be required to handle the data from the large number of picture elements. Of course, since the area in which the signal is likely to be found is only a small portion of the target area, the number of elements searched would be reduced. The center of the electron ring on the target

would also have to be determined in a calibration step. While the detection probability and false alarm curves (Figs. 13-15) derived for the ideal vernier detector would not apply to the situation just described, it is apparent from the above discussion that such a system would not be as sensitive as the ideal detector or an all solid-state system. Another potential drawback of this approach is, if the frame rate is on the order of standard TV rates ($\sim$ 16 msec/frame), readout could not take place between outgoing and return pulses and one of the schemes indicated in Fig. 12 would have to be used to distinguish outgoing and return pulses.

The second approach to using an electron beam readout system is to build a specialized tube including a diode array target as in Fig. 11 which is read out by a circularly scanned electron beam. The area of a resolution element (again assuming a target scaled down by a factor of 2 from Fig. 11) would be 1.15×10^{-3} cm^2, or 72 times as large as the resolution cell size of a standard silicon vidicon. The elemental capacitance, which scales with area, would then be 72 times larger also. Now signal current, I_s, is given by

$$I_s = \frac{Q_s}{\tau} \tag{27}$$

where Q_s is the signal charge of an element and τ is the time it takes to read out the element. $\tau = C_{el}R_B$ where C_{el} is the elemental capacitance and R_B is the equivalent electron beam resistance. Assuming R_B remains about the same, the signal current is decreased by 72 times compared to a conventional silicon vidicon target element which has the same signal charge. Also the bandwidth required is reduced as τ increases so that noise decreases; signal-to-noise ratio is proportional to $\sqrt{\tau}$, or is reduced in the

present example by a factor of 8.5. Therefore, if again it takes ~ 1 photoelectron/resolution cell in the conventional tube to give S/N = 1, it will take ~ 8.5 photoelectrons in the vernier target. Since it is desirable to operate with S/N > 1, even more signal photoelectrons are required. Again it can be concluded that such a system is less sensitive than the ideal vernier detector and all solid state target structures. Addition of another intensification stage may be able to improve this sensitivity at the expense of system complexity.

4. IMAGE DEFLECTION AMPLIFIER

The general image deflection requirements will now be addressed. The VHF image deflection amplifier has to deliver about 200 volts RMS to the deflection plates assuming typical image deflection sensitivity of about 400 V/cm and a 2.5 cm diameter target ring. The actual electronic configuration would basically consist of a frequency multiplier chain to convert the stable clock fundamental frequency to 150 MHz, a stepped attenuator to adjust the amount of deflection, a quadrature deflection amplifier and a helical resonator tank circuit. The final drive should be balanced and the anode of the vernier detector tube should be at ground potential. The amount of rf power needed to drive the vernier detector should be less than 5 W from past experience and should be gated to reduce rf dissipation in the tube. The above requirements could be easily met with current transistor technology.

VI. LASER TRANSMITTER

A. GENERAL

The constraints on the system most directly determining the choice of components and operating parameters are:

pulse width:	$\approx$ 25 psec
weight	$\sim$ 200 pounds
power input:	< 1 kW
lifetime:	one satellite mission - 1 week.

The range requirements, along with weight and other limitations on large receiver optics, implies a transmitter output energy for the pulse train of 0.03 to 1.0 Joule in the visible to infrared region of the spectrum. A choice for the laser depends then upon (1) its efficiency, since for pulsed lasers a large fraction of weight will be in storage capacitors, the weight of which will be limited by permissible system weight, and (2) wavelength, since the detector efficiency, diffration losses, and transmission-path absorption are all wavelength dependent. An additional option is wavelength conversion, e.g. a second-harmonic generator at the laser transmitter. Conversion efficiency then offsets other wavelength-dependent gains.

B. NEODYMIUM VERSUS RUBY SYSTEMS

System range resolution specifications require a Gaussian shaped pulse with a 20 - 50 psec FWHM width. At the energy levels required, only mode-

locked Q-switched neodymium lasers at 1.06 μm and ruby at 0.6943 μm would suffice (dye lasers are ruled out by reliability and lifetime factors).

Power input then implies a maximum repetition rate for laser firing. Electrical-to-optical efficiency of the lasers under consideration is low; it must be assumed therefore that cooling capacity equal to the power input is also available.

The choice between ruby and neodymium lasers requires comparisons of efficiencies, material damage thresholds, mode control, and reliabilities. At the power and energy levels contemplated, good transverse beam mode control is necessary, in turn necessitating a laser oscillator at low power followed by a higher-power amplifier. Beam-expanding optics between the units reduces damage to the later stage; energy outputs of the required levels are otherwise possible in single-stage oscillators.

In both ruby and neodymium (in glass) systems, the energy-outputs required do not reach saturation levels in the active optical media. It is thus useful to obtain multiple pulses out from the system during a single excitation pulse. Thus the original prototype system (Ref. 1) selected a single mode-locked pulse from a Q-switched envelope; if a sequence of these mode-locked pulses could be used, the available energy at the detector would be multiplied by the number of pulses used. Given some way to identify the individual pulses in the Q-switched envelope in order to determine range properly, an increase

in the number of pulses used permits a reduction in total (Q-switched envelope) pulse energy for a given detector sensitivity (with the exception that, for some detection schemes, each sub-pulse must have adequate energy for a statistically significant individual detection at the receiver). For both neodymium and ruby, a Q-switched envelope would be ~ 80 nsec (10% full width); if the vernier is synchronized at 150 MHz to the transmitter (mode-locked pulse repetition rate) the inter-sub-pulse period is 6.67 nsec and the increase in useful energy with a whole pulse train, referred to a single sub-pulse selected at the Q-switched envelope peak, would be a factor of ~ 7.

For a total energy output of 0.3 joules, sub-pulse energy would be ~ 43 mjoules at the envelope peak. For a mode-locked pulsewidth (sub-pulse width) of 25 psec, we have a peak sub-pulse power of 1.8×10^9 watts. This number is important, and thus requires more careful computation based on system details and actual pulse-envelope shapes, because material damage is fundamentally limited at power densities of 1 to 10×10^9 W/cm^2 (Refs. 19, 20, 21), and typical laser rods have cross sections of ~ 1 cm^2.

Discussion of high power ruby and neodymium mode-locked Q-switched lasers is available in the literature, (Refs. 22, 23) in manufacturers specifications, (Ref. 24) and from individuals (in particular, those involved in recent laser-fusion research for the AEC). Neodymium is available in two hosts: yttrium aluminum garnet (YAG) and

laser glass. Gain is higher in YAG; energy storage is better in glass; and, additionally, large rods are not readily available of YAG as of glass. (Refs. 22, 23). Thus the systems to be compared are a ruby oscillator-amplifier and an Nd: glass or YAG oscillator with Nd: glass amplifier.

Nd and ruby systems are easily capable of supplying 30 psec-wide pulses when mode-locked due to their very broad gain frequency bandwidths. Ruby pulsewidths of 2 to 5 psec have been obtained; (Refs. 25, 26, 27, 28) in Nd: glass, 3 to 8 psec are typical with signs of subpicosecond substructure (Refs. 29 - 33). Such excessively narrow pulses are disadvantageous for two reasons: (1) at a given energy, narrower pulses imply a higher peak power and greater materials-damage problems; (2) narrower pulses imply greater bandwidths and thus a larger receiver filter bandpass with consequent smaller signal/noise improvement possible by optical filtering. For example, a bandwidth-limited 3 psec pulse (FWHM, Gaussian) corresponds to 6 Å at 1.06 μm and 2 Å at 0.6943 μm; a 20 psec pulse, to 0.9 Å at 1.06 μm and 0.4 Å at 0.6943 μm. Due to high-power nonlinear effects in Nd: glass systems, e.g. self-phase modulation, and chirping, (Ref. 34) actual bandwidths encountered approach 150 Å.

Nd systems generally show short-pulse behavior; ruby systems do so only with some effort. The desired pulsewidths and bandwidths might be achieved with a Nd laser by appropriate optical (perhaps interferometric) bandpass filters, which would probably be required in

laser oscillator and amplifier. In a ruby system, a prudent choice of resonator and Q-switching mode-locking dye and solvent would suppress too-short pulse behavior.

The second-harmonic (SH) of 1.06 μm of Nd appears attractive. Constrained to transparent photocathodes for the vernier detector, we can obtain greater detector quantum efficiency by a factor of approximately 20 at 0.53 μm as at 1.06 μm; the cost of conversion to SH is an efficiency term at the transmitter of 0.15 to 0.25 (Refs. 35, 36). There would be a reliability trade-off at the transmitter: the SH-generating crystal would be exposed to very high peak powers, but successive optical elements would see much-less-damaging power levels; the addition of a SH crystal would increase somewhat the system alignment complexity. Some increase or decrease (more probable here) (Refs. 36, 37) in SH sub-pulse width with respect to fundamental pulse-width is expected.

One other consideration is relevant to the choice of laser type: electrical-input-to-optical-output efficiency. The Nd: glass laser is expected to more efficiently use pump power than the ruby laser. For example, in Korad's K-1300 laser system, which is available with either Nd or ruby active media, the ruby output is 0.3 that of the Nd output (Ref. 24). Thus the overall electrical-input to photodetector-count-rate efficiency is expected to be comparable for ruby and Nd SH. These data are tabulated in Table 3, ignoring any wavelength-dependent focussing or diffraction effects and transmission-path absorption.

Table 3. Relative Laser System Efficiencies

λ μm	Quantum efficiency for transparent photocathode	Relative detector input photon rate φ	Relative energy φ/λ	Transmitter wavelength-conversion efficiency	Relative laser energy required for constant detector electron rate	Estimated relative laser pump efficiency	Relative pump energy required for constant detector electron rate
1.06	0.0006	100	65	(1.0)	65	1.0	~20
0.6943	0.06	1.0	1.0	(1.0)	1.0	0.3	1.0
0.53	0.10	0.6	0.79	0.15 - 0.25	~4	1.0	~1.3

Two reasons point to ruby as the choice: first, for given input energy, a lower peak amplifier power (by a factor of 3 to 4) is necessary in ruby, and additionally the damage threshold for ruby itself is expected to be higher because the nonlinear index, upon which self-focussing depends, is higher by a factor of 2 for ruby (Ref. 20); second, greater ease is expected in obtaining proper-width (30 - 50 psec) sub-pulses. It is therefore suggested that a ruby laser oscillator-amplifier system be selected.

C. RUBY SYSTEM

1. OSCILLATOR AND AMPLIFIER

No system is presently available in the laboratory or commercially which exactly fulfills our present requirements, and interpolations, extrapotations, and informed guesswork is necessary. This is based on experience with older ruby lasers in laboratory service, available data on the latest commercial equipment, (Ref. 24) and data in the literature (Refs. 25 - 28). To minimize the possibility of materials damage, the laser beam must be maintained in a smooth TEM_{oo} transverse mode. This can most readily be achieved in a low-power oscillator, utilizing an appropriate resonator structure, to be followed by an amplifier stage.

Design of the laser amplifier lead would be conventional (Ref. 24). Several designs for the oscillator must first be compared experimentally. These designs (Refs. 25 - 28) all entail either ring-cavity construction or inverting lenses inside the optical cavity to obtain reliable TEM_{oo} mode structure and permit short sub-pulses. The required Q-switching and mode-locking is accomplished by the insertion of a dye cell; appropriate dyes and

solvents are cryptocyanine in acetone for 20 psec sub-pulses and dicyanine A in dimethyl sulfoxide for 50 psec pulses.

A slight expansion of the beam diameter before amplification would reduce the peak power density in the later optical elements. A rough target of 30 mjoules per Q-switched train of mode-locked pulses from the oscillator and an amplifier gain of ten for a final envelope energy of 0.3 joule seems conservative enough to allow for slight optical losses in the polarization switch (15 to 20%).

2. POWER SUPPLIES

Until experimental verification is possible, a flashlamp input energy to each stage of 5 kjoules should be allowed, for a total capacitor storage capability of 10 kjoules. These capacitors will comprise the largest fraction of the system weight. Commercial pulse-discharge capacitors are available with an energy density of up to 125 joules/pound, implying at 10 kjoules a minimum capacitor weight of 80 pounds. A more conservative storage density of 50 joules/pound results in a weight of 200 pounds.

The capacitors considered were Maxwell Laboratories, Inc., Series M units (Ref. 38); maximum energy density is achieved in the 35 μF, 5kV units, requiring 23 units for 10 kjoules at 5 kV. The significant trade-off to be considered here is lifetime versus weight, since maximum energy density is achieved at higher voltages and shorter lifetimes; the 125 joules/pound rating is achieved at a lifetime of 5000 charge-discharge cycles (2 percent failure rate). The lifetime of a 23-unit supply is significantly shorter since, without great care in paralleling the units, a single capacitor failure may trigger

other unit failures and thus the irreparable failure of the entire power supply. The use of high-voltage, de-rated units increases lifetime substantially. However, the life estimates available are based on very limited data and further information must be acquired before flying these units (Ref. 39).

The failure mode of these capacitors is dependent on attitude and geometry, and is uncertain for satellite use (Ref. 39). Catastrophic failure must be anticipated with some safety measure to protect from small case shrapnel; a lightweight fiberglass container should suffice. Overall weight of the capacitors and inverter power supply is estimated to total 100 to 200 pounds. With an estimated weight per laser stage head of 10 pounds and for the modulator (polarization switch) of 15 pounds, the transmitter system exclusive of main supporting frame should weigh in at about 140 - 240 pounds. The average was used in Section 10.

3. POLARIZATION SWITCH

In order to identify the individual sub-pulses, it has been proposed that the polarization of a selected sub-pulse be rotated 90 degrees. The polarization switch would be less susceptible to damage if placed between the laser oscillator and amplifier stages. Typically ruby laser outputs are linearly polarized due to the placement of optical surfaces at Brewster's angle to reduce reflection losses and, in some cases, due to the alignment of the crystalline c-axis of the ruby rod normal to the rod axis. Here the oscillator would be linearly polarized by Brewster elements and by a 90°

ruby rod; the amplifier would have optical surfaces normal to the beam, antireflection-coated if necessary for low loss (and if available for required power levels) and an unpolarized 0° ruby rod. The polarization switch should be constructed of KD*P for its high electro-optic coefficient and high-power damage threshold. It would immediately follow the laser oscillator and precede the beam expander and laser amplifier. It's design would substantially follow Ref. 40. A z-cut longitudinal KD*P crystal would be fed a high voltage through a Krytron switch-tube which in turn is fired by an avalanching-transistor circuit.

4. RESONATOR STABILITY

In order for the separate sub-pulses in a single Q-switched envelope to appear at the same point on the detector vernier display, the vernier sweep rate must be accurately synchronized to the laser oscillator resonator's beat frequency (i. e. the sub-pulse repetition rate). Since the adjustment of the vernier frequency is difficult, the resonator beat frequency must be set to the vernier frequency.

For an integrated return image spread of $\pm$ 5 psec over a duration of sub-pulses of 100 nsec, we require a fractional frequency match of $\pm 5 \times 10^{-5}$. For a vernier frequency of 150 MHz, the resonator (optical) length would be one meter, requiring an accuracy in length of $\pm$ 50 μm (or $\pm$ 2 mils). The resonator could readily be manufactured to the approximate length and final alignment made <u>in situ</u> with conventional micrometer adjustments.

The resonator optical length, and beat frequency, will be dependent on temperature through the thermal expansion and refractive-index coefficients of the elements. This effect enters from two sources: temperature changes of the environment, and time-dependent temperature of the elements during the laser-firing from absorbed optical pump power. If the ambient change is + 10°C, typical materials expand fractionally by 1 to 2 x 10^{-4} and Invar and fused silica by 1 x 10^{-5}, so that no length corrections would be necessary; for $\pm$ 100°C (unlikely for a manned system), micrometer corrections would be required and adequate. The adjustments would be made by observing the spread of pulses on the vernier display during a test firing and adjusting the pre-calibrated micrometer(s) on the resonator to correct the spread on successive shots.

The more serious problem is the beat-frequency sweep in time during the Q-switched pulse due to heating of the resonator optical elements by the laser pump. This effect has two components: the change in mean beat frequency due to thermal drift from a cold resonator to the mean time of output of the pulses; and the sweep of the beat frequency during the Q-switched envelope. The former is greatest, but can be compensated by an adjustment of the micrometers if the length change is reproducible, i.e. if the laser firing rate is held constant so that conditions are reproduced from shot to shot. The second component is not readily compensated and must therefore be minimized by optimum choice of materials.

The fractional beat frequency shift is

$$\frac{df}{f} = -\frac{\sum_i \frac{1}{n_i L_i}\left(\frac{1}{n_i}\frac{\partial n_i}{\partial T} + \frac{1}{L_i}\frac{\partial L_i}{\partial T}\right) dT}{\sum_i \frac{1}{n_i L_i}} \tag{28}$$

in which n is refractive index, L length, T temperature, f beat frequency, and the summations are over i optical resonator components. Temperature change of a component is dependent on the absorbed energy $d\epsilon$:

$$dT = \frac{d\epsilon}{mVs} \tag{29}$$

for element volume V, density m and specific heat s. Assume:

laser resonator length	$\approx$ 1 m
ruby rod volume	$\approx$ 10 cm^3
" " length	$\approx$ 10 cm
s	$\approx$ 0.2 cal/gm° C
m	$\approx$ 4 gm/cm^3
20% pump power absorbed in rod:	
$d\epsilon$	$\approx$ 1 kJ

Then $dT \sim 30°$ C and $df/f \approx -5 \times 10^{-4}$. This shift is likely to occur over a pump time constant of greater than 1 msec, so that the fractional shift during 100 nsec is only -5×10^{-8}. The sweep <u>during</u> the Q-switched pulse is thus negligible; but the <u>fluctuation</u> in <u>delay</u> from initiation of pumping until Q-switched pulse output must be less than 0.1 msec in order that the uncertainty in the beat frequency be less than 5×10^{-5}. This is a reasonable expectation.

VII. LASER BEACON TRACKING SYSTEM

The tracking requirements of the output and receiving optics associated with the receiver field of view, transmit beam divergence, and atmospheric refractions exceed typical inertial system accuracies. The actual tracking requirements needed for this particular application are from $2 \times 10^{-5} - 5 \times 10^{-5}$ radians which is well within the state of the art. The microwave interferometer (Ref. 41) beacon tracking being proposed for the ATL satellite could provide the necessary tracking function with the possible exception of alignment of the microwave and laser system with minimum boresight errors. The possible uses of this system should be investigated in more detail with special emphasis placed on holding a boresight tolerance of $\pm 5 \times 10^{-5}$ radians.

An alternate approach is to incorporate a laser beacon tracking system into the precision laser rangefinder. The basic requirements of the system are that it be capable of operating in high background environment with the desired tracking accuracy, of driving a 30 cm diameter mirror at a maximum rate of 2.3 degrees/sec, and of acquiring the retroreflector beacon in about 10 sec.

The RMS tracking accuracy of a diffraction limited system is (Ref. 42)

$$\text{pointing error} \cong \frac{1.22\lambda}{D_r} (S/N)^{-1} \tag{30}$$

where λ is the laser wavelength, D_r is the diameter of the receiving optics and S/N is the signal to noise ratio of the optical tracking system. The

potential tracking accuracy of a 1.06 μm system should be better than $\pm 8 \times 10^{-6}$ radians assuming 16 cm receiving optics.

In order to evaluate approximate power requirements of a beacon tracking system, a representative 1.06 μm system will be analysed. The laser transmitter is assumed to be square wave modulated at a rate of about 10 KHz with a receiver information bandwidth of 100 Hz. For the desired 2 to 5 degrees/sec tracking rate, 10 Hz bandwidths could be used. The received power can be expressed as

$$P_{rec} \geq \frac{P_{beacon} G_t(\theta_t) A_r T_{sys} T_{atm}(60°)}{4\pi R_{max}^2} \qquad (31)$$

where A_r is the ATL beacon receiver optics area, T_{sys} is the total system loss, T_{atm} is the atmospheric transmission coefficient, R_{max} is the maximum slant range between the spacecraft and laser beacon, and P_{beacon} is the laser beacon power needed to perform the mission.

The equivalent beacon antenna gain is expressed in the form

$$G_t(\theta_t) = \frac{16 \exp\left[-\left(2\theta_t/\alpha_t\right)^2\right]}{\alpha_t^2} \qquad (32)$$

where α_t is the full width (1/e) beam divergence, and θ_t is the line of sight pointing angle to the tracking receiver and is equal to $G_t(0.1°) = 4.54 \times 10^5$ if we assume the beacon is pointed at the spacecraft with an accuracy of ± 0.1 degree. The beam divergence is assumed to be $2\theta_t$. The above formulation can be derived from the definition of antenna gain and assuming a Gaussian radiation pattern. The received power is

$$P_{rec} = 6.93 \times 10^{-12} P_{beacon} \tag{33}$$

when

$$A_r = 180 \text{ cm}^2$$
$$T_{sys} = 0.1$$
$$T_{atm}(60°) = 0.2, \text{ hazy conditions}$$
$$R_{max} = 1.37 \times 10^8 \text{cm}$$

The background radiation is equal to (Ref. 43)

$$P_b = \frac{H_{\lambda s} B_o \alpha_r^2 A_r T_r \rho}{4} T_{atm}(0°)\, T_{atm}(60°), \text{ W} \tag{34}$$

where $H_{\lambda s}$ is the solar spectral irradiance incident on the atmosphere ($W\,cm^{-2}/Å$, B_o is the passband of the optics receiver filter (Å), α_r is the receiver field of view (rad), T_r is the transmission coefficient of the receiving optics, $T_{atm}(\theta_z)$ is the atmospheric transmission coefficient, θ_z is the zenith angle of the laser path, and ρ is the reflection coefficient of the earth. The resulting background is

$$P_b = 7.88 \times 10^{-10} \text{W} \tag{35}$$

when

$$B_o = 1Å$$
$$H_{\lambda s} = 6.5 \times 10^{-6} \text{W cm}^{-2}/Å$$
$$T_{atm}(0°) = 0.44$$
$$\rho = 1$$
$$\alpha_r = 1.75 \times 10^{-2} \text{rad}$$

The signal to noise ratio can be written as

$$(S/N) \approx \frac{\beta P_{rec}^2}{2eBP_b} \tag{36}$$

when one assumes the noise is caused by the background and where e is equal to the charge on an electron, β is the responsivity of the photodetector (A/W), and B is the signal bandwidth.

The resulting signal-to-noise ratio is S/N = 16 dB assuming a laser power of 1W, typical detector responsivity of 0.017 A/W and a signal bandwidth of 100 Hz. The conclusion is that the beacon system is feasible with current components and the approximate specifications are shown in Table 4.

Table 4. Beacon Specifications

Laser power	~ 1 W
Tracking accuracy	= ± 0.1 deg
Tracking rate	= 2.3 deg/sec
Field of view	± 0.5 deg
Acquisition time	~ 10 sec

VIII. RETROREFLECTOR ARRAY SYSTEM

A. GENERAL

The configuration and design of the retroreflector array system is extremely important in picosecond laser rangefinder applications, since pulse stretching can degrade measurement accuracy. An accurate determination of the physical location on the array which corresponds to the lead edge or centroid of the return pulse is needed for the various geophysical applications. The return signal can be expressed in the following functional form:

$$P_{rec}(t) = K\sum_{n-1}^{N}\sigma_n(\phi_n)P_{laser}(t-t_n), \text{ watts} \tag{37}$$

assuming that the incident radiation is uniform across the array, the phase centers of the individual elements are randomly distributed, and the optical position of each element remains constant during the pulse.

The equivalent radar cross section of the nth element can be expressed in the following functional form

$$\sigma_n(\phi_n, \theta_R) = \frac{16\, f(\phi_n)A_n \exp\left[-(2\theta_R/\alpha_n)^2\right]}{\alpha_n^2} \tag{38}$$

assuming a gaussian radiation pattern and where α_n is the return beam divergence, θ_R is the angle between the incident and return beams which is caused by satellite motion, A_n is the capture area, ϕ_n is the angle between the incident beam and normal vector to the element surface, and $f(\phi_n)$ is the reflectance of the corner cube at a tilt angle of ϕ_n.

The transmitted laser pulse is $P_{laser}(t-t_n)$ where t_n is the round trip transit time to the nth element in the retroreflector array. The factor K can be expressed as

$$K = \frac{G_t(\theta_t)\, A_r T_r T_t T_{atten}}{(4\pi R^2)^2} \left[T_{atm}(0^\circ)\right]^{\frac{2}{\cos\theta_z}} \tag{39}$$

where $G_t(\theta_t)$ is the equivalent antenna gain of the transmitting optics, A_r is the receiving optics capture area, T_r is the transmission coefficient of the receiving optics, T_t is the transmission coefficient of the transmitting optics, T_{atten} is the transmission coefficient of the receiver attenuator, $T_{atm}(0^\circ)$ is the atmospheric transmission coefficient at the zenith, θ_z is the zenith angle of the laser beam, and R is the slant range to the retroreflector.

If the retroreflector does not produce pulse stretching, the return signal is an identical replica of the outgoing pulse and can be expressed as

$$P_{rec}(t) = K P_{laser}(t-t_o)\, \sigma_R(\theta_R) \tag{40}$$

where $\sigma_R(\theta_R) = N\sigma_o(0, \theta_R)$, and N is the total number of elements.

Both planar and spherical array configurations were considered. Because of more stringent pointing requirements with a planar array, active ATL tracking would be required. The spherical array concept requires no active tracking; however, leading edge detection is needed. Since the average rise time of the return pulse is approximately equal to the laser pulse width, the timing resolution of the system could be degraded if 25 to 50 psec laser pulses were unattainable. The size of the spherical array is dictated by the

desired number of photons/cell needed for detection and is limited by the maximum return pulse width which does not overlap one cycle of the vernier sweep. Two color ranging to a spherical retroreflector may be impractical because of the resulting pulse spreading. The spherical array concept is also impractical in daylight operations because of the wide beam divergence (90 - 120 degrees) and corresponding power requirements of the laser beacon transmitter.

B. PLANAR RETROREFLECTOR ARRAY

For the purpose of this study, the planar array seems to be the best technical approach because of minimum return pulse spreading and output power requirements needed for the laser beacon. For simplicity, the laser pulses will be assumed rectangular in shape with an original width of 25 psec. The change in pulse width from a planar retroreflector array is

$$\Delta t_R = \frac{2d_{retro}\sin(\phi)}{c} \tag{41}$$

where ϕ is angle between the array normal and the incident laser beam, c is the velocity of light and d_{retro} is the diameter of the retroreflector array.

For example, an array 36 cm in diameter, a laser pulse width of 25 psec, and a return pulse width of less than 50 psec results in a pointing requirement of

$$\Delta\phi = \pm 0.6^\circ.$$

At least 6 sequential range measurements per retroreflector or 6 sets of four simultaneous measurements are required for surface distance reconstruction. An angular coverage of 120 degrees is needed to perform at least 6 range measurements if we assume an orbital altitude of 1.85×10^7 cm,

an orbital velocity of 7.5×10^5 cm/sec and a measurement rate of one measurement every 14 seconds. Active tracking is needed.

The change in laser return pulse length will be equal to or less than 4 psec with a pointing accuracy of $\pm$ 0.1 degree. In the laser rangefinder system calculations a more conservative $\pm$ 0.6 degree was assumed.

The mount should be designed so that the optical center of the retro-reflector remains fixed in space as the array is tracking the ATL satellite.

The basic ground retroreflector system is shown in Fig. 17 and consists of the planar retroreflector array, S-band beacon tracking radar and laser beacon as a retroreflector tracking aid. The ATL system would include a 5 to 10 Watt S-band beacon which the retro system could track. The approximate system requirements are listed in Table 5.

Table 5. S-Band Tracking System Parameters

ATL antenna gain,	G_t^s	= + 10 dB
Ground antenna gain,	$G_r^s(\theta_s=30^\circ)$	= + 5 dB
Wavelength,	λ_s	= 10 cm
Bandwidth,	BW	= 1 KHz
Noise figure,	NF	= 6 dB
System loss,	T_{sys}	= -15 dB
Transmitter power,	P_{trans}	= 10 W
Maximum range,	R_{max}	= 1.5×10^8 cm
Course tracking,	$\Delta\theta_{course}$	= 6°
Tracking accuracy,	$\Delta\theta_{fine}$	= 0.1°
Signal/Noise	S/N	= 12.3 dB
Acquisition time	τ_{acq}	= 20 sec

C. SPHERICAL RETROREFLECTOR ARRAY

The design of a spherical retroreflector array is twofold. First, the radius of the reflector is dictated by the number of photons per resolution cell needed for detection. The active reflecting area of the array is approximately

$$A_{act} \approx 2 \pi r_{retro} \Delta R \tag{42}$$

where r_{retro} is the radius of the spherical array, and ΔR is the desired range resolution. For a 200 cm retroreflector and a 4mm range resolution, the active area is 503cm^2. The increase in the return pulse width is governed by the radius of the array and the desired angular coverage and is equal to

$$\Delta t_R = \frac{4r_{retro}}{c} \sin^2\left(\frac{\theta_{max}}{4}\right) \tag{43}$$

where θ_{max} is the full width angular coverage.

The return width would therefore be equal to 3.9 nsec for an angular coverage of $\pm$ 90 degrees.

The second design criterion is that the return pulse does not overlap the vernier receiver sweep period. The pulse encoding and decoding scheme shown in Fig. 12a is impractical because of pulse overlap.

The total area of the array is

$$A_R = 2\pi r^2_{retro}\left[1 - \cos\left(\frac{\theta_{max}}{2}\right)\right] \tag{44}$$

and is equal to 7.36×10^4 cm^2 for θ_{max} = 90 deg. Assuming an individual retro cube area of 20 cm^2, a packing factor of 91%, 3349 retro cubes are needed for the above design.

The spherical array concept has potential, however, for wide angular coverage and daylight operations, the design becomes large, expensive and places severe system requirements on the laser beacon transmitter.

IX. SYSTEM PERFORMANCE

A. SPECIFICATIONS

The expected performance of the precision rangefinder system will now be calculated. The output pulse train is assumed to be made up of 13 Gaussian shaped pulses with (FWHM) widths of 23.5 psec or an equivalent rectangular pulse width of 25 psec. The distribution of pulse amplitudes is also assumed to be Gaussian with a width equal to 8.0 nsec between 10% points or equivalently 44 nsec (FWHM). The energy in the entire train is 0.3 joule, and the separation between adjacent pulses is adjusted to 6.6667 ± 0.0007 nsec.

The system specifications are given in Table 6. These specifications may not be optimum for a specific application, however, the performance calculations will demonstrate that the flight test objectives can be easily met with the postulated characteristics. The system parameters are with the state-of-the-art for laboratory devices. Some R and D effort is needed to space qualify the various system components.

Table 6. ATL Rangefinder System Specifications

Wavelength	$\lambda = 0.6943\mu m$
Total energy in train	$E_T = 0.3$ joules
Energy in largest pulse	$E_p = 0.0437$ joules
Peak power	$P_p = 1.75 \times 10^9$ watts
Rectangular pulse width	$t_p = 25$ psec
Maximum pulse rate	5 pulse/min.
Bandwidth	$B_o = 3$ Å
Transmission coefficient of trans. optics	$T_t = 0.5$
Transmission coefficient of rec. optics	$T_r = 0.1$
Return attenuator	$T_{atten} = 0$ to 30 dB
Receiver area	$A_r = 180\ cm^2$
Retroreflector area	$A_r = 1000\ cm^2$
Transmit beam divergence	$\alpha_t = 2 \times 10^{-4}$ rad
Retroreflector beam divergence	$\alpha_r = 1 \times 10^{-4}$ rad
Receiver field of view	$\alpha_r(0.6943\mu m) = 4 \times 10^{-4}$ rad
Receiver field of view	$\alpha_r(1.06\mu m) = 1.75 \times 10^{-2}$ rad
Polarization loss (coarse)	$T_{pol} = 0.5$
Polarization loss (vernier)	$T_{pol} = 1.0$
Solar spectral irradiance	$H_{\lambda s}(0.6943\mu m) = 0.137 \times 10^{-4}\ W\ cm^{-2}/Å$
Bore sight alignment	$\theta_{bore} = \pm 5 \times 10^{-5}$ rad
Optical beacon tracking accuracy	$\theta_{track} = \pm 5 \times 10^{-5}$ rad
Tracking rate	$\frac{\Delta\theta_z}{\Delta t} = 3$ deg/sec

B. BACKGROUND RADIATION

The background radiation from a reflecting earth that reaches the various detector photocathodes can be expressed as

$$P_b^{V,C} = 1.26 \times 10^{18} \lambda(\mu m) H_{\lambda s} B_o \alpha_r^2 A_r T_r \rho \cdot T_{atten} T_{pol} \left[T_{atm}(0^\circ) \right]^{(1+1/\cos\theta_z)}, \text{ photons/sec} \tag{45}$$

where $H_{\lambda s}$ is solar spectral irradiance incident on the atmosphere, B_o is the passband of the receiver optical filter in Å, α_r is the receiver field of view in radians, A_r is the collecting area of the receiver telescope in cm^2, T_r is the transmission coefficient of the receiving optics, T_{atten} is the transmission coefficient in the receiving optical path, T_{pol} is the polarization loss, $T_{atm}(0^\circ)$ is the atmospheric transmission coefficient at the zenith, θ_z is the zenith angle and is defined in Fig. 18, and ρ is the earth reflection coefficient.

For the worst case background, the sun is assumed to be directly overhead of the retroreflector. For the course range detectors a polarization loss of 0.5 is assumed since the Glan-Thompson prism will only pass 50% of a random polarized background. The vernier receiver background calculation assumes no polarization loss. The results are plotted in Fig. 19 as a function of atmospheric attenuation and zenith angle. The superscripts C and V denote the course and vernier detectors respectively. For the purpose of false alarm rates, an earth reflectivity of unity will be assumed.

C. RETURN SIGNAL PHOTONS

The number of return photons can be expressed in the following form (radar equation)

$$E_s^{C,V} = \frac{E_{P,T}(\text{joules})\lambda(\mu m)}{1.99\times10^{-19}(4\pi R^2)^2} G_t(\theta_t)A_r T_r T_t T_{atten}$$

$$\bullet\ \sigma_R(\theta_R)\left[T_{atm}(0^\circ)\right]^{2/\cos\theta_z},\ \text{photons} \tag{46}$$

where $E_{P,T}$ is the transmitted energy in the largest pulse or total energy in the pulse train, λ is the laser wavelength in μm, R is the slant range to the retroreflector, and $\sigma(\theta_R)$ is the equivalent cross section of the retroreflector.

The equivalent gain of the transmitting optics is given in Eq. 32. The worst case point error is assumed to be equal to

$$\theta_t = \theta_{bore} + \theta_{track} \tag{47}$$

where θ_{bore} is the boresight error and θ_{track} is the optical beacon tracking accuracy. For optimum signal the beam divergence is set equal to $2\theta_t$.

The retroreflector radar cross section is given by Eqs. 38 and 40. The above analysis is patterned after the standard radar approach and assumes Gaussian radiation patterns for the transmitting and retroreflector optics.

Since the satellite has changed position from the time the outgoing pulse was transmitted to the time the return pulse is received (transit times range from about 1 msec to 10 msec), optimum signal is obtained when the beam divergence is set equal to two times

$$\theta_R = \frac{2u}{c}\cos\left[\tan^{-1}\left(\frac{Y_T}{\sqrt{X_T^2 + Z_T^2}}\right)\right] \tag{48}$$

where θ_R is the angular change in the satellite position, u is the satellite velocity, and c is the velocity of light in vacuum. Without active focusing the optimum beam divergence cannot be realized. The calculations were performed with α_R equal to 10^{-4} radians which corresponds to twice the maximum angular position change.

During the entire pulse train the phase across the retroreflector face is assumed to be constant. The maximum change in the optical delay across the retroreflector array from the first to last pulse is less than 1° assuming an orbital altitude and velocity of 1.85×10^7 cm and 7.5×10^5 cm/sec respectively.

The geometrical factors appearing in Eq. 46 can be derived from the geometry shown in Fig. 18. The subscript T denotes the satellite position when the outgoing pulse train is transmitted and the subscript R denotes the satellite position when the return pulse train is received. A minimum and maximum orbital altitude of 1.85×10^7 to 5.56×10^8 cm were assumed. Calculations of the expected number of signal photons incident on the course and vernier detectors are presented in Figs. 20 through 23. The equivalent antenna gain of the transmitting optics is obtained from Eqs. 32 and 47 and the equivalent radar cross section of the retroreflector is calculated using Eqs. 38 and 48. The other system parameters appearing in Eq. 46 are defined in Table 6.

The number of signal photons received by the course detector is plotted in Fig. 20 as a function of atmospheric attenuation and zenith angle.

In this example the spacecraft pass directly overhead of the retroreflector ($X_T = X_R = 0$). The minimum altitude is equal to 1.85×10^7 cm and the maximum altitude is equal to 5.56×10^7 cm. The range in atmospheric attenuation can be found in Refs. 5 and 44. The corresponding number of signal photons received by the vernier detector is a factor of 6.87 greater than the course detector since the vernier system is integrating the entire pulse train.

The same parameters are plotted in Figs. 22 and 23 except that the retroreflector is located cross range by 1.85×10^7 cm for the minimum orbital altitude (1.85×10^7 cm) and by 5.56×10^7 cm for the maximum orbital altitude (5.56×10^7 cm).

D. SAMPLE MISSION PERFORMANCE

The detection probability and false alarm calculations are presented for clear and hazy atmospheric conditions and a flight geometric corresponding to $Z_T = 5.56 \times 10^7$ cm, $u = 7.5 \times 10^5$ cm/sec, and a cross range $X_T = 5.56 \times 10^7$ cm. These worst case flight parameters represent expected return signal conditions. For the purpose of this sample calculation, the course detector threshold was set at $N_T = 3$ photoelectrons and the vernier threshold was set at $N_T = 4$ photoelectrons. The return gate width, t_G, was assumed to be 10^{-3} sec. The attenuator located in the receiving optical path was set by the previous signal strength recorded by the course range peak detector. A threshold of 63 photons was used in these calculations since that produces a reasonable detection probability of 0.99 on the course detectors and 0.999 on the vernier system.

The background levels were obtained from Fig. 19. The expected number of signal photons at the course and vernier detector photocathodes are obtained from Figs. 22 and 23 respectively. The results are tabulated in Table 7 for two atmospheric conditions. The various geometric parameters such as slant range and zenith angle are also tabulated. For the purpose of this example, the measurement rate is equal to one range measurement every 14 sec.

The corresponding detection probabilities and false alarm rates are derived from Figs. 8, 9, 13, 14, and 15.

At the worst background rate of 1.05×10^8 photons/sec, the course detector would have an average false alarm rate of 3×10^{-3} assuming a detection threshold of 3 photoelectrons. The vernier detector has a false alarm probability per readout of about 0.15 if we assume a return gate width of 10 μsec. Since the high background levels are accompanied by large signal levels, an active optical AGC system would improve the vernier false alarm characteristics. An alternate approach is to incorporate an optical delay line in the receiving optics and gate the vernier detector on and off with the course range detectors. The return gate width could be set at about 200 nsec which results as a false alarm probability per readout of less than 0.001.

The simpler AGC attenuator approach will now be addressed. The false alarm rates and detection probability assuming the flight conditions given in Table 7, receiver gate width $T_G = 10^{-3}$ sec and no attenuation in the optical attenuator, $T_{atten} = 1.0$, are tabulated in Table 8. The results

illustrate the need for active signal AGC. For the same physical condition, the resulting detection probabilities and false alarm rates with T_{atten} set by the peak signal received at the last range measurement are given in Table 9. The results are apparent. The false alarm rates are reduced to tolerable levels at the high signal conditions. The false alarm rates shown in Table 9 are reduced to less than 0.001 under average earth reflectivity of 0.3. Since the vernier system is degraded by background counts, the high thresholds improves performance if active return gates are not employed. The actual system has improved false alarm performance by active gating; however the system complexity may outweigh the improved performance.

Table 7. Signal Photons and Background Levels,
$u = 7.5 \times 10^5$ cm/sec, $Z_T = Z_R = 5.56 \times 10^7$ cm

Time (sec)	Y_T (cm)	R (cm)	θ_Z (deg.)	E_S^V/T_{atten} (photons)	E_S^C/T_{atten} (photons)	P_b^V/T_{atten} (photons/sec)	P_b^C/T_{atten} (photons/sec)	$T_{atm}(0°)$
0	-1.05×10^8	1.31×10^8	64.9°	48	7	9.87×10^5	4.94×10^5	0.25
14	-9.45×10^7	1.23×10^8	63.1	88	12	1.21×10^6	6.05×10^5	0.25
28	-8.40×10^7	1.15×10^8	61.1	162	23	1.47×10^6	7.35×10^5	0.25
42	-7.35×10^7	1.08×10^8	58.9	284	41	1.77×10^6	8.85×10^5	0.25
56	-6.30×10^7	1.01×10^8	56.5	486	70	2.11×10^6	1.06×10^6	0.25
70	-5.25×10^7	9.45×10^8	54.0	792	115	2.46×10^6	1.23×10^6	0.25
140	0.00	7.86×10^7	51.4	2690	392	3.68×10^6	1.84×10^6	0.25
0				1.17×10^4	1.70×10^3	4.91×10^7	2.46×10^7	0.8
14				1.52×10^4	2.21×10^3	5.08×10^7	2.54×10^7	0.8
28				2.00×10^4	2.91×10^3	5.24×10^7	2.62×10^7	0.8
42				2.56×10^4	3.73×10^3	5.40×10^7	2.70×10^7	0.8
56				3.28×10^4	4.77×10^3	5.56×10^7	2.78×10^7	0.8
70				4.13×10^4	6.02×10^3	5.69×10^7	2.85×10^7	0.8
140				7.23×10^4	1.05×10^4	6.07×10^7	3.04×10^7	0.8

Table 8. Detection Probability and False Alarm Rates without AGC, Flight Parmeters Given in Table 7

Time (sec)	T_{atten}	Vernier Detector		Coarse Detector		$T_{atm}(0°)$
		$P_D(N_T = 4)$	$\overline{FAR}$ $(t_G = 10^{-3})$	$P_D(N_T = 3)$	$\overline{FAR}(N_T = 3)$	
0	1.0	0.1	0.008	< 0.1	$< 10^{-5}$	0.25
14	1.0	0.5	0.017	< 0.1	$< 10^{-5}$	0.25
28	1.0	0.92	0.042	0.42	$< 10^{-5}$	0.25
42	1.0	0.997	0.085	0.87	$< 10^{-5}$	0.25
56	1.0	> 0.999	0.17	0.996	$< 10^{-5}$	0.25
70	1.0	> 0.999	0.35	> 0.999	$< 10^{-5}$	0.25
140	1.0	> 0.999	~ 1.0	> 0.999	$< 10^{-5}$	0.25
0	1.0	> 0.999	~ 1.0	> 0.999	3×10^{-5}	0.8
14	1.0	> 0.999	~ 1.0	> 0.999	3×10^{-5}	0.8
28	1.0	> 0.999	~ 1.0	> 0.999	3.3×10^{-5}	0.8
42	1.0	> 0.999	~ 1.0	> 0.999	3.5×10^{-5}	0.8
56	1.0	> 0.999	~ 1.0	> 0.999	4×10^{-5}	0.8
70	1.0	> 0.999	~ 1.0	> 0.999	4.4×10^{-5}	0.8
140	1.0	> 0.999	~ 1.0	> 0.999	4.8×10^{-5}	0.8

Table 9. Detection Probability and False Alarm Rate with AGC, Same Conditions as Table 7

Time (Sec)	T_{atten}	E_S^V (photons)	$T_{atm}(0°)$	P_b^V (photons/sec)	Vernier $P_D(N_T = 4)$	Vernier $\overline{FAR}(t_G = 10^{-3})$
0	1.0	48	0.25	9.87×10^5	0.1	0.008
14	1.0	88	0.25	1.21×10^6	0.5	0.017
28	1.0	162	0.25	1.47×10^6	0.92	0.042
42	1.0	284	0.25	1.77×10^6	0.997	0.085
56	1.0	486	0.25	2.11×10^6	> 0.999	0.17
70	0.89	705	0.25	2.19×10^6	> 0.999	0.24
140	0.17	457	0.25	6.26×10^5	> 0.999	0.0012
0	1.0	1.17×10^4	0.8	4.91×10^7	> 0.999	~1
14	0.037	562	0.8	1.88×10^6	> 0.999	0.1
28	0.028	560	0.8	1.47×10^6	> 0.999	0.045
42	0.022	563	0.8	1.19×10^6	> 0.999	0.017
56	0.017	558	0.8	9.5×10^5	> 0.999	0.0065
70	0.013	537	0.8	7.4×10^5	> 0.999	0.0025
140	0.0062	448	0.8	3.76×10^5	> 0.999	< 0.001

X. REPRESENTATIVE SYSTEM

A. OPTICAL LAYOUT

A representative optical layout is shown in Fig. 6. In the actual construction and detailed optical design, care must be taken that high quality optical components are used so that near diffraction limited performance is obtained. For example, the primary receiving mirror should be of the highest quality (e.g., $\lambda/20$) since the bore sight alignment of the transmitter and return channels is important in this application. Assuming that the outgoing beam is gaussian with a $(1/e^2)$ radius of 1.2 cm and a 64 cm focal length primary mirror, the outgoing and optical beacon channels can be aligned to better than 3.75×10^{-5} radians if diffraction limited optics are used.

The background rejection filters are staged to reduce flourescence problems. The actual bandwidth requirements are governed by doppler shifts and transmitted pulse spectrum. Assuming a rectangular 25 psec laser pulse, a maximum directed spacecraft velocity toward the retroreflector of 7.5×10^5 cm/sec and a laser wavelength of 0.6943 μm, yields a 1Å bandwidth requirement. A more conservative 3Å was used in the system calculations. Care must be taken in the selection of the narrow band filter to insure that the desired filter stability and polarization characteristics are realized. (Ref. 42)

If detection thresholds of 2-4 photoelectrons are used, careful optical layout and design is needed to minimize the amount of scattered and reflected light reaching the detectors. Special attention must be given to minimizing stray electrical signals.

B. GUIDELINES TO WEIGHTS, VOLUME, AND POWER

The rough estimates of the various system component weights, volumes and power requirements are listed in Table 9. The sum total volume will never be realized because of packing. The optics, laser, and receiver volume is about 1.0×10^5 cm^3. The total electronics volume is 7.7×10^4 cm^3 assuming unity packing factor. Assuming a 150% packing factor results in volume needed for the electronics of 1.20×10^5 cm^3 and a total volume of 2.2×10^5 cm^3 (0.22 m^3). With careful mechanical and electronic design, the size, weight, and volume restriction should be able to be satisfied.

Table 10. Estimated Component Weight, Volume and Power

	Wt. (lbs.)	Vol. (cm^3)	Power(W)
Laser head	10	9,000	-
Laser amplifier	10	1,500	-
Polarization mod.	15	1,000	10
Capacitor bank	150	45,000	900 *
Freq. standard	15	10,000	30
Time interval meter	15	10,000	30
Vernier det.	10	3,000	15
Course det.	15	4,000	15
Background rec.	5	1,000	7
Vernier driver	5	400	10
Master timer	10	5,000	10
CCD electronics	2	1,000	5
Optical tracker	20	8,000	30
Computer	4	2,000	10
Optics	10	10,000	-
Display panel	5	3,000	
Supporting structure	100	10,000	
	401 lbs.	1.23×10^5	1,070 W

*Based on 80% efficiency in charging capacitors and measurement rate 4.29 PPM.

The actual system geometrical configuration may differ from the characteristics given in Table 10; however a factor of 2 reduction in weight or size is improbable since the weight and size are governed by the capacitor bank, charging rate, and efficiency of the laser. The numbers used in this respect are at this point in time state-of-the-art.

The simultaneous ranging to 4 independent reflectors on the earth's surface requires one transmitter section, four independent tracking optical systems and a course and vernier receiving system capable of identifying the returns. The expected total weight would be 632 lbs., the expected power requirements 1385 Watts, and the total system needs about 0.5 m^3 volume.

XI. FLIGHT TEST EXPERIMENTS

A. MISSION PROFILE

The sequence of events leading to a set of range measurements are outlined in this section. The spacecraft is first manually oriented to provide maximum viewing time. The steering mirror is positioned to allow acquisition of the beacon laser. The ground reflector system is activated about 30 sec prior to the ranging measurements and the S-Band beacon tracking system locks onto the ATL beacon. After the laser beacon tracking system has acquired the retroreflector beacon, the system is ready to perform the desired measurements. During each range measurement, line of sight angle, exact transmit time, background, and meteorological data are recorded along with the range data.

Man's role is to maintain equipment, to calibrate, to check electrical performance, to check optical performance, to record data, to provide coordination with other experiments, to shut down equipment, and to secure for reentry. Specialized functions such as optical alignment, focusing, and boresight adjustments which cannot be maintained with enough precision during launch, will have to be performed in orbit. During the measurement phase flash lamp replacement, laser cavity adjustment, and range calibration may be needed. The laser cavity will need periodic adjustments so as to maintain the desired frequency stability between the modelocked train and vernier detector sweep frequency. This function is performed by minimizing the reference pulse width recorded by the vernier system as the cavity is mechanically adjusted. Prior to actual ATL to ground measurements the

system should be calibrated and checked out optically to insure maximum sensitivity and timing resolution.

B. OPTICAL ALIGNMENT

The system is a precision optical instrument with near diffraction limited performance. As a result, optical bore sight alignment of the optical tracker, rangefinder receivers, and transit beam must be performed in orbit since the optical performance probably cannot be maintained during launch. The optical tracking system should be designed to aid in the bore sight alignment. Specially designed optical filter should be incorporated in the laser beacon tracking system to allow some transmission at 0.6943 μm.

During the alignment procedure, the 0.6943 μm transmit beam would be attenuated. A small retroreflector is placed in the outgoing beam as shown in Fig. 6. The steering mirror m_1 would be adjusted so that the image was centered on the optical tracker. After the tracker and rangefinders are bore sighted, the course and vernier receivers may need re-alignment. The center elements of the vernier target array are used for this purpose. Finally, the adjustable field stop is centered and adjusted to the desired field of view needed for the particular experiment. The output attenuator and calibration retroreflector are removed and the system is ready for use. The beam expander can then be defocused as the mission requires.

C. RANGE FINDER PERFORMANCE MEASUREMENTS

The objectives of these range measurements are to obtain the necessary data needed to assess the performance and accuracy of the rangefinder system under various atmospheric and background illumination conditions. To this end, a special block retroreflector design could be used to measure

the differential range resolution and vernier detection sensitivity. The basic configuration is shown in Fig. 24.

The actual return recorded by the vernier system consists of many individual pulses having different amplitudes and range separations. The split level array should be designed with 25, 50, and 100 picosecond pulse separations and return amplitudes corresponding to 10, 30, 100, 300, and 1000 cm^2 intercept areas. The above composite return spans 875 picoseconds, thereby satisfying the requirement that the return be less than one vernier sweep period. The results of a single measurement set yields information about the detector sensitivity and differential range resolution and are insensitive to atmospheric effects.

The range resolution can also be inferred by simultaneously ranging to four accurately positioned retroreflectors. The six inter-reflector distance should be measured with a two color laser ranging system if possible and the individual reflectors should be located within the transmit beam. In this application the receiver field of view and transmit beam divergence would have to be increased to allow simultaneous illumination. The present system has enough signal margin to allow a 3 to 10 mile spot size on the ground when operating at night in a clear atmosphere. The system accuracy can be inferred by using three of the satellite-to-ground distances to fix the position of the satellite and the fourth measurement to obtain the closure error. In the case of the rangefinder system shown in Fig. 1, the above concept is more difficult to implement since the vernier receiver is not equipped to identify which output pulse belongs with which reflector. Return signature encoding could be implemented, however the schemes become complicated with increasing number of pulses to be unambiguously identified.

If the relative position of the satellite is known to within a few meters by means of ground based laser ranging, the range accuracy can be inferred by assigning each return to a specific reflector and then examining the closure errors of each of the 24 possible solutions. This technique is questionable without an extensive error analysis for the particular geometric configuration and expected measurements accuracies.

The absolute range accuracies and systematic errors are best measured directly in ground or field testing over well instrumented 5 to 10 km paths. The satellite to ground absolute accuracy can also be determined by accurately fixing the satellite with ground laser ranging and an accurately positioned retroreflector.

During all range measurements, background levels and meteorological data should be monitored and recorded.

In all of the absolute range measurement missions, the slant range, and line of sight angles should be used to transform the actual range measurements to the ATL center of gravity.

The range results should then be checked against other system altimeter and satellite ephemeris data.

D. GEODETIC MEASUREMENTS

The distance between two surface points can in principle be determined assuming a local Keplerian orbit, and measuring at least six sequential range measurements per site and the exact transmission time.

Assuming a total measurement time of 200 seconds, (measurement rate = 4 min^{-1}, base line = 50 - 100 miles, and satellite velocity = 7.5×10^5 cm/sec) the frequency standard should have an accuracy of

$\Delta f/f = 6.7 \times 10^{-9}$ if the satellite position error is to be less than 1 cm. Nine measurements per site should provide better local orbital reconstruction since position, velocity and acceleration terms can be obtained. Depending on the time required to complete the set of measurements and the ground distance involved, microscopic orbital pertibations will ultimately limit the accuracy of the surface distance reconstruction. A more accurate technique for surface distance reconstruction is simultaneous ranging from the satellite to four ground retroreflector sites. Six sets of four simultaneous measurements are needed to solve for the six unknown surface distances. In this case, the orbital form is not needed for the inversion. However, for large base line measurements, the transmit beam does not simultaneously illuminate the four retro sites. Under these circumstances, four independent tracking optics and receiver systems are needed. Retroreflector return signature techniques can be used if stepped retroreflectors and vernier receiver return pulse decoding are employed.

E. ADVANCED GLOBAL GEODETIC SYSTEM

In view of the microscopic orbit perturbations and satellite limitations on system power weight and volume, the most sensible global geodetic laser ranging system would consist of a single color sequential satellite mode-locked laser rangefinder and four simultaneous ground based two color laser rangefinder systems. The ground based systems would be used to update satellite ephemeris data and accurately fix its position in space and time. Two color ranging is used so that the necessary range precision could be maintained at large zenith angle look angles needed for inter-continental base line configurations. Only three ranging systems are needed to fix the satellite

position if the location of each site is accurately known. The four ground based systems are therefore initially used to obtain the exact location of the sites by simultaneously ranging from the ground to the satellite. After the initial phase, only three sites are needed. In order to reduce the site to site timing synchronization, the satellite system should be equipped with instrumentation to measure the differential time of arrival of the four ground based laser ranging pulses.

The satellite-based single color ranging system could then be used in determining the position of secondary retroreflector sites by making three sequential range measurements along with the ground based fix information.

Since the position determination of the secondary reflector sites can be made near the zenith, the atmospheric range correction uncertainties can be kept to a minimum, thereby requiring only a single color rangefinder.

XII. CONCLUSIONS

With state-of-the-art vernier detector technology, it is theoretically possible to design a pulsed laser rangefinder system having a range resolution of $\pm$ 0.8 mm. The basic receiver consists of an image tube having two-axis deflection, ultra-stable VHF electron beam deflection driver, CCD target, associated readout electronics, and course range counter. With the CCD target, it is expected that the detection of two to four photo-electrons per cell is possible. With this sensitivity and timing accuracy, the receiver has potential in a two-color ranging application.

The single color system analyzed in this study has the potential range resolution of $\pm$ 0.4 cm neglecting retroreflector and atmospheric effects. For worst case conditions accuracies of $\pm$ 2.0 cm should be possible. The Cerro Gordo results presented in Sec. II support this contention. The system performance analysis clearly demonstrates that detection probabilities of greater than 0.99 can be expected at ranges less than 1000 km, zenith angles less than 55° and under hazy atmospheric conditions. The above performance easily satisfies the mission requirement to range from the ATL spacecraft to the ground. For the minimum orbital altitude the laser amplifier could be deleted without degrading performance.

The weight, size, and power requirements are technical estimates only; however, they do represent conservative numbers in most cases since the values were derived from available laboratory equipment which has not been designed for minimum weight, size or power requirements. The laser

transmitter is available; however most systems are not space qualified. The vernier detector is a development item and hardware development should be pursued in the near future.

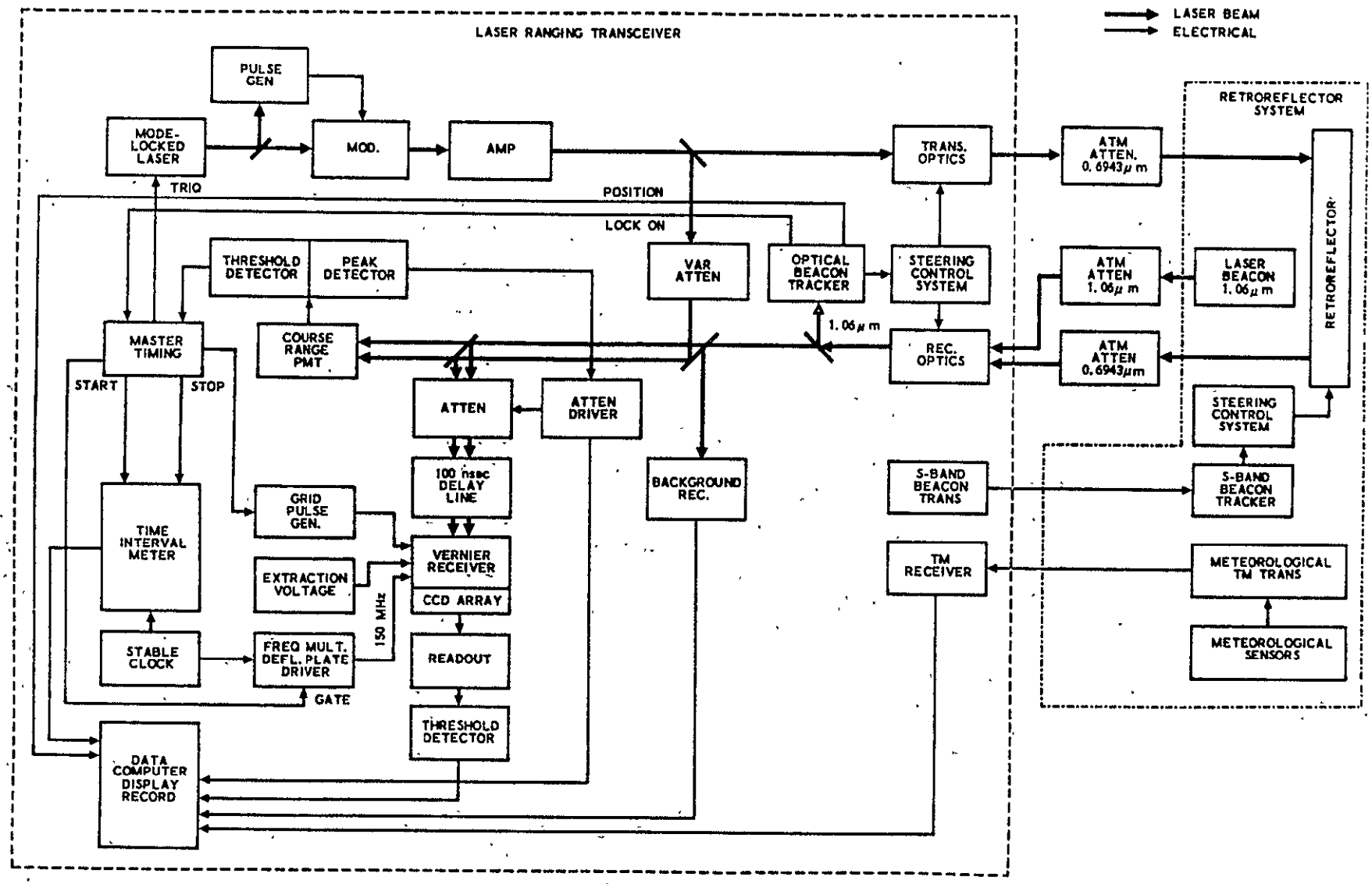

Fig. 1. Basic Precision Range Finder System

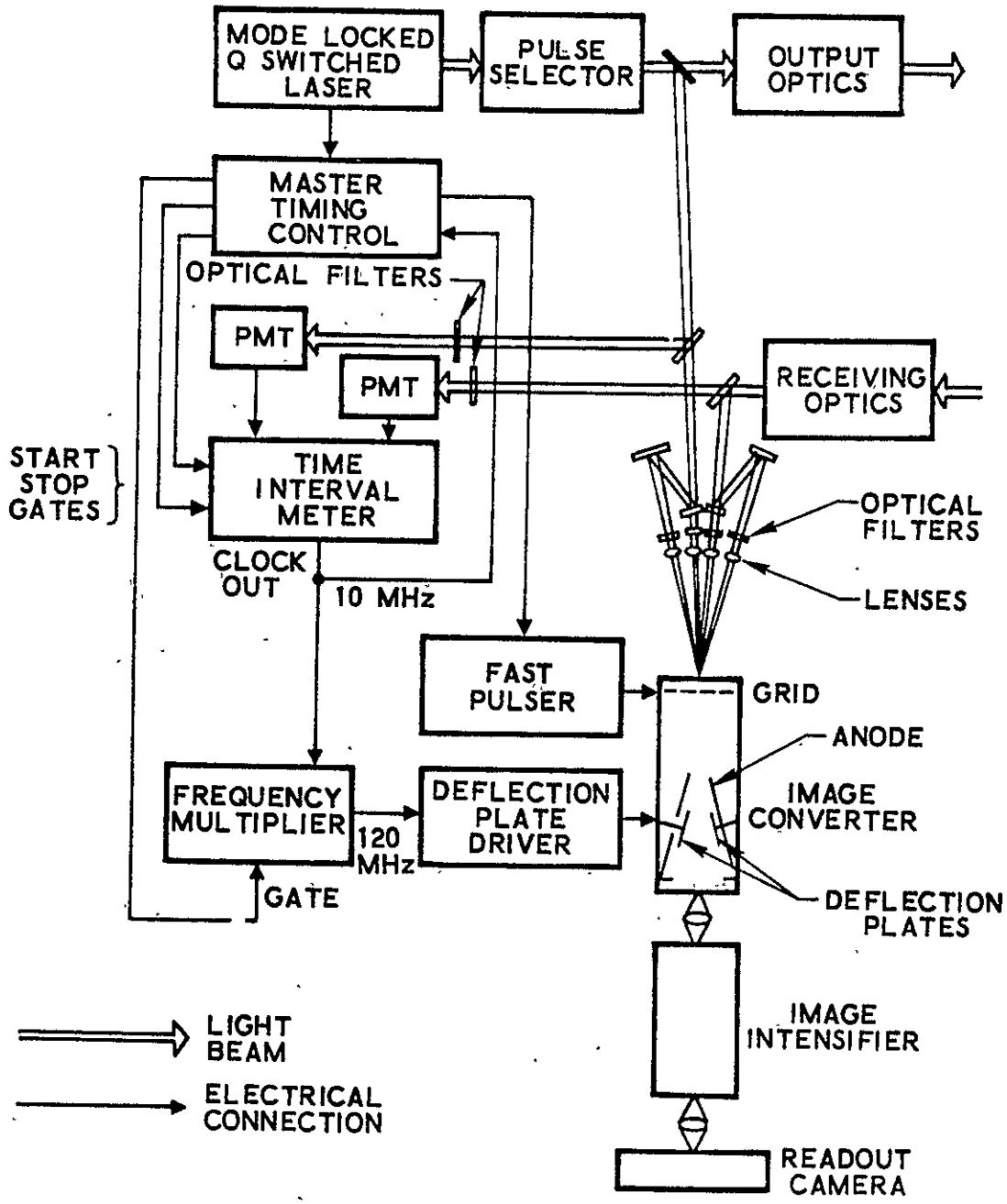

Fig. 2. Prototype Rangefinder

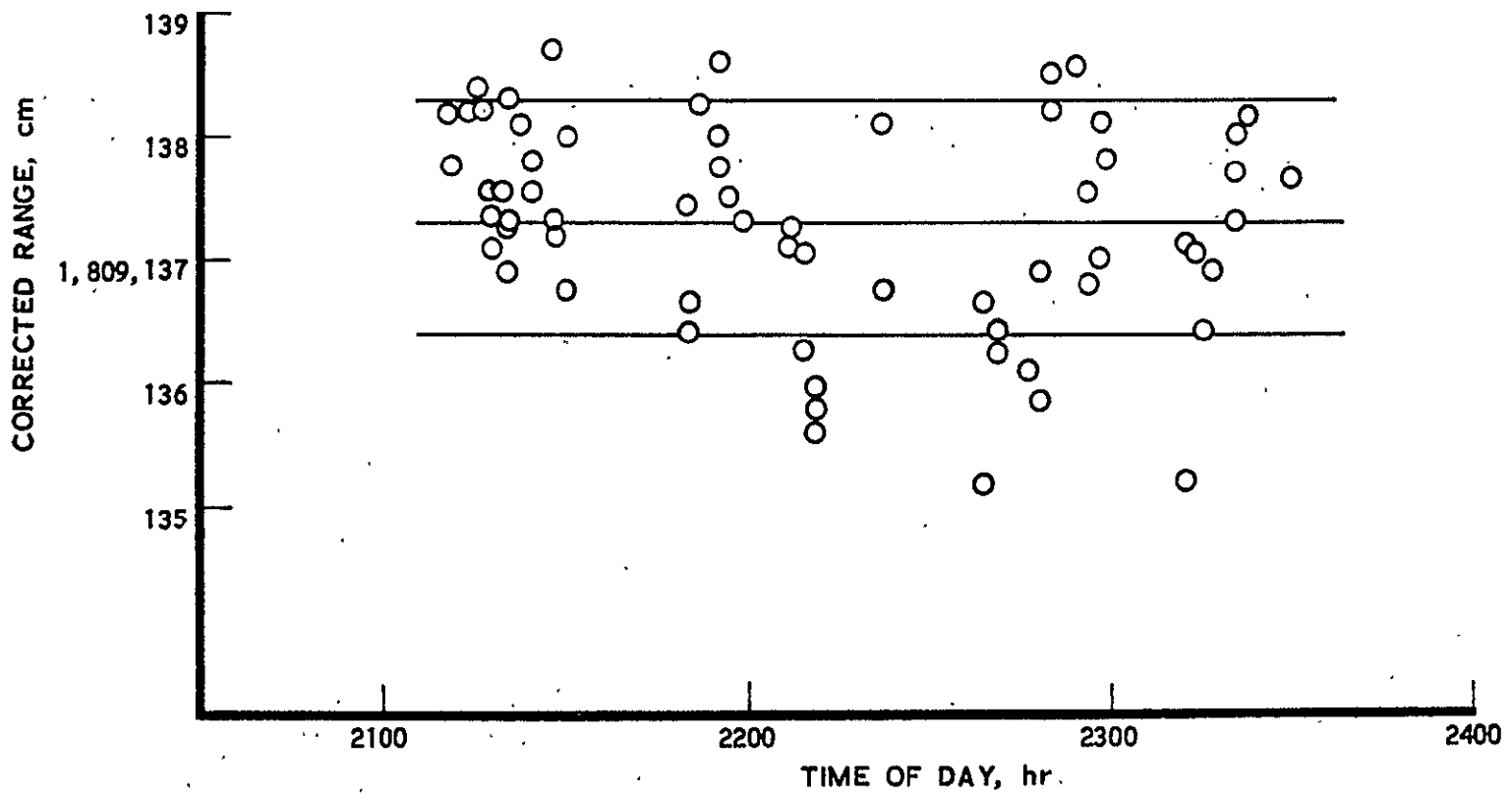

Fig. 3. Cerro Gordo Range Data, R ≅ 18 km; 10/4/73

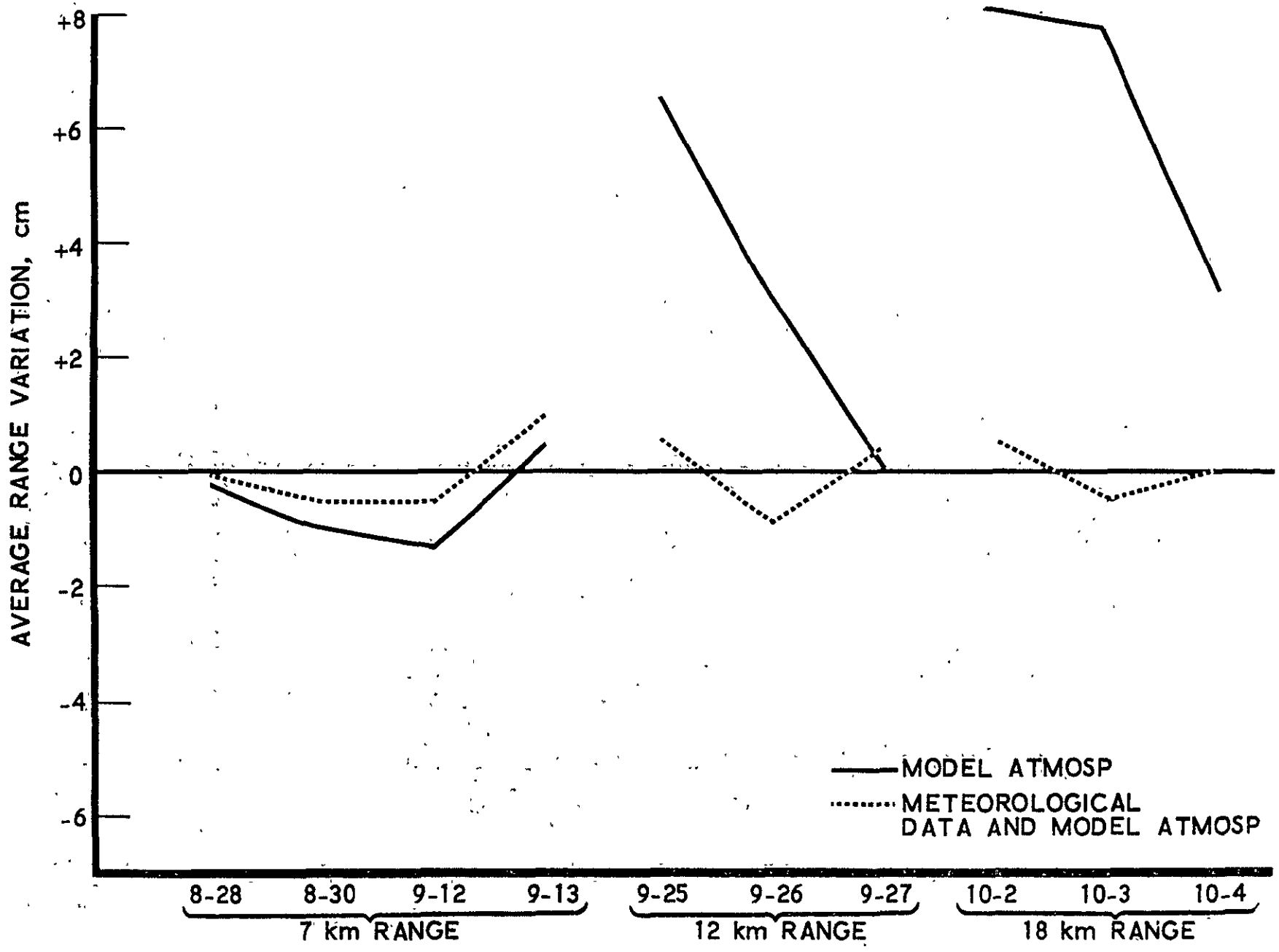

Fig. 4. Variations in Daily Average Range Data, Cerro Gordo

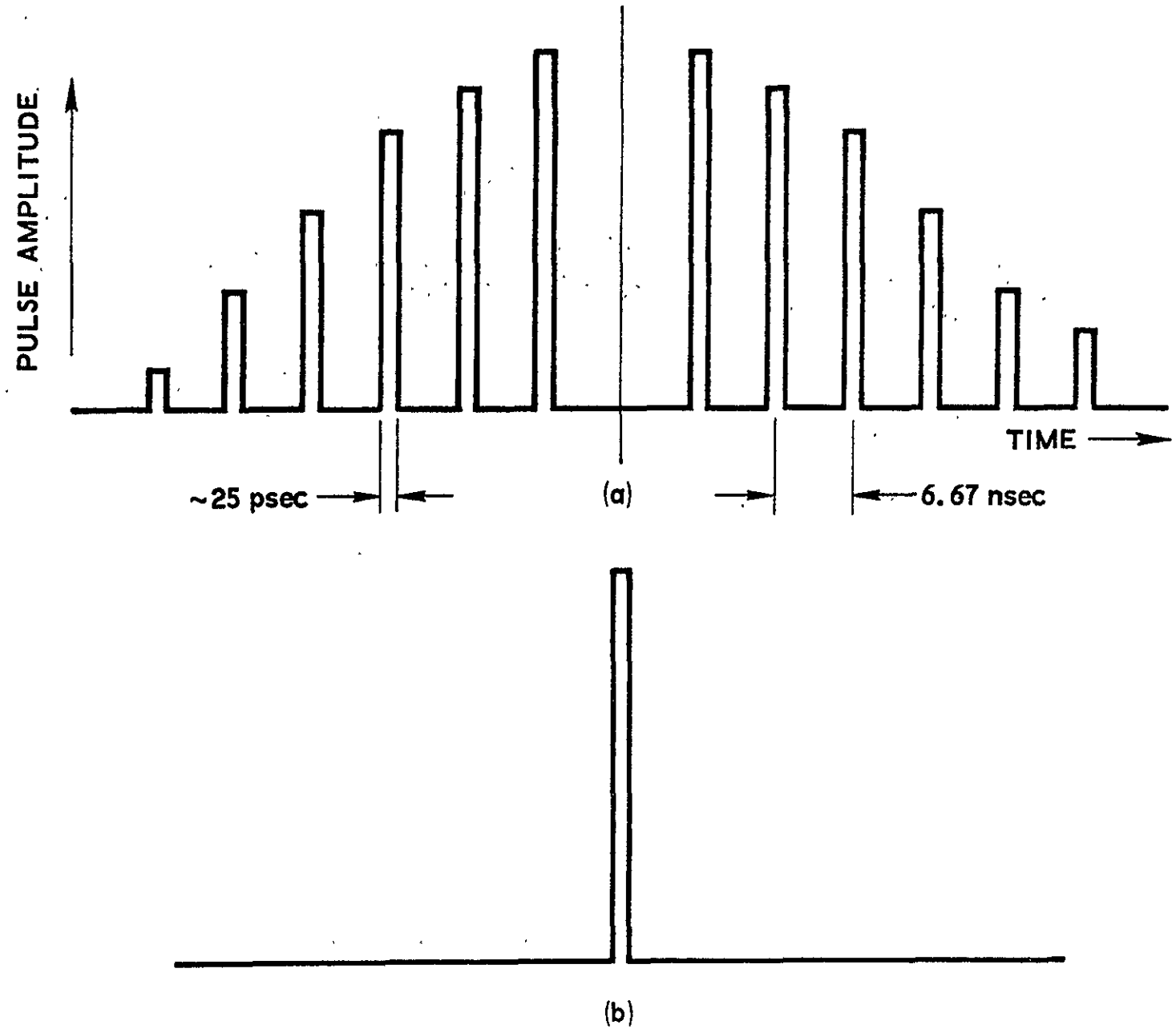

Fig. 5. Optical Pulse Train (a) 0° Polarization
(b) 90° Polarization

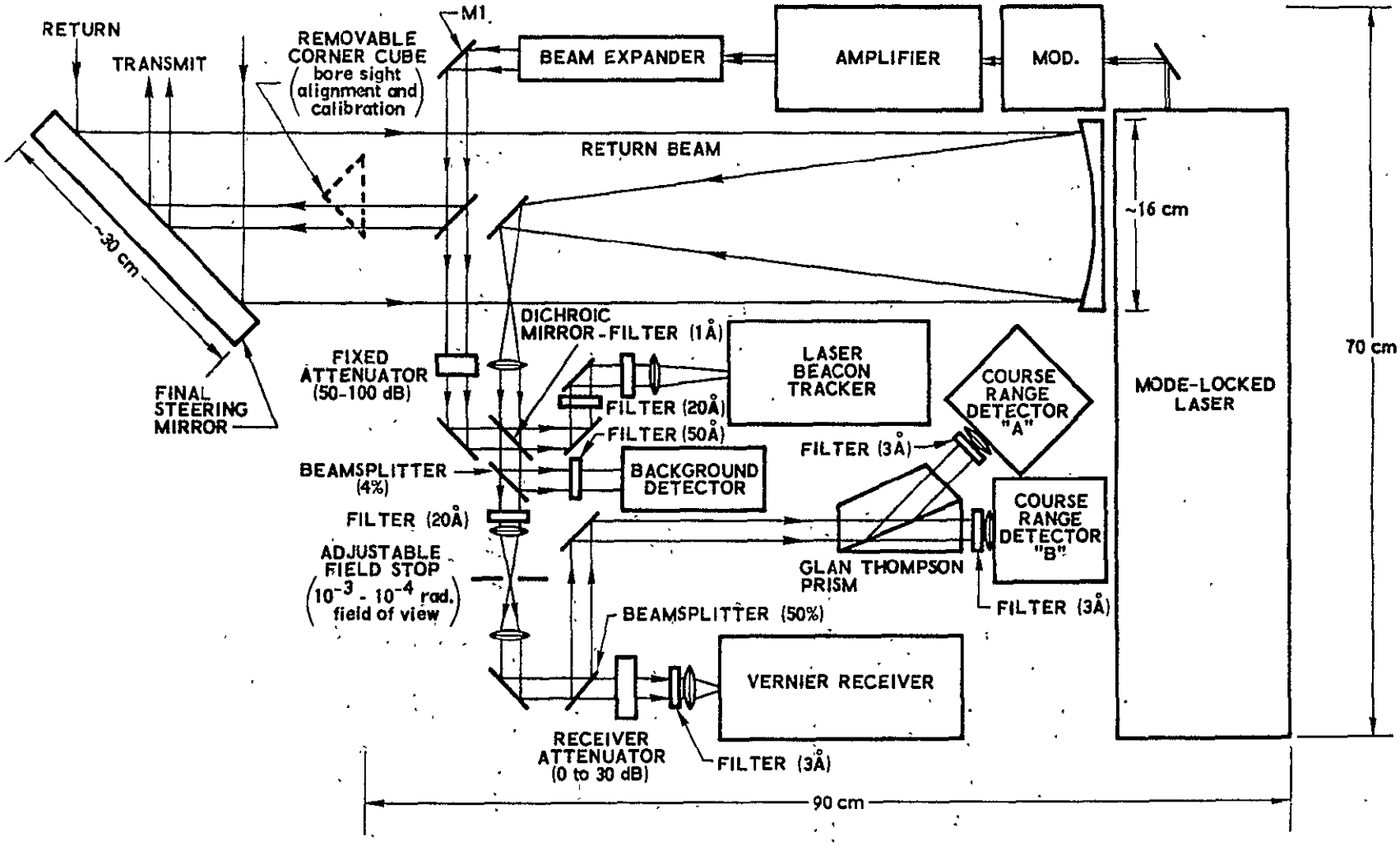

Fig. 6. Representative Optical Layout

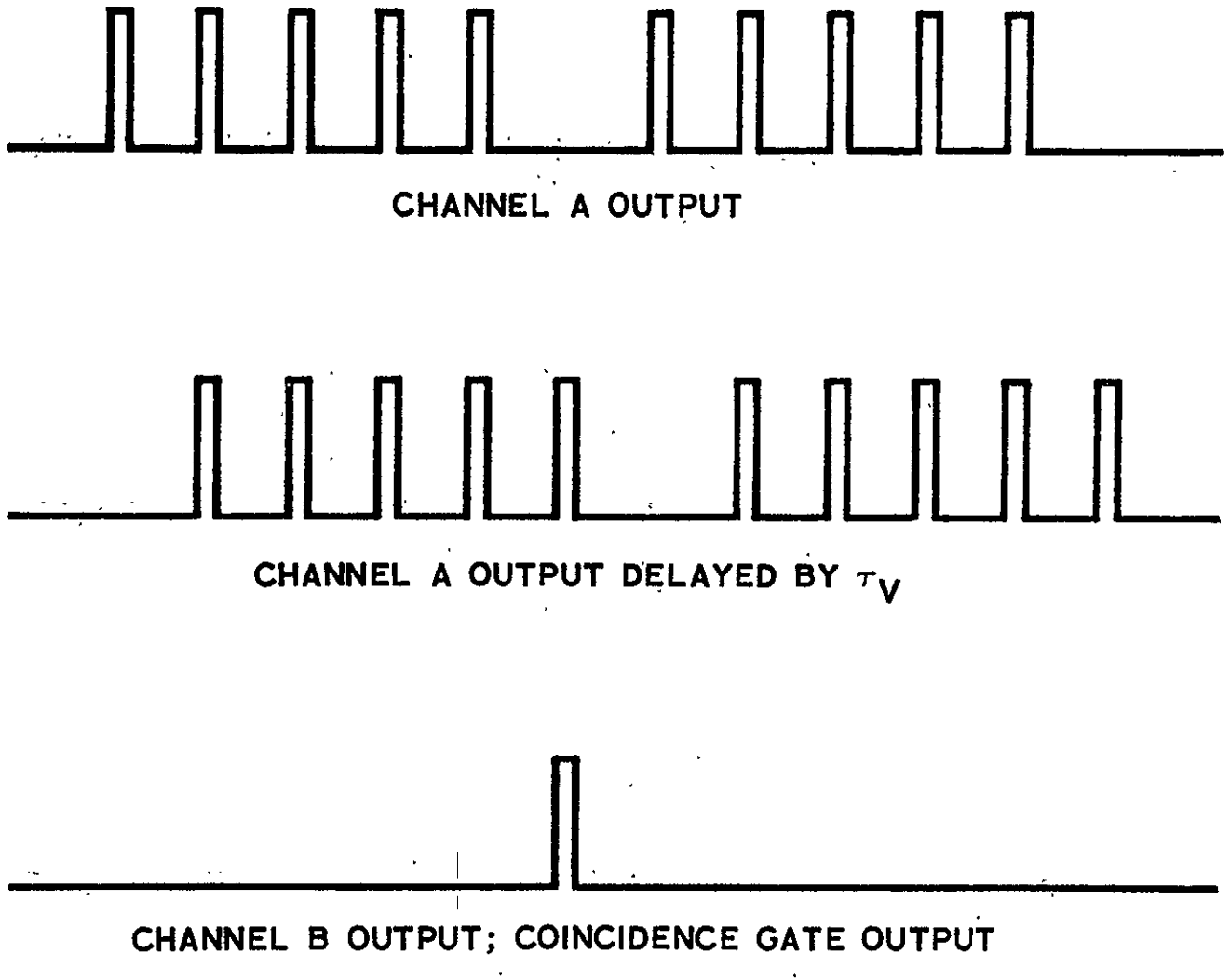

Fig. 7. Detection of Polarization Coded Pulses

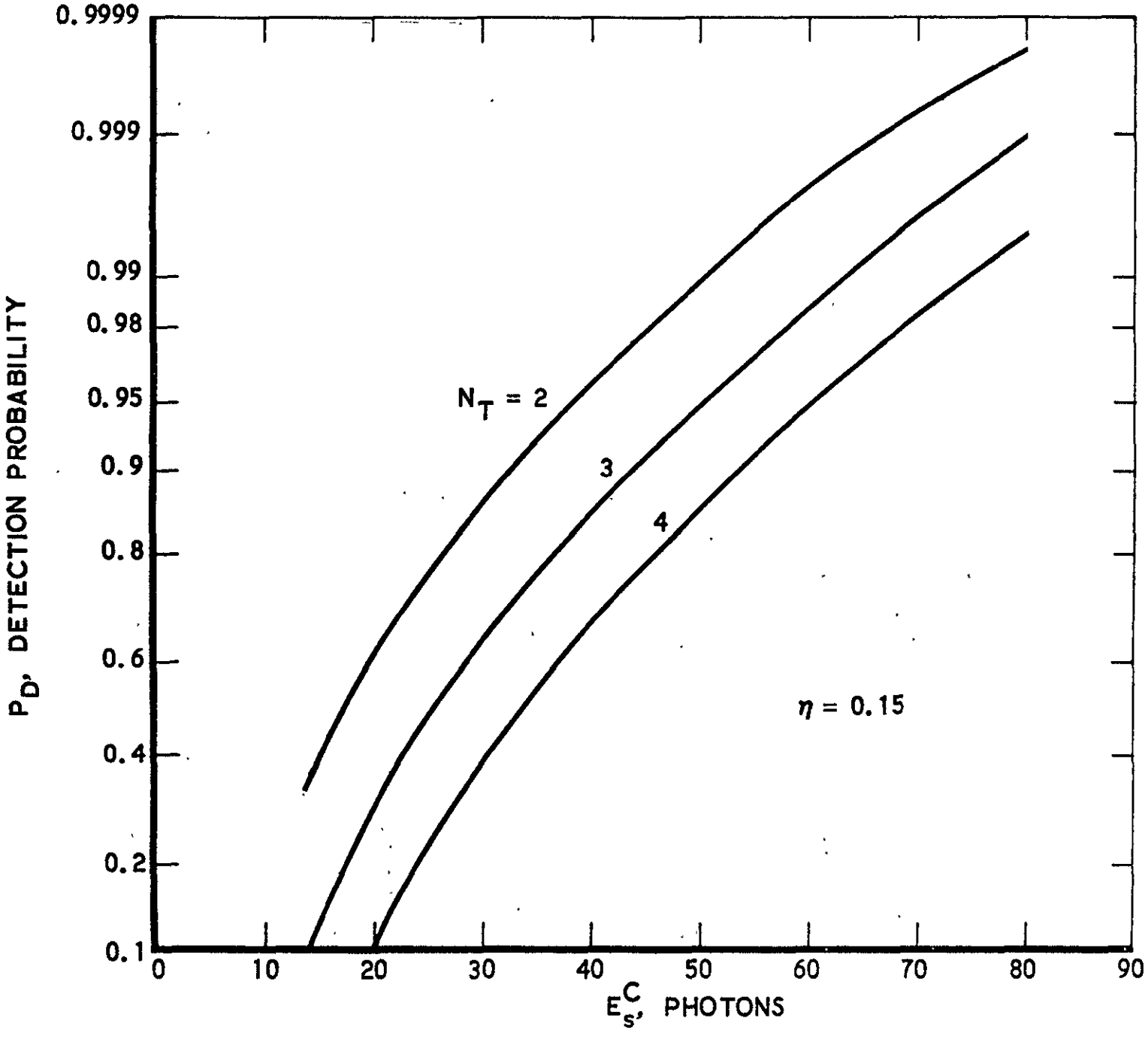

Fig. 8. Detection Probability for Coarse Detector

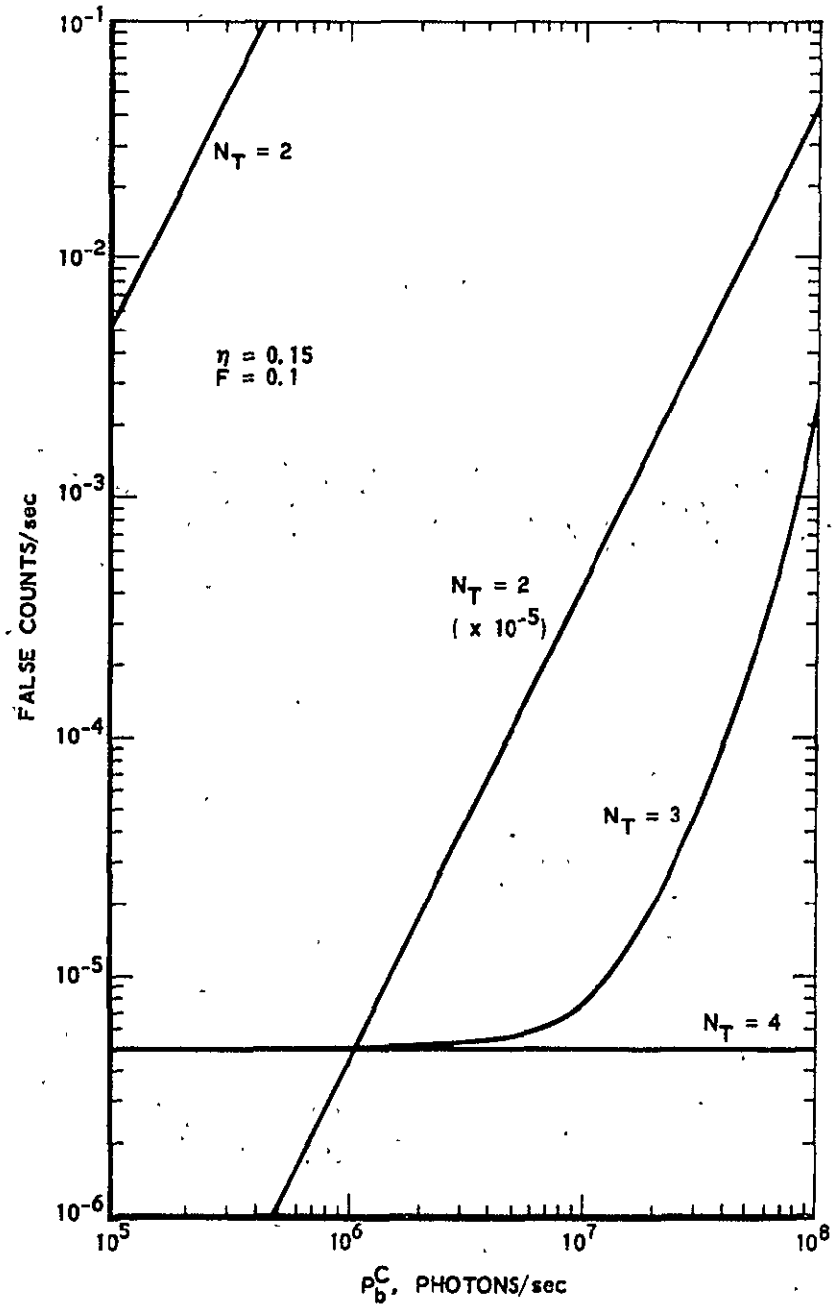

Fig. 9. False Count Rate for Coarse Detector

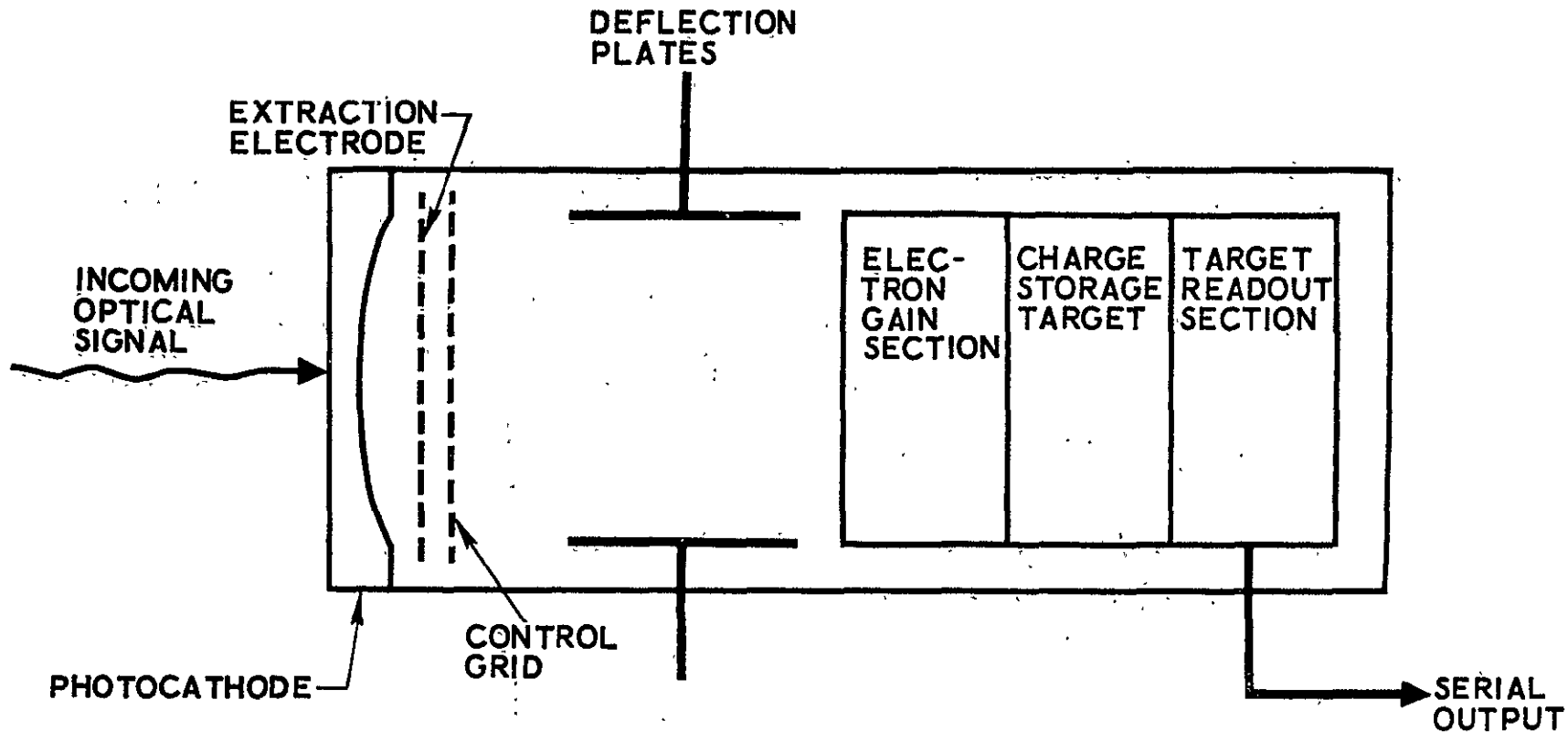

Fig. 10. Schematic Representation of Vernier Detector

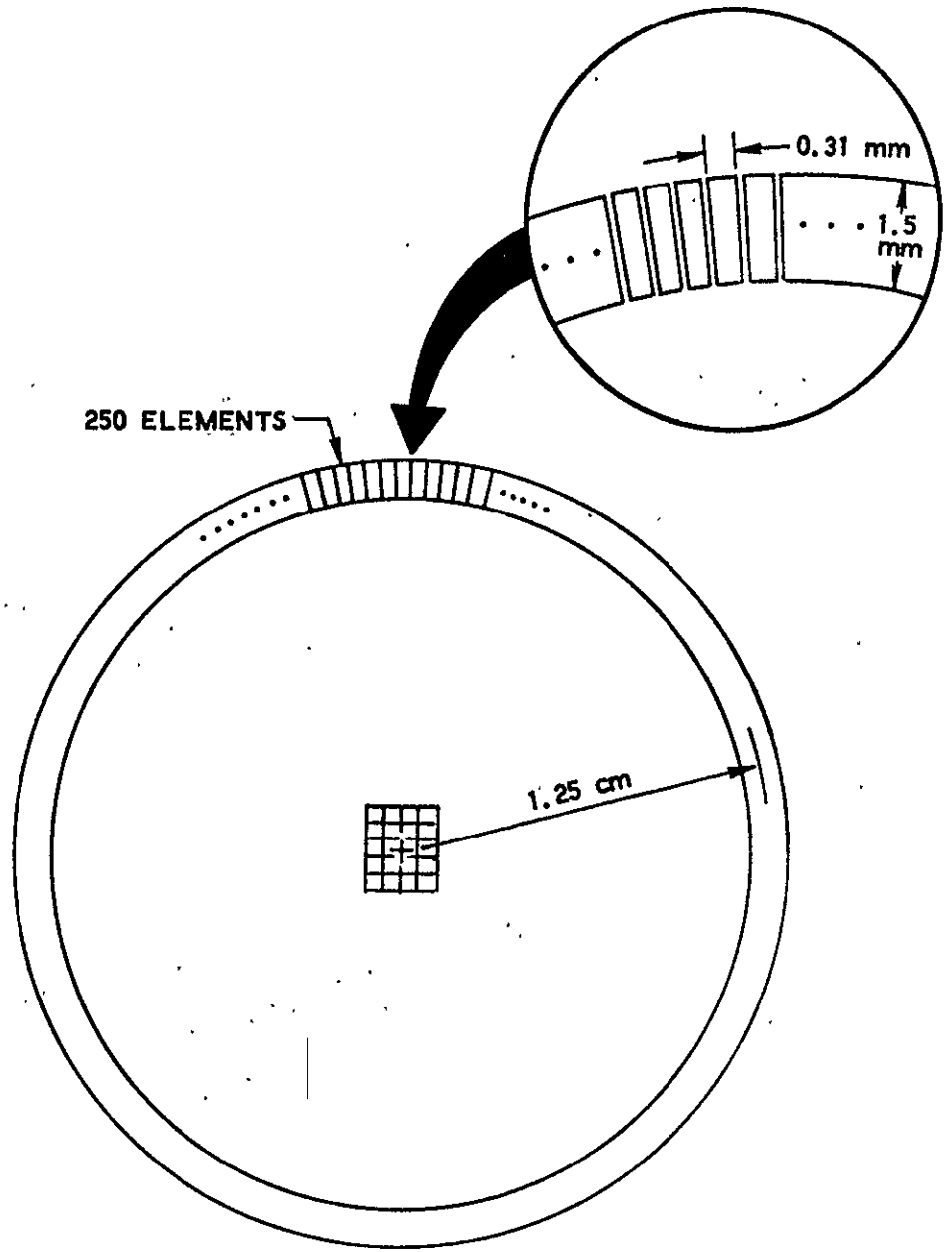

Fig. 11. Illustration of Vernier Target Structure

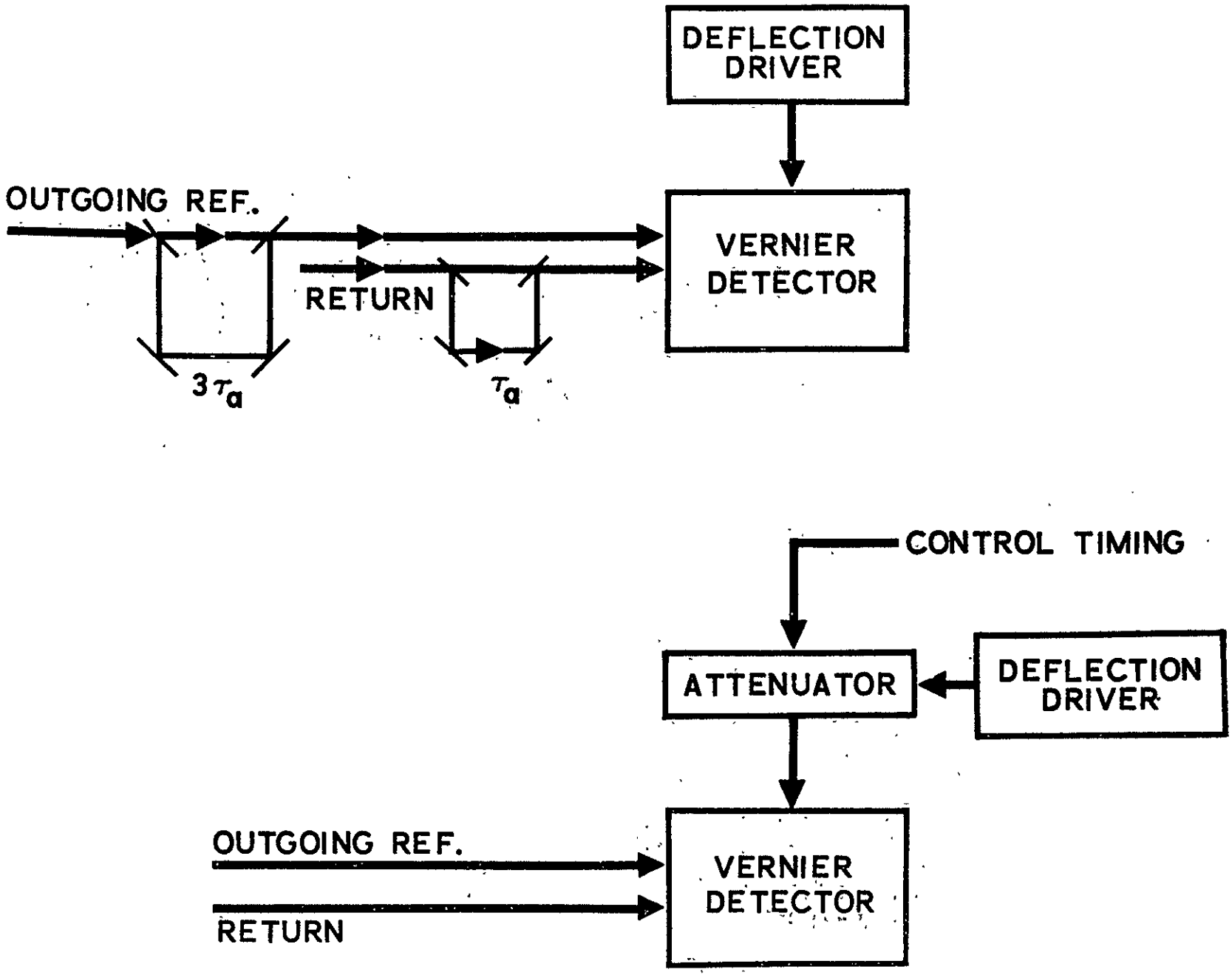

Fig. 12. Techniques for Discriminating Outgoing and Return Pulses

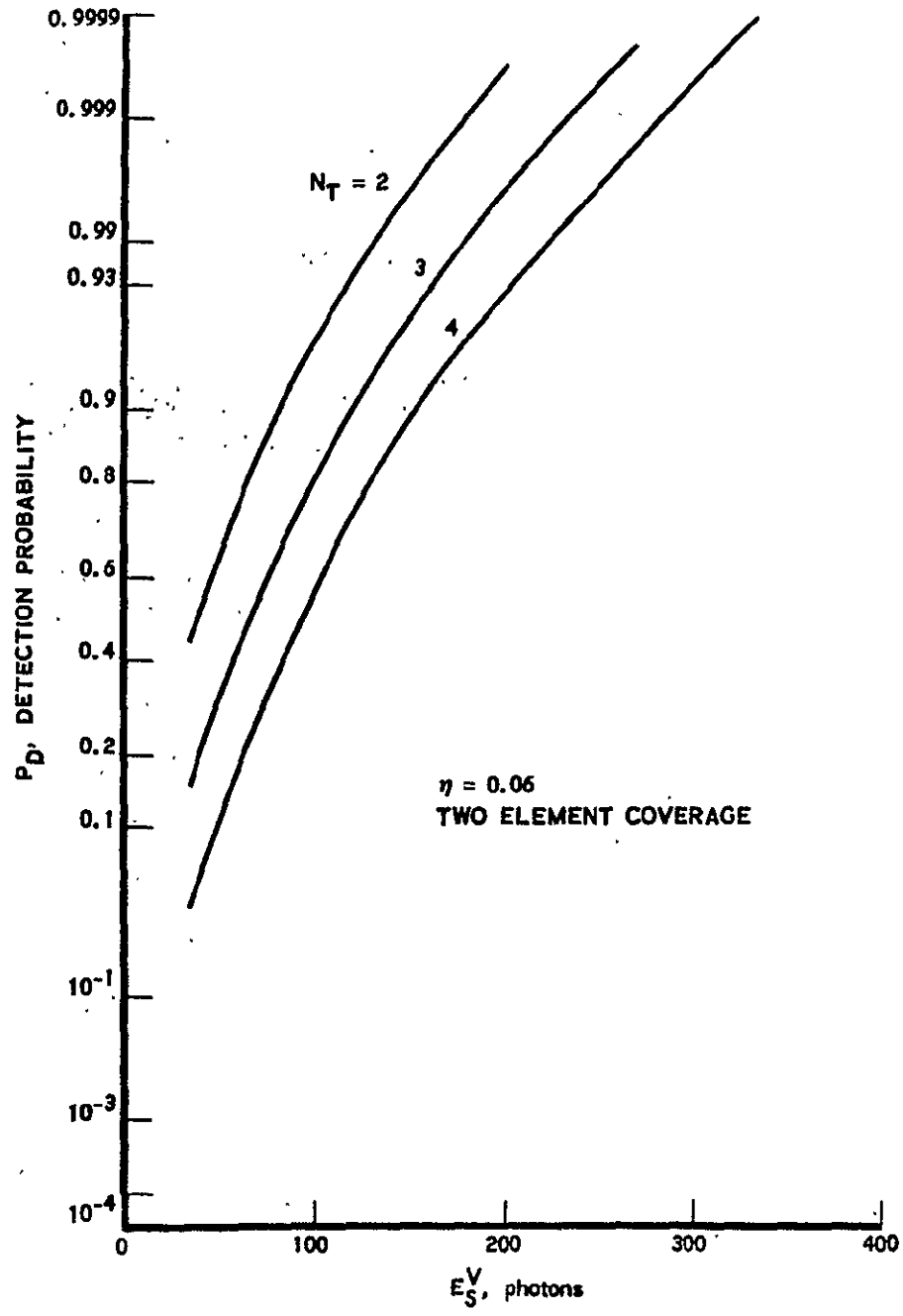

Fig. 13. Detection Probability of Vernier Detector

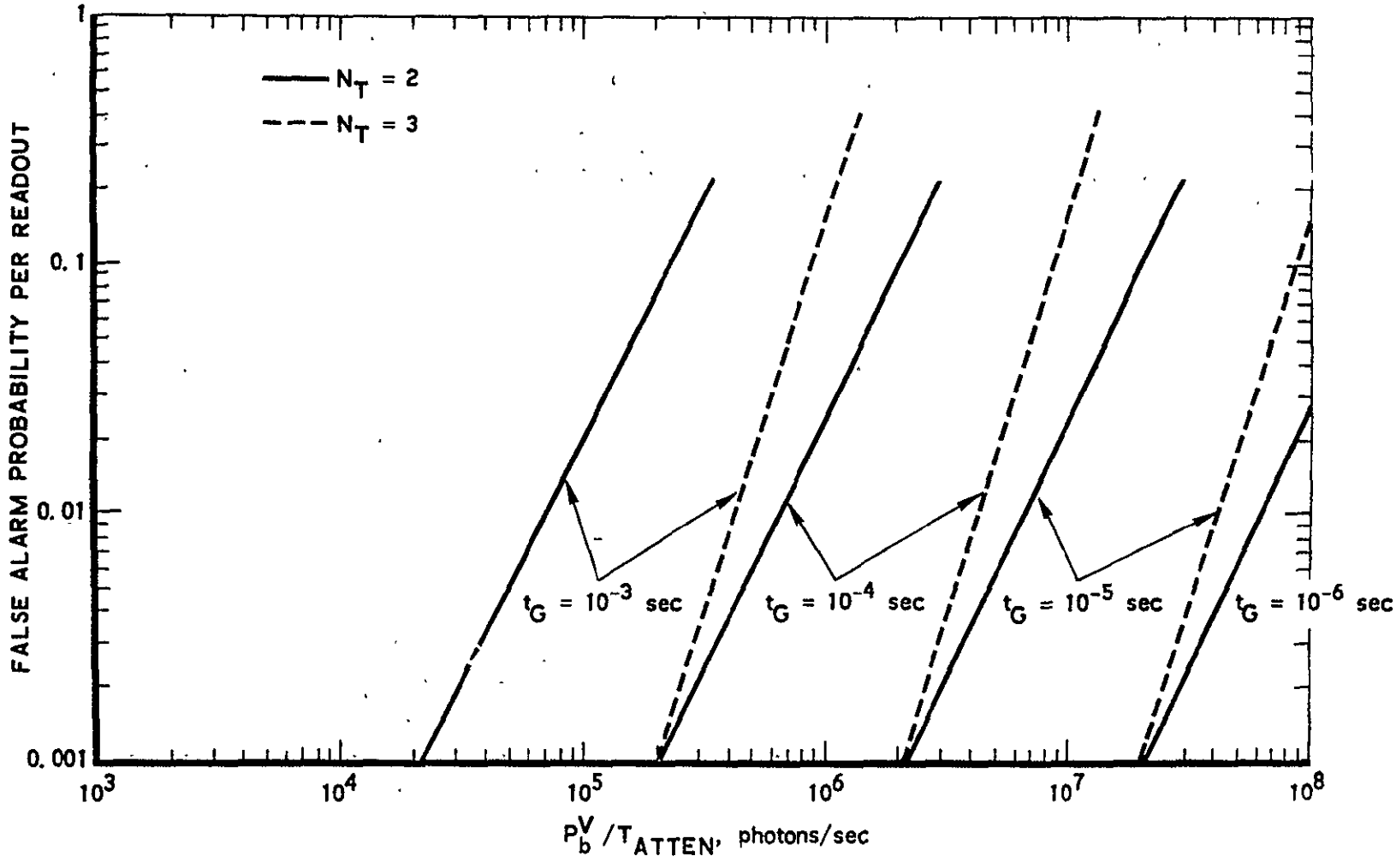

Fig. 14. False Alarm Probability per Readout for Vernier Detector, $N_T = 2$ & 3

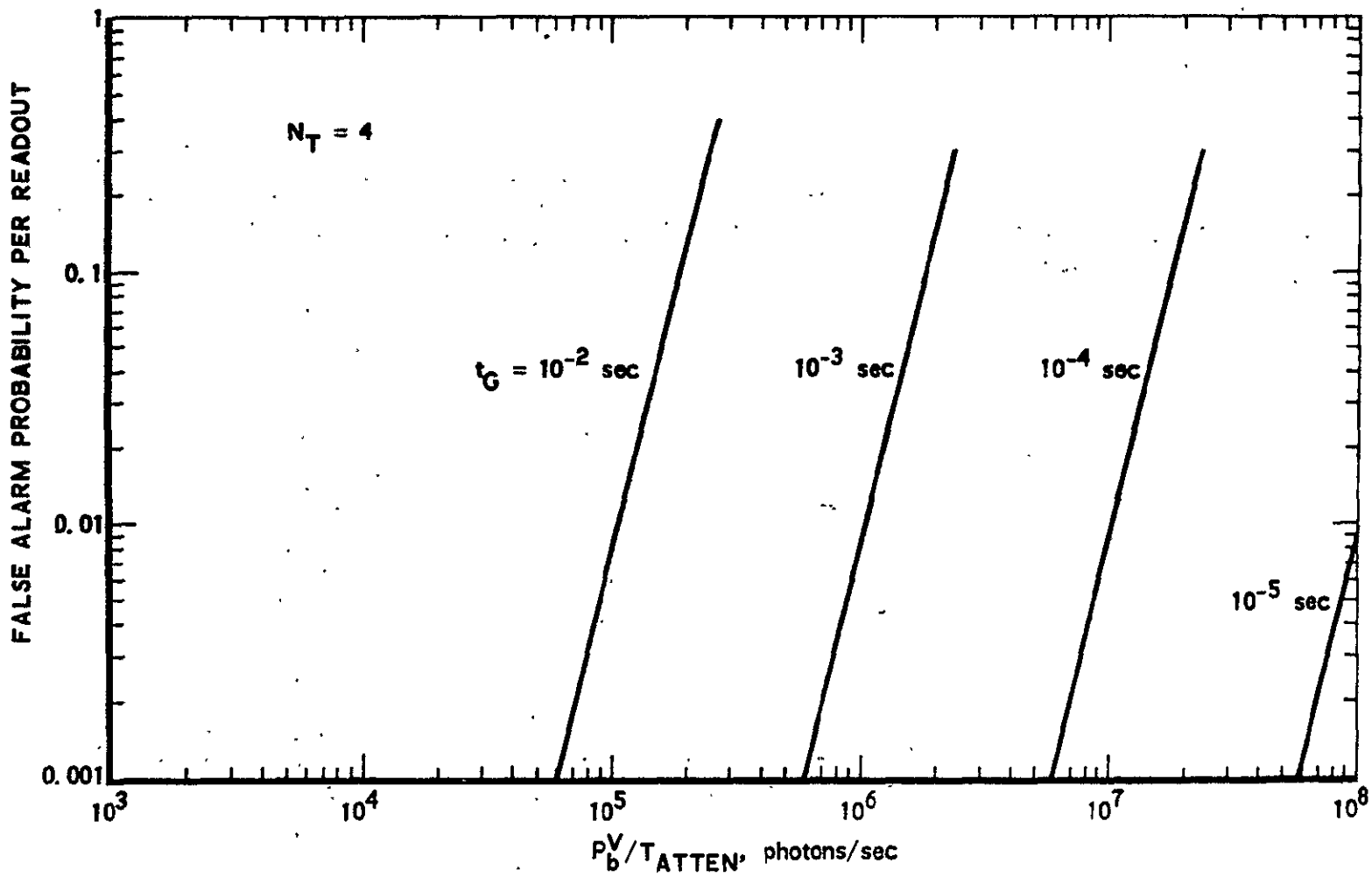

Fig. 15. False Alarm Probability per Readout for Vernier Detector, $N_T = 4$

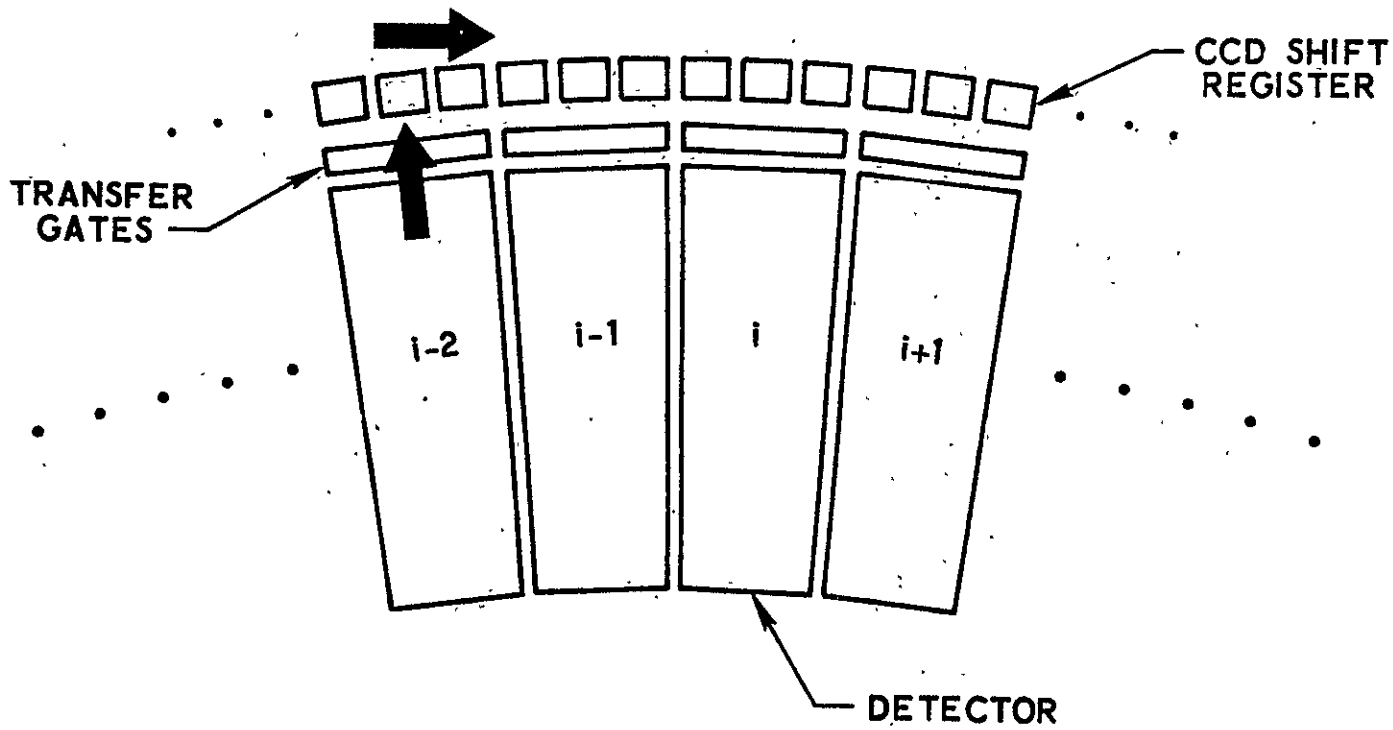

Fig. 16. Charge-Coupled-Device Vernier Target Layout

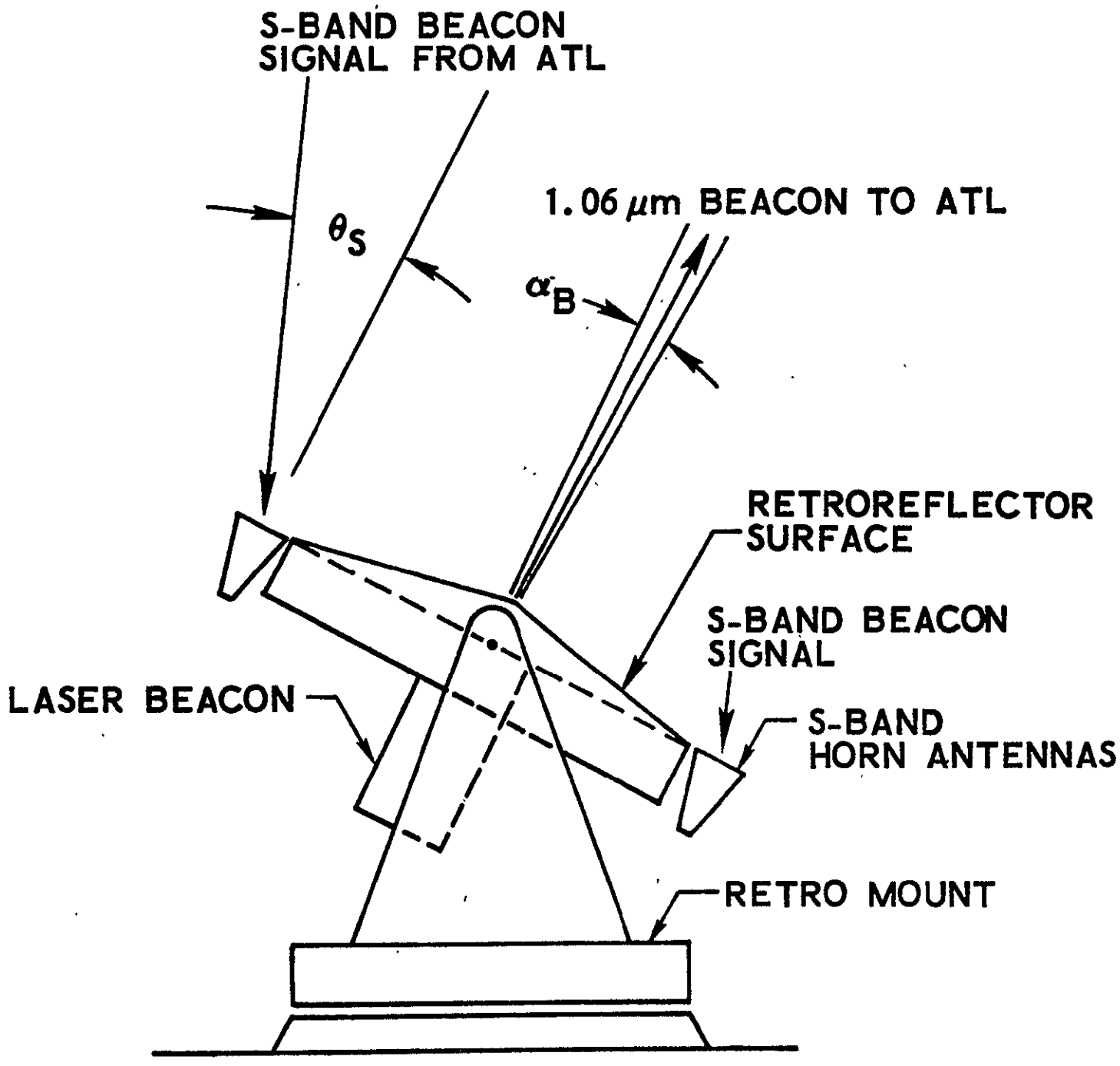

Fig. 17. Retroreflector, Laser Beacon, S-Band Tracking System Configuration

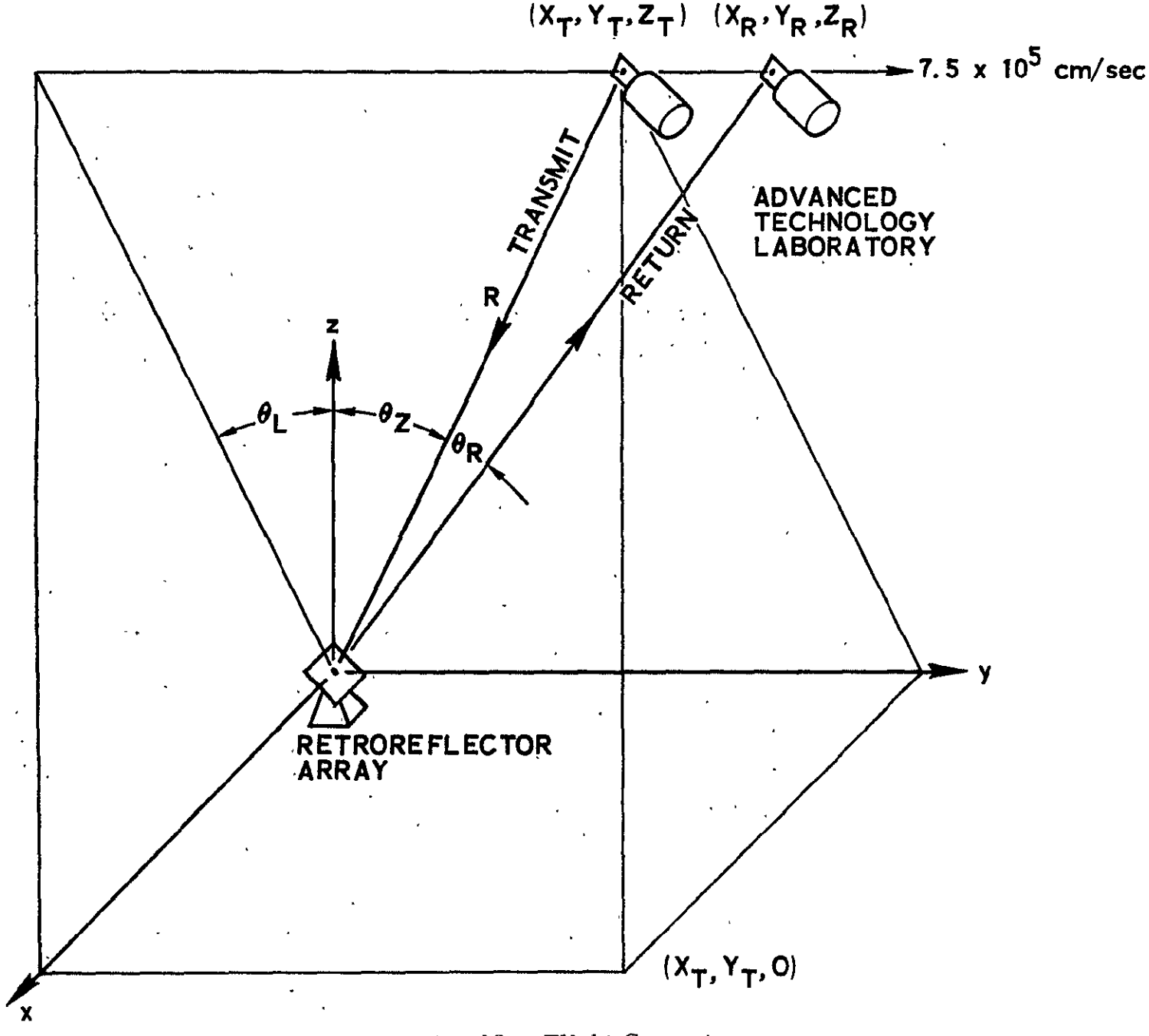

Fig. 18. Flight Geometry

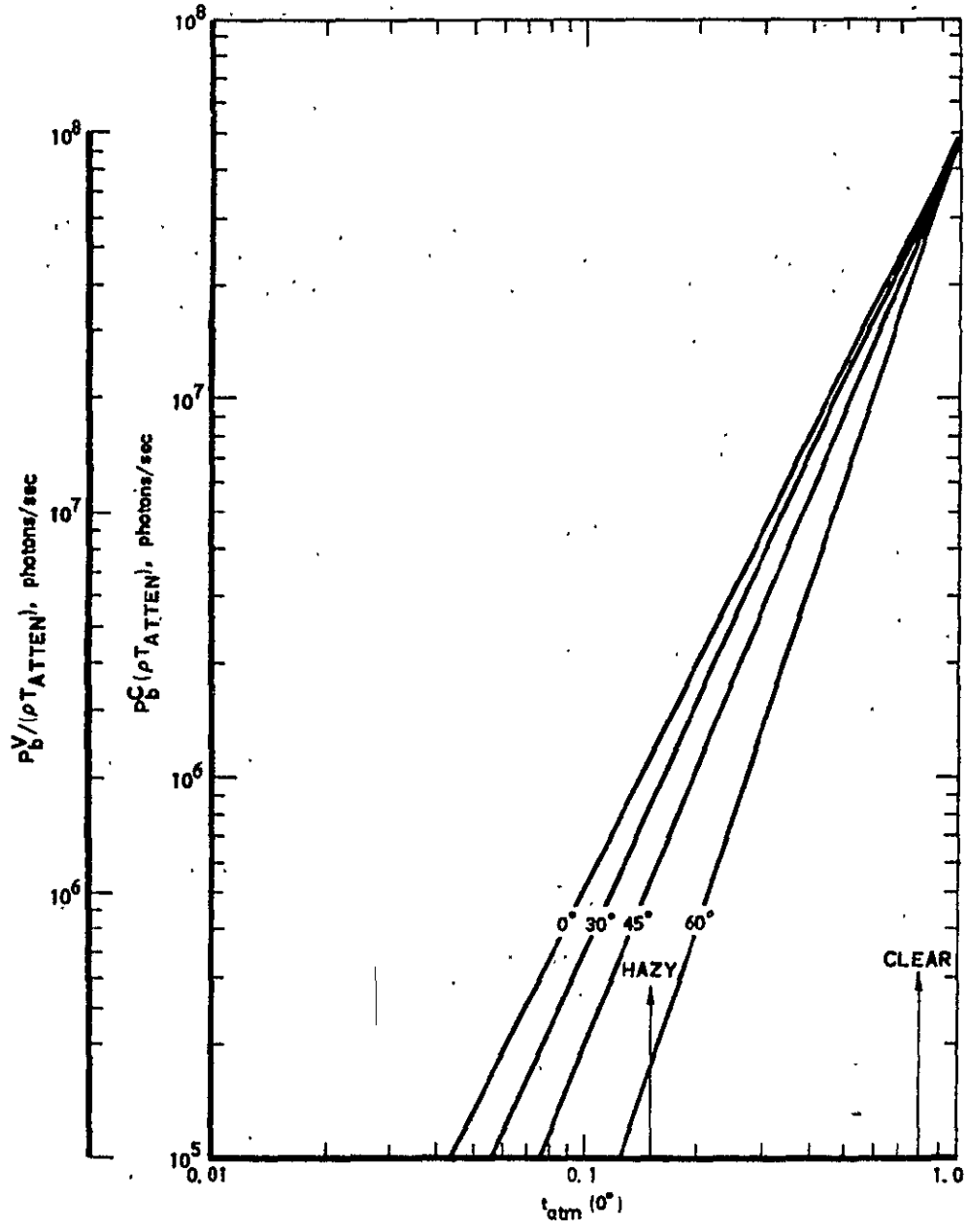

Fig. 19. Background Levels vs. Zenith Angle, Sun Overhead

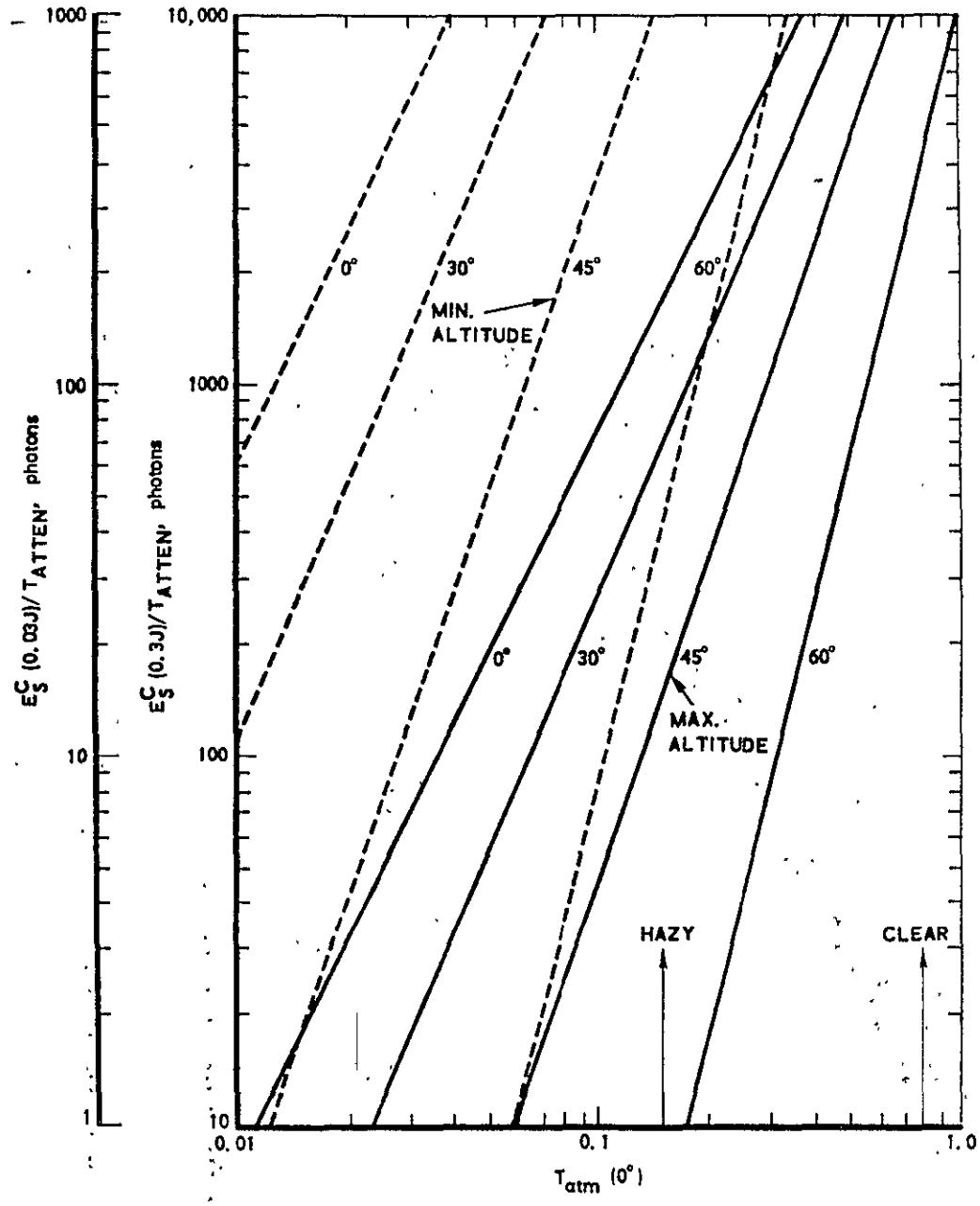

Fig. 20. Coarse Detector Signal Level vs. Zenith Angle, $Z_T(\min) = 1.85 \times 10^7$ cm, $Z_T(\max) = 5.56 \times 10^7$ cm, and $X_T = 0$

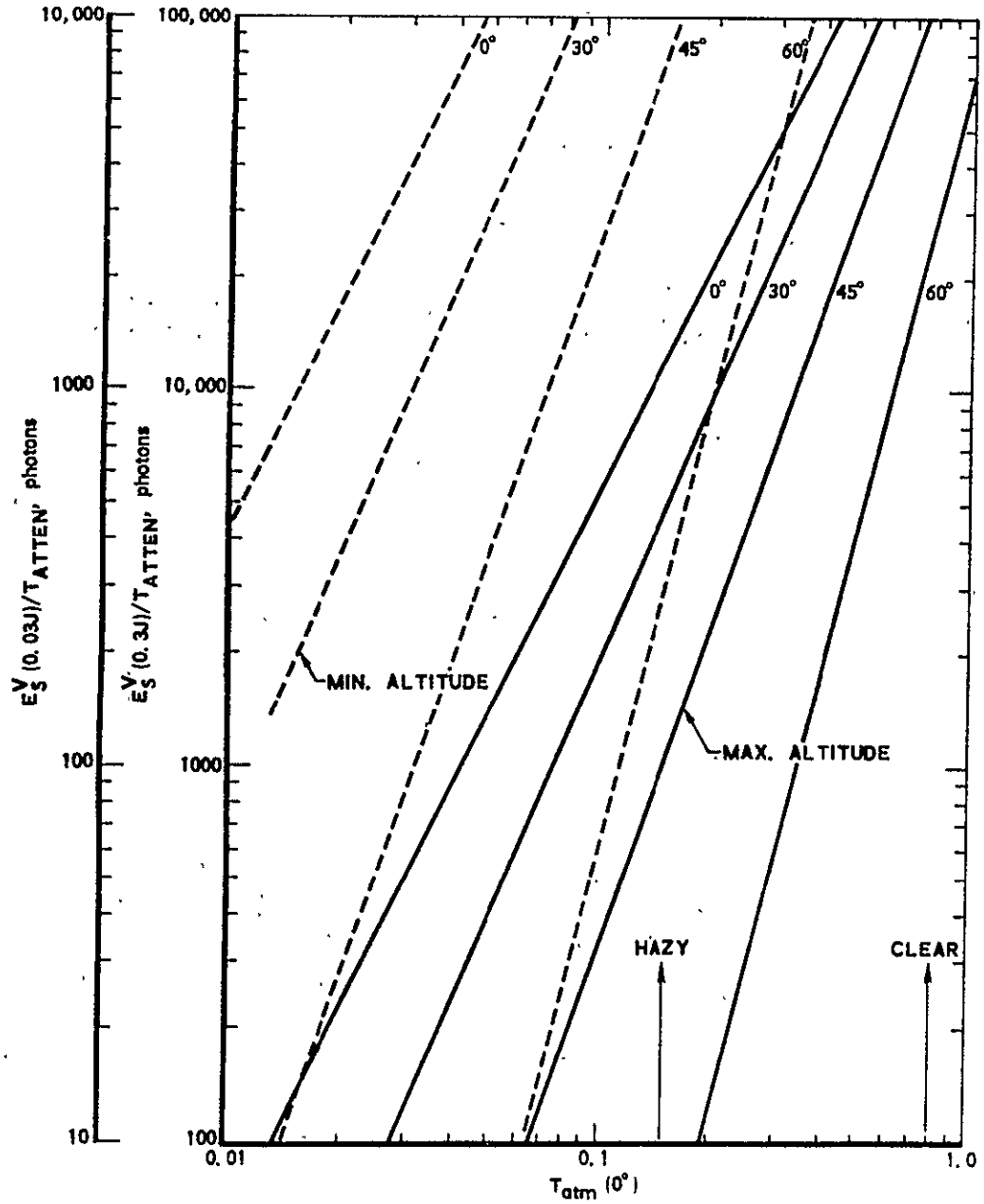

Fig. 21. Vernier Detector Signal Level vs. Zenith Angle, $Z_T(\min) = 1.85 \times 10^7$ cm, $Z_T(\max) = 5.56 \times 10^7$ cm, and $X_T = 0$

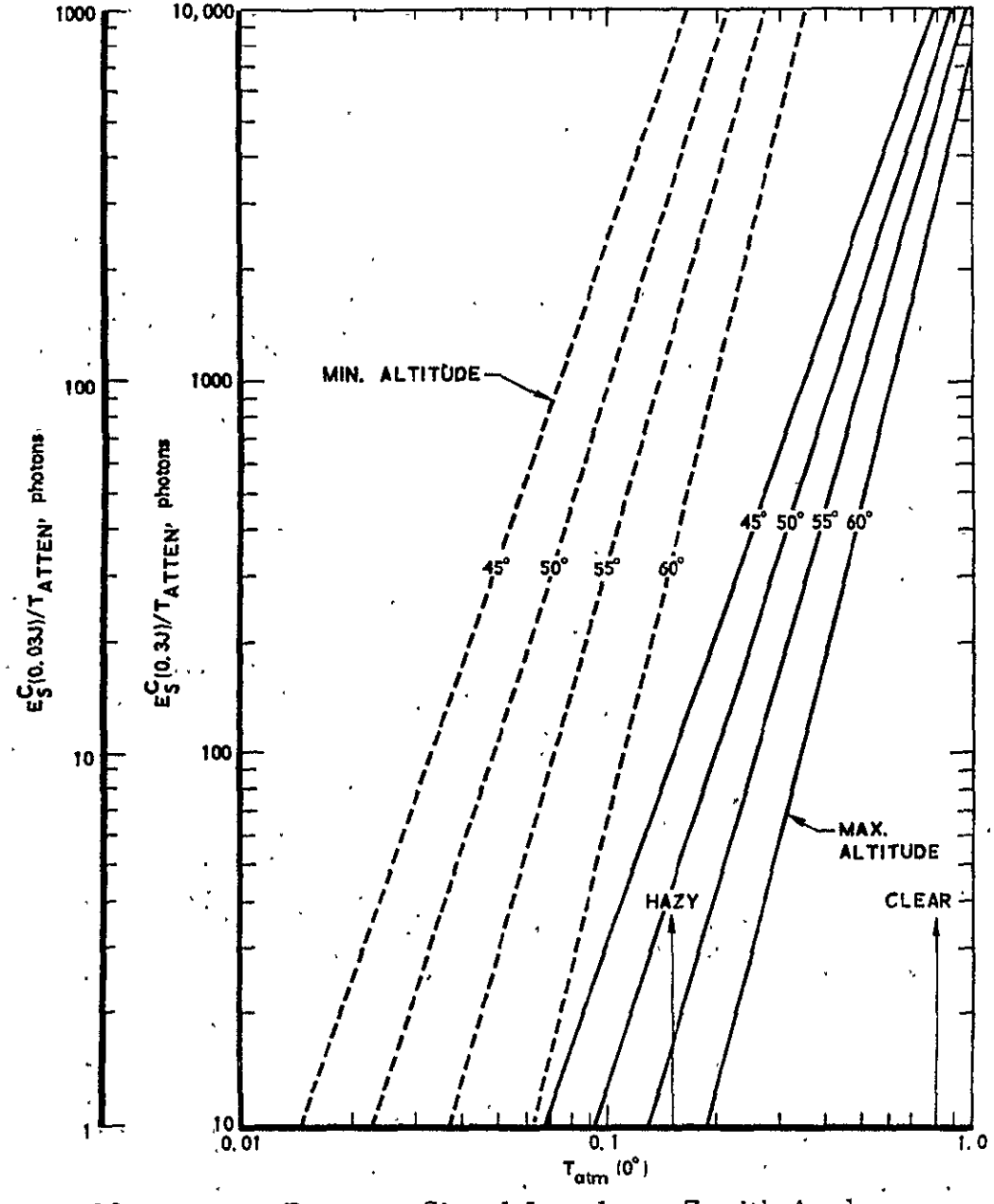

Fig. 22. Coarse Detector Signal Level vs. Zenith Angle, $Z_T(\min) = 1.85 \times 10^7$ cm, $Z_T(\max) = 5.56 \times 10^7$ cm, $X_T(\min) = 1.85 \times 10^7$ cm, and $X_T(\max) = 5.56 \times 10^7$ cm

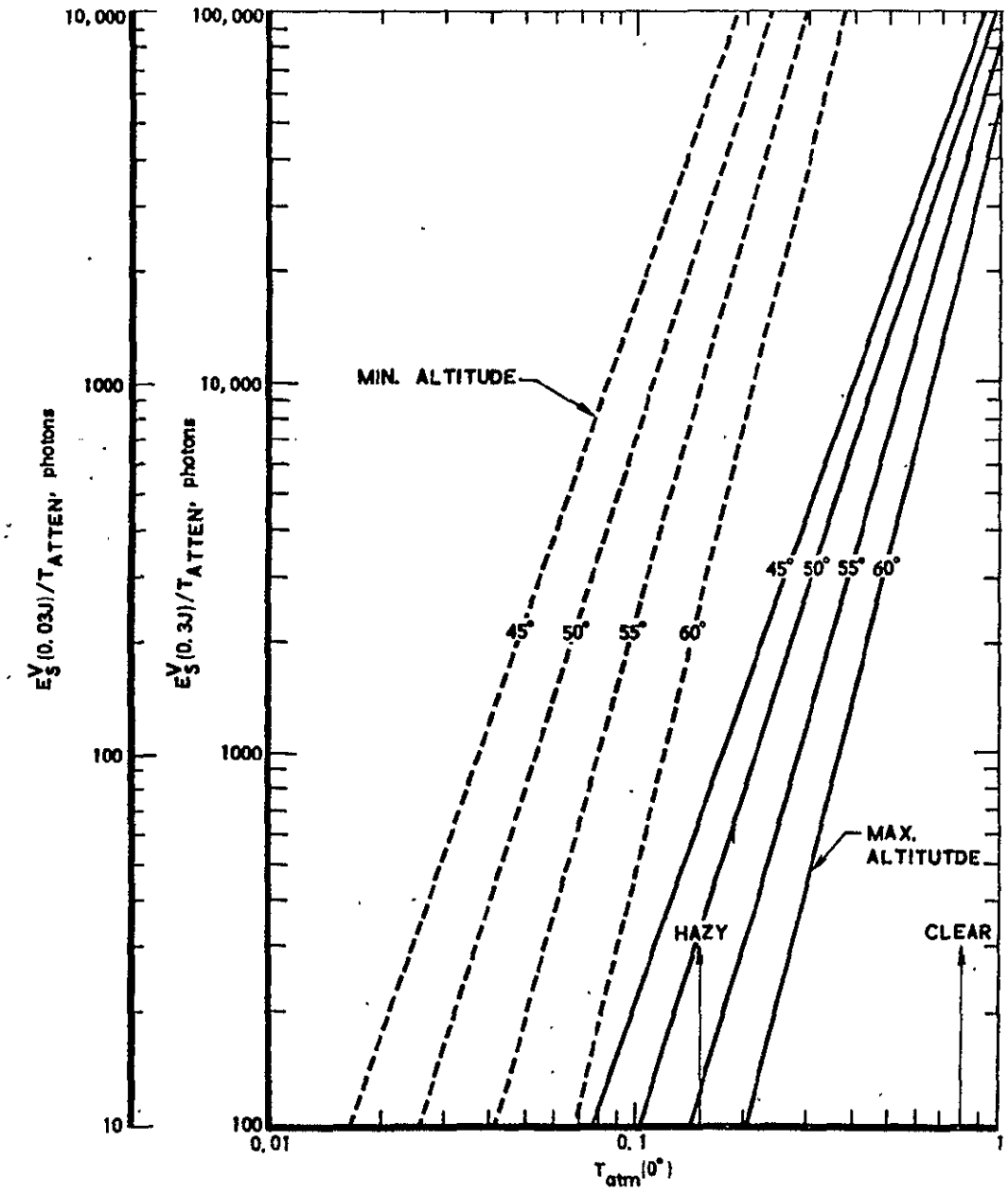

Fig. 23. Vernier Detector Signal Level vs. Zenith Angle, $Z_T(\min) = 1.85 \times 10^7$ cm, $Z_T(\max) = 5.56 \times 10^7$ cm, $X_T(\min) = 1.85 \times 10^7$ cm, and $X_T(\max) = 5.56 \times 10^7$ cm

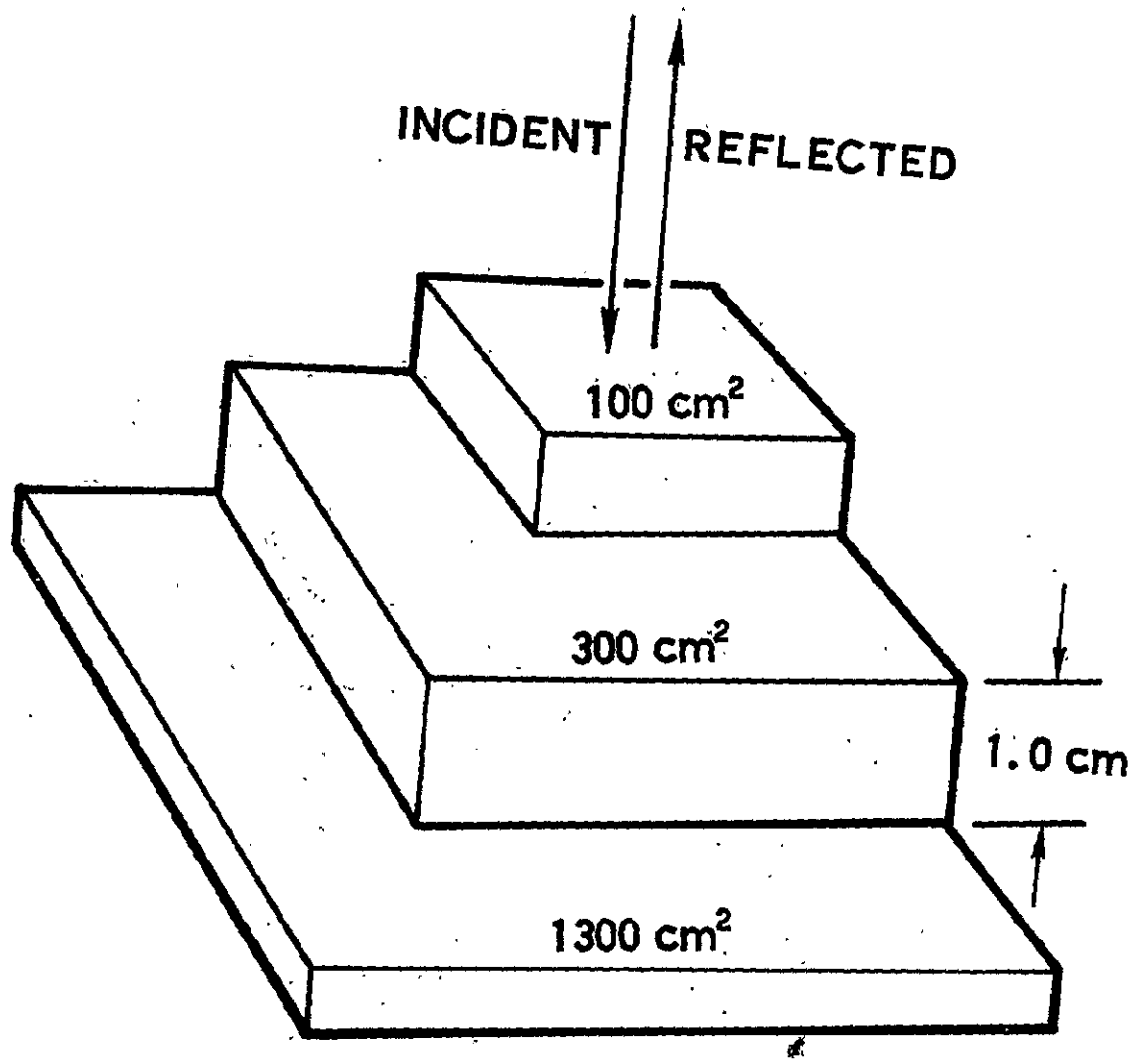

Fig. 24. Differential Range Retroreflector

REFERENCES

1. K. E. Golden, D. E. Kind, S. L. Leonard, and R. C. Ward, "Laser Ranging System with 1 cm Resolution," Applied Optics 12, p. 1447, July, 1973.

2. D. J. Bradley and Geoffrey H. C. New, "Ultrashort Pulse Measurements" Proc. IEEE 62, p. 313, March 1974.

3. G. D. Thayer, "Atmospheric Effects on Multiple-Frequency Range Measurements," ESSA Technical Report IER 56-ITSA 53, Oct. 1967.

4. K. E. Golden, E. E. Reber, and E. Ozaki, "Range Tests of a Mode-locked Laser Rangefinder System Having 1 cm Resolution, Aerospace Report, ATR 74(8161)-2, to be published.

5. S. L. Valley, Handbook of Geophysics, McGraw-Hill, New York, 1965.

6. A. T. Young, "Cosmic Ray Induced Dark Current in Photo Multipliers", Rev. Sci. Instr. 37, p. 1472, Nov. 1966.

7. W. B. Fowler, E. I. Reed, J. E. Blamont, "Effects of Energetic Particles on Photomultipliers in Earth Orbits up to 1500 Km," NASA Goddard Space Flight Center, Report No. Y-613-68-486, NASA TMX-6319, Dec. 1968.

8. R. L. Jerde, L. E. Peterson, and W. Stein, "Effects of High Energy Radiations on Noise Pulses from Photo multiplier Tubes" Rev. Sci. Instr. 38 p. 1387, Oct., 1967.

9. J. I. Vetti, "Models of the Trapped Radiation Environment, Vol. I, Inner Zone—Protons and Electrons", NASA SP-3024, 1966.

10. R. G. Stoudenheimer, "Ultra-High Speed Streak Photography Using Image Tubes" RCA Image Tube Application Note, AN-4789.

11. V. V. Korobkin, A. A. Maljotin, and M. Y. A. Schelev, "Time Resolution of an Image Converter Camera in Streak Operation", Journal of Photographic Science 17, p. 179, Oct., 1969.

12. W. W. Harman, Fundamentals of Electronic Motion, p. 144, McGraw-Hill, New York, 1953.

13. J. V. Uspensky, Introduction to Mathematical Probability, McGraw-Hill, New York, 1937, p. 22.

14. John F. McNall, "Photon Counting with a Self-Scanned Diode Array" in Astronomical Observations with Television-Type Sensors, Proceedings of a symposium held by Institute of Astronomy and Space Science, 15-17 May 1973, at University of British Columbia, Canada, J. W. Glospey and G. A. H. Walker, eds. pg. 111.

15. G. R. Riegler and K. A. More, "A High Resolution Position Sensitive Detector for Ultra violet and X-Ray Photons" IEEE Trans. Nucl. Sci. NS-20, 102 (1972).

16. D. McMullan, G. Wellgate, J. Ormerod, and J. Dickinson, "Serial Read-Out from Image Tubes Incoporating Silicon Diode Arrays", Advances in Electronics and Electron Physics, 33B, Academic Press, London, 1972, p. 873.

17. J. A. Westphal, "Application of the SIT Vidicon to Astronomical Measurements", in Astronomical Observations with Television-Type Sensors, Proceedings of Symposium held by Institute of Astronomy and Space Science, 15-17 May 1973, at University of British Columbia, Canada, J. W. Glaspey and G. A. H. Walker, eds., pg. 127.

18. See articles in Astronomical Observations with Television-Type Sensors, Ref. 16; also A. Boksenberg and D. E. Burgess, "An Image Photon Counting System for Optical Astronomy", Advances in Electronics and Electron Physics, 33B, Academic Press, London, 1972, p. 835.

19. M. Bass and H. H. Barrett, "Avalanche Breakdown and the Probabitistic Nature of Laser-Induced Damage," IEEE J. Quantum Electr. QE-8, 338 (March 1972).

20. A. J. Glass and A. H. Guenther, "Laser Induced Damage of Optical Elements — A Status Report," Appl. Opt. 12, 637 (April 1973).

21. A. J. Glass and A. H. Guenther, "Laser Induced Damage to Optical Materials, 1973: A Conference Report," Appl. Opt. 13, 74 (January 1974).

22. Laser-Fusion Program Semiannual Report — January - June 1972, Lawrence Livermore Laboratory, UCRL-50021-72-1: See pp. 6-28 and 71-73.

23. LLL Laser Projects Report No. 3, Lawrence Livermore Laboratory, TID-4500, UC-34 Physics, p. 7.

24. Korad, Division of Hadron, Inc., Santa Monica, Calif.: data on the "high-brightness laser systems," especially system K-1300. According to their spokesmen, and based on experience with the prototype-system laser, Korad specifications are quite conservative.

25. I. K. Krasynk, P. P. Pashkin, and A. M. Prokhorov, "Ring Ruby Laser for Ultrashort Pulses," JETP Letters 7, 89 (20 February 1968).

26. M. E. Mack, "Mode Locking the Ruby Laser," IEEE J. Quantum Electron. QE-4, 1015 (December 1968).

27. R. Cubeddu, R. Polloni, C. A. Sacchi, and O. Svelto, "Picosecond Pulses, TEM_{00} Mode, Mode-Locked Ruby Laser," IEEE J. Quantum Electron. QE-5, 470 (September 1969).

28. R. Polloni, "Single-Transverse-Mode-Locked Ruby Laser," IEEE J. Quantum Electron. QE-8, 428 (April 1972).

29. M. A. Duguay, J. W. Hansen, and S. L. Shapiro, "Study of the Nd: Glass Laser Radiation," IEEE J. Quantum Electron. QE-6, 725 (November 1970).

30. R. C. Edkardt, C. H. Lee, and J. N. Bradford, "Temporal and Spectral Development of Mode Locking in a Ring-Cavity Nd: Glass Laser," Appl. Phys. Letters 19, 420 (15 November 1971).

31. D. von der Linde, "Experimental Study of Simple Picosecond Light Pulses," IEEE J. Quantum Electron. QE-8, 328 (March 1972).

32. D. J. Bradley and W. Sibbett," Streak-Camera Studies of Picosecond Pulses from a Mode-Locked Nd: Glass Laser," Opt. Commun. 9, 17 (September 1973).

33. D. J. Bradley, G. H. C. New, and S. J. Caughey, "Subpicosecond Structure in Mode-Locked Nd: Glass Laser," Physics Lett. 30 A, 78 (22 September 1969).

34. E. B. Treacy, "Direct Demonstration of Picosecond-Pulse Frequency Sweep," Appl. Phys. Lett. 17, 14 (1 July 1970).

35. Korad data sheet on KM2 Frequency Multiplier, Hadron, Inc.

36. T. A. Rabson et al, "Efficient Second Harmonic Generation of Picosecond Laser Pulses," Appl. Phys. Letters 20, 282 (15 April 1972).

REFERENCES (Continued)

37. J. Comley and E. Garmire, "Second Harmonic Generation from Short Pulses," Appl. Phys. Lett. 12, 7 (1 January 1968).

38. Maxwell Laboratories, Inc., San Diego, Calif.: Bulletins 301R and 401R.

39. I. Kovalik and P. Hoffman, Maxwell Laboratories, Inc. Paul Hoffman suggests contacting W. Guman or D. Palumbo of Fairchild, Farmingdale, N. Y. for their experience with capacitors for satellite-type applications.

40. J. M. Ley, T. M. Christmar, C. G. Wildey, "Solid-State Subnanosecond Light Switch," Proc. IEE (London) 117, 1057 (June 1970).

41. C. Tsitsera, B. W. Driggs, and T. L. Kise, "Development of Microwave Interferometer Position Locator," IBM, NASA-Report, NASA CR-112188, Aug 1973.

42. C. McIntyre et al, "Laser Space Communication Systems," Proc. IEEE, 58, p. 1491, Oct. 1970.

43. N. S. Kopeika and J. Bordogna, "Background Noise in Optical Communication Systems," Proc. IEEE 59, p. 1571 Oct. 1970.

44. McClatchey et al, "Optical Properties of the Atmosphere, "AFCRL, Environmental Research Papers, No. 333, AFCRL-70-0S27, Sept. 1970

INTERNAL DISTRIBUTION LIST

M. Birnbaum

K. E. Golden (2)

T. S. Hartwick

G. W. King

R. L. Kohn

R. X. Meyer

G. A. Paulikas

D. A. Seib

A. H. Silver (12)

G. E. Stewart

R. E. Vassau

H. J. Wintroub

EXTERNAL DISTRIBUTION LIST

NASA Langley Research Center
Mail Stop 475
Hampton, Virginia 23365

Attn: J. H. Goad, Jr. (3)